SANTA CATARINA STATE UNIVERSITY – UDESC
JOINVILLE COLLEGE OF ENGENEERING – CCT
MECHANICAL ENGINEERING GRADUATE PROGRAM – PPGEM

FERNANDO VALENTINI

ROBUST TOPOLOGY OPTIMIZATION OF CONTINUUM STRUCTURES SUBJECTED TO UNCERTAINTIES IN THE EXCITATION FREQUENCY

JOINVILLE, SC
2021

FERNANDO VALENTINI

ROBUST TOPOLOGY OPTIMIZATION OF CONTINUUM STRUCTURES SUBJECTED TO UNCERTAINTIES IN THE EXCITATION FREQUENCY

Master's Thesis submitted to the Mechanical Engineering Graduate Program at the Joinville College of Engeneering of Santa Catarina State University in fulfilment of the partial requirement for the Master's degree in Mechanical Engineering, area: Numerical Modeling and Simulation.

Adviser: Prof. Dr. Eduardo Lenz Cardoso.

Co-Adviser: Dr. Olavo M. Silva.

JOINVILLE, SC
2021

Valentini, Fernando

V161r Robust Topology Optimization of Continuum Structures Subjected to Uncertainties in the Excitation Frequency / Fernando Valentini. – 2021.

91 p. : il. (algumas color.) ; 30 cm.

Orientador: Eduardo Lenz Cardoso

Coorientador: Olavo M. Silva

Dissertação (Mestrado) – Universidade do Estado de Santa Catarina, Centro de Ciências Tecnológicas, Programa de Pós-Graduação em Engenharia Mecânica, Joinville, 2021.

Inclui Bibliografia.

1. Robust design. 2. Topology optimization. 3. Harmonic Response. 4. Monte Carlo Simulation. 5. Density-weighted norm. I. Cardoso, Eduardo Lenz. II. Silva, Olavo M.. III. Universidade do Estado de Santa Catarina, Centro de Ciências Tecnológicas, Programa de Pós-Graduação em Engenharia Mecânica. IV. Título.

CDD: 620.1

FERNANDO VALENTINI

ROBUST TOPOLOGY OPTIMIZATION OF CONTINUUM STRUCTURES SUBJECTED TO UNCERTAINTIES IN THE EXCITATION FREQUENCY

Dissertação apresentada ao Programa de Pós-Graduação em Engenharia Mecânica do Centro de Ciências Tecnológicas da Universidade do Estado de Santa Catarina, como parte dos requisitos necessários para obtenção do título de Mestre em Engenharia Mecânica, área de concentração: Modelagem e Simulação Numérica.

BANCA EXAMINADORA

Orientador:

____
Prof. Dr. Eduardo Lenz Cardoso
Universidade do Estado de Santa Catarina
Departamento de Engenharia Mecânica

Membros:

____
Prof. Dr. André Teófilo Beck
Escola de Engenharia de São Carlos - Universidade de São Paulo
Departamento de Engenharia de Estruturas

____
Prof. Dr. Emilio Carlos Nelli Silva
Universidade de São Paulo
Escola Politécnica da Universidade de São Paulo

Joinville, 24 de fevereiro de 2021.

ACKNOWLEDGMENTS

The author would like to express the following acknowledgments:

To my beloved family, Eduardo Valentini, Salvelina M. B. Valentini and Marina Valentini, for being nothing less than my safe haven, my example of life and dignity. Thanks for the unconditional patience, care and support during all my life.

To my lovely Jéssica M. S. de Souza, for all the love and all the support throughout this journey, without which I most certainly would not have been able to succeed.

To Prof. Dr. Eduardo Lenz Cardoso, for sharing with me so much of his brilliant knowledge and so much of his time, and for all the support and guidance during the development of this research. My sincere gratitude for being the best adviser I could have ever asked for.

To Dr. Olavo M. Silva, co-adviser, for accepting this challenge together with us, enriching the discussions and analyses herein provided with great knowledge and expertise.

To my dear friend MSc. Diego S. Montero, first, for opening the front doors of this University to me; second, for his outstanding Master's thesis that inspired this work; and third, for being an example in personal and professional life.

To the Professors and professionals of the Mechanical Engineering Graduate Program for the contribution to my education and intellectual development.

This study was financed in part by the Coordenação de Aperfeiçoamento de Pessoal de Nível Superior - Brasil (CAPES) – Finance Code 001. The author would also like to acknowledge the financial support from FAPESC (Fundação de Amparo à Pesquisa e Inovação do Estado de Santa Catarina), through grant n. 2019TR000779 and *Universidade do Estado de Santa Catarina* for providing the computational resources.

ABSTRACT

This work studies the robust design of structures with minimum dynamic response (non-resonant structures) and maximum dynamic response (resonant structures) considering uncertainty in the excitation frequency, using topology optimization. The Monte Carlo Simulation method with stratified sampling is used to model both the expected value and standard deviation of the structural dynamic response, described by a density-weighted norm. Results show that the proposed formulation leads to the design of structures with optimized dynamic response and improved robustness, which is attested by comparison with the deterministic approach.

Results also show that the mechanisms used to increase the robustness depend on the target frequency. For minimization cases, at low frequencies, a mode separation mechanism is preferred, while for higher frequencies, low energy resonant modes are used. For maximization cases, there is also dependency on the excitation frequency, however, in a lower scale. In general, subsequent high-energy resonances located before and after the target excitation frequency improve response robustness while ensuring a resonating behavior within the interval bounded by the mentioned subsequent resonant modes.

Key-words: Robust design. Topology optimization. Harmonic Response. Monte Carlo Simulation. Density-weighted norm.

RESUMO

Este trabalho estuda o projeto robusto de estruturas com resposta dinâmica mínima (estruturas não ressonantes) e resposta dinâmica máxima (estruturas ressonantes) considerando a incerteza na frequência de excitação, utilizando otimização topológica. O método de simulação de Monte Carlo com amostragem estratificada é usado para modelar tanto o valor esperado quanto o desvio padrão da resposta dinâmica estrutural, descrita por uma norma de densidade ponderada. Os resultados mostram que a formulação proposta leva ao projeto de estruturas com resposta dinâmica otimizada e maior robustez, o que é atestado por comparação com a abordagem determinística.
Os resultados também mostram que os mecanismos utilizados para aumentar a robustez dependem da frequência alvo. Para casos de minimização, em baixas frequências, um mecanismo de separação de modo é preferido, enquanto para frequências mais altas, modos ressonantes de baixa energia são usados. Para os casos de maximização, também há dependência da frequência de excitação, porém em escala inferior. Em geral, ressonâncias de alta energia subsequentes que são localizadas antes e depois da frequência de excitação alvo melhoram a robustez da resposta, garantindo um comportamento ressonante dentro do intervalo limitado pelos modos ressonantes subsequentes mencionados.

Palavras-chave: Projeto Robusto. Otimização topológica. Resposta harmônica. Simulação de Monte Carlo. Norma de densidade ponderada.

LIST OF FIGURES

Figure 1 – Finite Element 22
Figure 2 – Normal distribution 38
Figure 3 – Stratified sampling. 42
Figure 4 – Optimization algorithm flowchart. 46
Figure 5 – Definition of Problem 1. 48
Figure 6 – Definition of Problem 2 49
Figure 7 – Frequency response of the Problem 2. 50
Figure 8 – Topologies obtained with the deterministic approach, Eq. (85), for the test case depicted in Fig. 5. 51
Figure 9 – Topologies obtained at 365 Hz, for different values of η and φ. 52
Figure 10 – Histograms of $N_{m\omega dB}$ comparing the robust and deterministic designs at 365 Hz, for different values of η and φ. Histograms in green are relative to deterministic designs and the histograms in grey are relative to robust designs. 54
Figure 11 – Frequency response for the robust design ($\eta = 10$ Hz and $\varphi = 15.0$) and for the deterministic design (left) and topology with dynamic displacement fields (absolute values) at three different frequencies for the same robust design (right), obtained at 365 Hz. 55
Figure 12 – Topologies obtained at 700 Hz, for different values of η and φ. 56
Figure 13 – Histograms of $N_{m\omega dB}$ comparing the robust and deterministic designs at 700 Hz, for different values of η and φ. Histograms in green are relative to deterministic designs and the histograms in grey are relative to robust designs. 57
Figure 14 – Frequency response for the robust design ($\eta = 10$ Hz and $\varphi = 15.0$) and for the deterministic design (left) and topology with dynamic displacement fields (absolute values) at three different frequencies for the same robust design (right), obtained at 700 Hz. 58
Figure 15 – Topologies obtained at 1135 Hz, for different values of η and φ. 59
Figure 16 – Histograms of $N_{m\omega dB}$ comparing the robust and deterministic designs at 1135 Hz, for different values of φ and η. Histograms in green are relative to deterministic designs and the histograms in grey are relative to robust designs. 61
Figure 17 – Frequency response for the robust design ($\eta = 10$ Hz and $\varphi = 15.0$) and for the deterministic design (left) and topology with dynamic displacement fields (absolute values) at three different frequencies for the same robust design (right), obtained at 1135 Hz. 62
Figure 18 – Topologies obtained at 1440 Hz, for different values of φ and η. 62
Figure 19 – Histograms of $N_{m\omega dB}$, comparing the robust and deterministic designs at 1440 Hz, for different values of φ and η. Histograms in green are relative to deterministic designs and the histograms in grey are relative to robust designs. 63
Figure 20 – Frequency response for the robust design ($\eta = 10$ Hz and $\varphi = 15.0$) and for the deterministic design (left) and topology with dynamic displacement fields (absolute values) at three different frequencies for the same robust design (right), obtained at 1440 Hz. 64

Figure 21 – Convergence for the Lagrangian Function (solid line), volume constraint (dotted line) and intermediate topologies and frequency responses at some external iterations. Tuples over each topology indicate the pair (ζ, β_H). . . 65
Figure 22 – Topologies obtained for the asymmetric loading test case, for different target frequencies and for $\varphi = 15.0$ and $\eta = 10.0$ Hz. 66
Figure 23 – Frequency response for the robust design ($\eta = 10$ Hz and $\varphi = 15.0$) and for the deterministic design (left) and displacement fields (absolute values) at three different frequencies for the same robust design (right), obtained at 420 Hz. 67
Figure 24 – Frequency response for the robust design ($\eta = 10$ Hz and $\varphi = 15.0$) and for the deterministic design (left) and displacement fields (absolute values) at three different frequencies for the same robust design (right), obtained at 700 Hz. 68
Figure 25 – Frequency response for the robust design ($\eta = 10$ Hz and $\varphi = 15.0$) and for the deterministic design (left) and displacement fields (absolute values) at three different frequencies for the same robust design (right), obtained at 930 Hz. 68
Figure 26 – Frequency response for the robust design ($\eta = 10$ Hz and $\varphi = 15.0$) and for the deterministic design (left) and displacement fields at three different frequencies for the same robust design (right), obtained at 1425 Hz. 69
Figure 27 – Histograms of $N_{m\omega dB}$ for different frequencies and for $\varphi = 15.0$ and $\eta = 10.0$ Hz. Histograms in green are relative to deterministic designs and histograms in grey are relative to robust designs. 69
Figure 28 – Topologies obtained with the deterministic approach, Eq. (85), and standard parametrization for the test case depicted in Fig. 5. 71
Figure 29 – Topologies obtained with the deterministic approach, Eq. (85), and modified parametrization for the test case depicted in Fig. 5. 71
Figure 30 – Topologies obtained for maximization at 365 Hz, for different values of φ and $\eta = 20$ Hz. 72
Figure 31 – Frequency response of the deterministic design ($N_{AL} = 15$) and robust design cases at 365 Hz, where Robust Design 1, 2 and 3 correspond to $\varphi = 10.0$, 20.0 and 50.0, respectively. 72
Figure 32 – Histograms of $N_{m\omega dB}$, comparing the robust and deterministic designs for maximization at 365 Hz, for different values of φ and $\eta = 20$ Hz. Histograms in green are relative to deterministic designs and the histograms in grey are relative to robust designs. 73
Figure 33 – Frequency response for the robust design ($\eta = 20$ Hz and $\varphi = 50.0$) and for the deterministic design obtained with $N_{AL} = 25$ (left) and topology with dynamic displacement fields (real values) at three different frequencies for the same robust design (right), obtained for maximization at 365 Hz. 74
Figure 34 – Topologies obtained for maximization at 700 Hz, for different values of φ and $\eta = 20$ Hz. 75
Figure 35 – Frequency response of the deterministic design (mesh 100×50 and $N_{AL} = 15$) and robust design cases at 700 Hz, where Robust Design 1, 2 and 3 correspond to $\varphi = 10.0$, 20.0 and 50.0, respectively. 75

Figure 36 – Histograms of $N_{m\omega dB}$, comparing the robust and deterministic designs for maximization at 700 Hz, for different values of φ and $\eta = 20$ Hz. Histograms in green are relative to deterministic designs and the histograms in grey are relative to robust designs. 76
Figure 37 – Frequency response for the robust design ($\eta = 20$ Hz and $\varphi = 50.0$) and for the deterministic design obtained with 140×70 elements (left) and topology with dynamic displacement fields (absolute values) at three different frequencies for the same robust design (right), obtained for maximization at 700 Hz. 77
Figure 38 – Topologies obtained for maximization at 1135 Hz, for different values of φ and $\eta = 20$ Hz. 78
Figure 39 – Frequency response of the deterministic design (mesh 100×50 and $N_{AL} = 15$) and robust design cases at 1135 Hz, where Robust Design 1, 2 and 3 correspond to $\varphi = 10.0$, 20.0 and 50.0, respectively. 78
Figure 40 – Histograms of $N_{m\omega dB}$, comparing the robust and deterministic designs for maximization at 1135 Hz, for different values of φ and $\eta = 20$ Hz. Histograms in green are relative to deterministic designs and the histograms in grey are relative to robust designs. 79
Figure 41 – Frequency response for the robust design ($\eta = 20$ Hz and $\varphi = 50.0$) and for the deterministic design (left) and topology with dynamic displacement fields (absolute values) at three different frequencies for the same robust design (right), obtained for maximization at 1135 Hz. 79
Figure 42 – Topologies obtained for maximization at 1440 Hz, for different values of φ and $\eta = 20$ Hz. 80
Figure 43 – Frequency response of the deterministic design (mesh 100×50 and $N_{AL} = 15$) and robust design cases at 1440 Hz, where Robust Design 1, 2 and 3 correspond to $\varphi = 10.0$, 20.0 and 50.0, respectively. 81
Figure 44 – Histograms of $N_{m\omega dB}$, comparing the robust and deterministic designs for maximization at 1440 Hz, for different values of φ and $\eta = 20$ Hz. Histograms in green are relative to deterministic designs and the histograms in grey are relative to robust designs. 82
Figure 45 – Frequency response for the robust design ($\eta = 20$ Hz and $\varphi = 20.0$) and for the deterministic design (left) and topology with dynamic displacement fields (absolute values) at three different frequencies for the same robust design (right), obtained for maximization at 1440 Hz. 82

LIST OF TABLES

Table 1 – Relative differences for expected value, standard deviation and Inf norm of sensitivities with respect to the reference MCS with 1×10^6 realizations. 48
Table 2 – Problem data - Test case 1. 49
Table 3 – Problem data - Test case 2. 49
Table 4 – Expected values $E[N_{m\omega dB}]$ at 365 Hz, for different values of η and φ. . . . 53
Table 5 – Standard deviations $Std[N_{m\omega dB}]$ at 365 Hz, for different values of η and φ. 53
Table 6 – Expected values $E[N_{m\omega dB}]$ at 700 Hz, for different values of φ and η. . . . 55
Table 7 – Standard deviations $Std[N_{m\omega dB}]$ at 700 Hz, for different values of φ and η. 56
Table 8 – Expected values $E[N_{m\omega dB}]$ at 1135 Hz for different values of η and φ. . . 60
Table 9 – Standard deviations $Std[N_{m\omega dB}]$ at 1135 Hz for different values of η and φ. 60
Table 10 – Expected values $E[N_{m\omega dB}]$ at 1440 Hz, for different values of φ and η. . . 61
Table 11 – Standard deviations $Std[N_{m\omega dB}]$ at 1440 Hz, for different values of φ and η. 63
Table 12 – Expected values $E[N_{m\omega dB}]$ and standard deviations $Std[N_{m\omega dB}]$ at 365 Hz of the deterministic design ($\varphi = 0.0$) and the robust designs, for different values of φ and $\eta = 20.0$ Hz. 73
Table 13 – Expected values $E[N_{m\omega dB}]$ and standard deviations $Std[N_{m\omega dB}]$ at 700 Hz of the deterministic design ($\varphi = 0.0$) and the robust designs, for different values of φ and $\eta = 20.0$ Hz. 76
Table 14 – Expected values $E[N_{m\omega dB}]$ and standard deviations $Std[N_{m\omega dB}]$ at 1135 Hz of the deterministic design ($\varphi = 0.0$) and the robust designs, for different values of φ and $\eta = 20.0$ Hz. 79
Table 15 – Expected values $E[N_{m\omega dB}]$ and standard deviations $Std[N_{m\omega dB}]$ at 1440 Hz of the deterministic design ($\varphi = 0.0$) and the robust designs, for different values of φ and $\eta = 20.0$ Hz. 81

CONTENTS

1 INTRODUCTION . . . 13
1.1 STATE OF THE ART . . . 13
1.2 CONTRIBUTIONS . . . 16
1.3 THESIS OUTLINE . . . 16

2 DYNAMIC EQUILIBRIUM PROBLEM . . . 18
2.1 ELASTODYNAMICS . . . 18
2.2 FINITE ELEMENT DOMAIN DISCRETIZATION . . . 19
2.2.1 Finite Element Definition . . . 21
2.3 HARMONIC PROBLEM DEFINITION . . . 23

3 GENERAL OPTIMIZATION . . . 24
3.1 OPTIMIZATION PROBLEM DEFINITION AND OPTIMALITY CRITERIA 24
3.2 SOLUTION STRATEGY . . . 25
3.3 AUGMENTED LAGRANGIAN METHOD . . . 26

4 TOPOLOGY OPTIMIZATION FOR HARMONIC PROBLEMS 28
4.1 MATERIAL PARAMETRIZATION . . . 28
4.2 FILTERING AND PROJECTION . . . 29
4.3 DAMPING MODELING . . . 29
4.4 SENSITIVITY ANALYSIS OF HARMONIC PROBLEMS . . . 30
4.5 DETERMINISTIC APPROACH FOR DYNAMIC DISPLACEMENTS OPTIMIZATION . . . 31
4.5.1 Sensitivity Analysis of the Density-Weighted Norm . . . 32

5 UNCERTAINTY . . . 35
5.1 RANDOM VARIABLE . . . 36
5.2 NORMAL PROBABILITY DENSITY FUNCTIONS . . . 38

6 PROBABILISTIC ROBUST OPTIMIZATION . . . 40
6.1 SENSITIVITY ANALYSIS OF A PROBABILISTIC ROBUST PROBLEM 42

7 PROPOSED FORMULATION . . . 44

8 RESULTS . . . 47
8.1 DESIGN MODELS . . . 47
8.1.1 Cantilever beam with central loading . . . 48
8.1.2 Cantilever beam with bottom loading . . . 48
8.2 DYNAMIC RESPONSE MINIMIZATION . . . 50
8.2.1 Cantilever beam with central loading . . . 51
8.2.1.1 Results at 365 Hz . . . 51
8.2.1.2 Results at 700 Hz . . . 55
8.2.1.3 Results at 1135 Hz . . . 58
8.2.1.4 Results at 1440 Hz . . . 60
8.2.2 Convergence analysis . . . 64
8.2.3 Cantilever beam with bottom loading . . . 65
8.3 DYNAMIC RESPONSE MAXIMIZATION . . . 67
8.3.1 Results at 365 Hz . . . 71

8.3.2 Results at 700 Hz . . . 74
8.3.3 Results at 1135 Hz . . . 77
8.3.4 Results at 1440 Hz . . . 80

9 CONCLUSIONS . . . **84**
9.1 FUTURE WORK . . . 84

REFERENCES . . . **86**

1 INTRODUCTION

This work proposes a formulation for the robust design of structures with either minimum or maximum dynamic response considering uncertainties in the excitation frequency. The objective is to optimize the dynamic response while minimizing its variance with respect to a given target frequency. Low response variance configures the meaning of the term robust for the objectives of this work.

Due to the non-linear nature of dynamic problems, small perturbations on the excitation frequency might cause a large impact on the structural dynamic response. Such dependency increases even more, specially close or at a resonance, due to the shifting of energy expenditure inside the structure (potential and kinetic). This main characteristic composes the challenge that motivated the development of this work.

Topology optimization (TO) is used in this work to determine the optimal material distribution within a fixed domain to achieve the desired dynamic behavior. When the objective is a non-resonant structure, the resultant design will have high-energy resonance frequencies as far as possible of the excitation frequency. The opposite occurs when maximization of dynamic displacements is targeted, such that the resultant structure will resonate exactly at the excitation frequency.

Structures with a robust dynamic behavior offer the assurance that undesired responses will not take place around a target excitation frequency. In the case of non-resonant structures, the aimed dynamic response would demonstrate low and consistent displacements. When it comes to resonant structures, a smoother response behavior around resonance is desired, which is particularly useful for applications like energy harvesting such that power generation improvements could happen in scenarios where the excitation frequency is not precisely synchronized to the structure's natural frequency.

Among many practical applications for non-resonant structures, one can devise the design of a rotatory system (electric motor) with minimum vibration and less sensitive to variations in the excitation frequency (for example, due to variations in the grid frequency) or the design of a support structure to a measuring device, with minimum vibration transfer for a given range of base excitation frequency. Thinking about resonant designs, an eventual application is structures for energy harvesting purposes, where the generated power is proportional to the displacements magnitude. In this context, the robust resonant design should have high displacements at a frequency range, and not only at a specific target frequency.

Such improved dynamic behavior can be achieved by the use of the robust approach herein proposed for the design of structures less sensitive to changes in operation parameters, as the excitation frequency, with lowest possible penalty in the dynamic response at a given target excitation frequency.

1.1 STATE OF THE ART

There are different approaches used to optimize the structural dynamic behavior, and the most common approaches found in the literature are based on modal analysis, transient or harmonic dynamic response.

Reviewing the works based on modal analysis, efforts regarding dynamic response minimization started with the work of Fox and Kapoor (1970), where truss structures subjected to a given base motion were designed for minimum mass and controlled stress. Also, Bendsøe and Olhoff (1985) addressed the maximization of the gap between two subsequent resonant vibration modes with respect to a given frequency of interest for the optimal design of vibrating beams or shafts. However, parametric optimization is used in these works instead of topology optimization. Works of Díaz and Kikuchi (1992), Krog and Olhoff (1999), and Pedersen (2000) also discuss the maximization of the first resonance frequency using topology optimization.

The work of Du and Olhoff (2007) investigated optimization problems involving simple and multiple eigenfrequencies in order to maximize specific natural frequencies or even create a gap between two resonances. Subsequently, Niels Olhoff and Jianbin Du (2008) evaluated several different methods for reaching minimum dynamic response. The ones related to the modal approach are the maximization of a higher order eigenvalue and gap maximization between two resonances. Additionally, the minimization of sound power radiation to an acoustic medium is evaluated.

Regarding the works based on harmonic dynamic displacements calculation, there are several different approaches that were investigated. As a starting point, minimization of dynamic compliance for harmonic topology optimization was studied by Ma, Kikuchi, and Hagiwara (1993), targeting non-resonant structures. The caveats of using the dynamic compliance are that it is not a positive-definite measure (NIU et al., 2018), which leads to convergence problems, and also the necessity of considering static compliance to circumvent disconnection of the structure from the supports. Also using the dynamic compliance approach, Min et al. (1999) worked on its minimization using explicit direct integration for different frequencies to design structures subjected to harmonic loads.

A different approach is proposed by the work of Jog (2002), in which the dynamic compliance is redefined as a positive-definite measure in the presence of vibration and zero when the structure is static, meaning that the minimization of the dynamic compliance would drive the structure to a static state. Also, the work suggests a local approach for vibration minimization, allowing the user to choose a certain area of the structure to be non-resonant, without any concern to other areas. In addition, dynamic compliance minimization is briefly discussed in the work of Niels Olhoff and Jianbin Du (2008).

Efforts on the maximization of harmonic response happened in parallel with the ones made on the harmonic response minimization. First work on this area is signed by Tcherniak (1999) in which the problem of structure disconnection from the boundary conditions is reported. Static compliance has been added as a constraint to solve the issue. Also, Dmitri Tcherniak (2002) denotes problems regarding modes existent in void regions and proposes an external damper to ensure connection to the boundary conditions.

On the area of energy harvesting, Deng et al. (2015) built an objective function with two parts. The first one ensures maximization of output displacement and the second one ensures minimization of perpendicular stiffness so that the device would not touch the surroundings. This second part of the objective function ends up increasing the static stiffness and ensures a well connected structure.

Either input power and dynamic stiffness have been evaluated in the work of Silva (2017) for the design of resonant structures, Again, static compliance has been added to aid in structure connection to the supports.

The work of Silva, Neves, and Lenzi (2019) provides a critical evaluation of several different ways of using the dynamic compliance in harmonic response minimization problems. Furthermore, it shows that minimization of dynamic compliance leads to convergence issues caused by antiresonances for designs that target frequencies above the first resonance, since it may be difficult to move out from this point. In Silva, Neves, and Lenzi (2020), the same authors suggest the use of the input power concept in this type of problem, resulting in well-defined designs at any frequency range, however, still using static compliance in the objective function. Additionally, in Silva and Neves (2020), the use of complex input power is proven to be a good alternative to overcome convergence issues in the design of resonant structures, again considering static compliance in the formulation.

More recently, Montero, Silva, and Cardoso (2020) proposed a new measure, the density-weighted norm, that has the capacity to precisely identify resonances and also eliminates the presence of non-physical modes in regions where voids are located. These two main characteristics are of great interest to the goals herein discussed. Therefore, the formulation proposed by Montero, Silva, and Cardoso (2020) is the base for this work. This measure, however, does not solve the known structural disconnection problem and also requires the use of static compliance in the objective function.

Regarding the robust design methodology, Stockl (2001) developed a method for the design of truss structures considering stochastic uncertainties on any characteristic of the problem, such as material properties or loading. It is observed that robust designs have additional bars when compared to the deterministic solution.

Kharmanda and Olhoff (2002) developed a concept of reliability-based topology optimization, where a probabilistic term is added as a constraint while considering the objective function as deterministic. This concept was also explored by Maute and Frangopol (2003) and Jung and Cho (2004). The former work considers uncertainties in loading, material properties and boundary conditions for the design of complaint mechanisms. In Jung and Cho (2004), the deterministic topology optimization problem is modified so that the objective function is defined as a probabilistic performance measure, which yields the failure probability. As optimization constraint, a maximum allowable probability of design violation is evaluated. Results provided by this work also show designs with extra reinforcements when compared to the deterministic results.

The work of Chen, Chen, and Lee (2010) explored random field uncertainty in loading and material properties for shape and topology optimization. In this work the optimization problem is modeled for the minimization of an objective function composed by two parts: mean value and standard deviation of the objective function under the uncertainty field.

Works signed by Boyan Stefanov Lazarov, Schevenels, and Sigmund (2011) and Boyan S Lazarov, Schevenels, and Sigmund (2012) explored manufacturing uncertainty, accounting for geometrical variation using the collocation method. B. S. Lazarov, M. Schevenels, and O. Sigmund (2012) also explores the use of the perturbation method as an alternative for computational cost reduction.

More recently, further studies were done in the area of robust design by Wu et al. (2016) for unknown-but-bounded design parameters, using the Chebyshev interval method. Also, the work of Cardoso, Silva, and Beck (2019) investigated the robust design of compliant mechanisms considering uncertainties in the output stiffness, where probabilistic and non-probabilistic formulations are compared. The probabilistic approach presented in Cardoso, Silva, and Beck (2019) is the base for the robust formulation of this work.

The robust design approach associated to the dynamic compliance minimization was explored and evaluated in the work of Zhang, Kang, and Zhang (2016). Unknown-but-bounded design inputs were treated using the non-probabilistic ellipsoid convex model. The optimization process targets the design of structures for the worst case scenario given by the input uncertainties. This is ensured by means of running two loops, being the inner loop the responsible for seeking the worst case combination and the outer loop for designing the structure for the combination found by the inner loop.

Using the results of these previous works as a basis, a formulation is proposed for the design of structures with robust dynamic behavior with respect to harmonic loading with uncertainty in the excitation frequency. The proposal relies on the well-known Monte Carlo Simulation method with stratified sampling, in combination with the density-weighted norm. While the Monte Carlo Simulations provide data for robustness improvements, the density-weighted norm precisely identifies resonances and hinders the appearance of non-physical modes in void regions. Since the density-weighted norm does not solve the well-known problem of discontinuous topologies, static compliance is added as a weighted part of the objective function.

1.2 CONTRIBUTIONS

Main contributions are:

- Monte Carlo Simulation with Stratified Sampling method: in order to improve results consistency while reducing computation cost of the Monte Carlo Simulation (MCS) method, a modification has been made to the original MCS formulation (CARDOSO; SILVA; BECK, 2019);
- Formulation for robust design of non-resonant structures: development of an effective objective function, gathering a robust parcel and static compliance. The robust term consists on minimizing both the expected value and standard deviation of density-weighted norm;
- Formulation for robust design of resonant structures: development of an effective objective function, gathering a robust parcel and static compliance. The robust term consists on maximizing the expected value while minimizing the standard deviation of density-weighted norm.

Discussions about the first and second topics have been gathered in the format of a technical article. Its publication was accepted by the journal Computer Methods in Applied Mechanics and Engineering (CMAME) in March 7th, 2021 (VALENTINI; CARDOSO; SILVA, 2021).

1.3 THESIS OUTLINE

Chapter 1 provides an overall understanding and main motivation for the development of this work. It also provides a summary about the history of studies related to the topics herein evaluated, with highlights of the most important methods and outcomes of the referred works.

In Chapter 2, an overview about elastodynamics and finite element discretization is provided, followed by the definition of the harmonic problem.

The concepts about general optimization, optimality criteria and the Augmented Lagrangian method are explored in Chapter 3.

Chapter 4 discusses the main ideas related to topology optimization applied to harmonic problems. Thus, material parametrization is discussed, together with a description of filtering and projection techniques. Additionally, one specific deterministic approach of topology optimization related to harmonic problems is presented and discussed.

A description about uncertainty and its main related concepts is provided in Chapter 5, discussing the mathematical definitions of expected value and standard deviation, measures of great importance for the formulation herein used. Such formulation and respective sensitivity analysis are presented in Chapter 6.

With these definitions, the objective function can be presented and discussed, as well as the optimization method and its sensitivity analysis, in Chapter 7. Finally, in Chapter 8, the design cases considered in this work are presented and evaluated.

2 DYNAMIC EQUILIBRIUM PROBLEM

In this section, the finite element formulation is derived, the chosen finite element type is presented and the harmonic problem is properly defined.

2.1 ELASTODYNAMICS

Applying the linear momentum conservation over an infinitesimal material portion of a given body subjected to external and internal loads and a general acceleration dependent on the time t, one has the resulting balance equation

$$\boldsymbol{\nabla} \cdot \boldsymbol{\sigma}(t) + \mathbf{b}(t) = \rho \ddot{\mathbf{u}}(t), \tag{1}$$

where $\boldsymbol{\sigma}(t)$ is the Cauchy stress tensor, $\mathbf{b}(t)$ is the body internal forces, ρ is the material density, considered constant throughout the portion under study, and $\ddot{\mathbf{u}}(t)$ is the acceleration vector. Adding viscous forces contribution, a new term appears in the right side of Eq. (1), such that

$$\boldsymbol{\nabla} \cdot \boldsymbol{\sigma}(t) + \mathbf{b}(t) = \rho \ddot{\mathbf{u}}(t) + \alpha \rho \dot{\mathbf{u}}(t), \tag{2}$$

where α is a mass-proportionality constant and $\dot{\mathbf{u}}(t)$ is the velocity vector.

The infinitesimal strain $\boldsymbol{\varepsilon}(t)$ actuating over the material portion can be defined as a function of displacements $\mathbf{u}(t)$, as

$$\boldsymbol{\varepsilon}(t) = \frac{1}{2}\left(\boldsymbol{\nabla}\mathbf{u}(t)^T + \boldsymbol{\nabla}\mathbf{u}(t)\right) = \boldsymbol{L}\left(\mathbf{u}(t)\right), \tag{3}$$

where $\boldsymbol{L}(\cdot)$ is a differential operator that carries information of about how two points within the material domain move with respect to each other under loading. Similarly, the strain rate $\dot{\boldsymbol{\varepsilon}}(t)$ is defined as

$$\dot{\boldsymbol{\varepsilon}}(t) = \boldsymbol{L}\left(\dot{\mathbf{u}}(t)\right). \tag{4}$$

Considering both elastic and viscous terms, the total actuating stress can be defined as

$$\boldsymbol{\sigma}(t) = \boldsymbol{\sigma}^E(t) + \boldsymbol{\sigma}^V(t) \tag{5}$$

where $\boldsymbol{\sigma}^E(t)$ is the stress implied by the material elastic properties, therefore, related to the strain $\boldsymbol{\varepsilon}(t)$. Also, $\boldsymbol{\sigma}^V(t)$ is related to viscous properties, which implies dependency on the strain rate $\dot{\boldsymbol{\varepsilon}}(t)$. Thus, the isotropic linear constitutive tensor $\mathbf{D}$ is defined as a function of both the strain and the strain rate

$$\boldsymbol{\sigma}(t) = \mathbf{D} : \left(\boldsymbol{\varepsilon}(t) + \beta\dot{\boldsymbol{\varepsilon}}(t)\right) \tag{6}$$

with the additional proportionality constant β.

Substituting Eqs. (3) and (4) in Eq. (6), and the resulting expression in Eq. (2), the linear momentum equilibrium is more completely derived, such as

$$\boldsymbol{\nabla} \cdot \left(\boldsymbol{D} : \left(\mathbf{L}\left(\mathbf{u}(t) + \beta\dot{\mathbf{u}}(t)\right)\right)\right) + \mathbf{b}(t) = \rho\ddot{\mathbf{u}}(t) + \alpha\rho\dot{\mathbf{u}}(t). \tag{7}$$

For the solution of this second order differential equation, the weighted residues method can be used. As a consequence, to obtain the weak form of the referred equation, an approximation of the displacements vector is defined as $\tilde{\mathbf{u}}(t)$, leading to the residue $\boldsymbol{r}(t)$, defined as

$$\mathbf{r}(t) = \boldsymbol{\nabla} \cdot \left(\boldsymbol{D} : \left(\mathbf{L}\left(\tilde{\mathbf{u}}(t) + \beta\dot{\tilde{\mathbf{u}}}(t)\right)\right)\right) + \mathbf{b}(t) - \rho\ddot{\tilde{\mathbf{u}}}(t) - \alpha\rho\dot{\tilde{\mathbf{u}}}(t). \tag{8}$$

For the convergence, the inner product of the residue with a vector field test function $\mathbf{w}$ must tend to zero, as

$$\int_\Omega \mathbf{w} \cdot \mathbf{r}(t)\, d\Omega \rightharpoonup 0, \tag{9}$$

where Ω is the volume domain. Inserting Eq. (8) in Eq. (9) leads to

$$\begin{aligned} \int_\Omega \mathbf{w} \cdot \left[\boldsymbol{\nabla} \cdot \left(\boldsymbol{D} : \left(\mathbf{L}\left(\tilde{\mathbf{u}}(t) + \beta\dot{\tilde{\mathbf{u}}}(t)\right)\right)\right)\right] d\Omega + \int_\Omega \mathbf{w} \cdot \mathbf{b}(t) d\Omega \\ - \int_\Omega \mathbf{w} \cdot \rho\ddot{\tilde{\mathbf{u}}}(t)\, d\Omega - \int_\Omega \mathbf{w} \cdot \alpha\rho\dot{\tilde{\mathbf{u}}}(t)\, d\Omega = 0. \end{aligned} \tag{10}$$

Integrating by parts the first term of Eq. (10), results in

$$\begin{aligned} \int_\Omega \mathbf{w} \cdot \left[\boldsymbol{\nabla} \cdot \left(\boldsymbol{D} : \left(\mathbf{L}\left(\tilde{\mathbf{u}}(t) + \beta\dot{\tilde{\mathbf{u}}}(t)\right)\right)\right)\right]\, d\Omega = \int_\Gamma \mathbf{w} \cdot \mathbf{t_c} d\Gamma \\ - \int_\Omega \mathbf{L}\left(\mathbf{w}\right) : \mathbf{D} : \left(\mathbf{L}\left(\tilde{\mathbf{u}}(t) + \beta\dot{\tilde{\mathbf{u}}}(t)\right)\right) d\Omega \end{aligned} \tag{11}$$

where Γ is the boundary of Ω. After simplifications and using the quadratic form vector equivalent, the complete form of the weak problem is derived. Using Voigt notation and $\mathbf{u}(t)$ in place of $\tilde{\mathbf{u}}(t)$ for simplifying the notation, the resultant expression is given as

$$\begin{aligned} \int_\Omega \mathbf{L}_V\left(\mathbf{w}\right) \cdot \mathbf{D}\mathbf{L}_V\left(\mathbf{u}(t) + \beta\dot{\mathbf{u}}(t)\right)\, d\Omega + \int_\Omega \mathbf{w} \cdot \rho\ddot{\mathbf{u}}(t)\, d\Omega + \int_\Omega \mathbf{w} \cdot \alpha\rho\dot{\mathbf{u}}(t)\, d\Omega \\ = \int_\Omega \mathbf{w} \cdot \mathbf{b}(t)\, d\Omega + \int_\Gamma \mathbf{w} \cdot \mathbf{t_c}\, d\Gamma. \end{aligned} \tag{12}$$

where the differential operator is represented in Voigt notation as $\mathbf{L}_V$ and the constitutive tensor $\mathbf{D}$ is a matrix.

2.2 FINITE ELEMENT DOMAIN DISCRETIZATION

Consider a domain Ω which is divided in a finite number of smaller sections, being these sections called the finite elements. Thus, consider one finite element e and the related field vector $\mathbf{u}_{int}(t)$, dependent on the time t, which describes the displacements within the element, such that

$$\mathbf{u}_{int}(t) = \mathbf{N}\mathbf{u}_e(t) \tag{13}$$

where $\mathbf{N}$ is a matrix with interpolation functions and $\mathbf{u}_e(t)$ contains the nodal discrete values of displacements implied by the surroundings. Analogously, the vector field $\mathbf{w}$, velocities $\dot{\mathbf{u}}_{int}(t)$ and accelerations $\ddot{\mathbf{u}}_{int}(t)$ are also described by the interpolation functions of $\mathbf{N}$, in the form

$$\mathbf{w} = \mathbf{N}\mathbf{W}_e, \tag{14}$$

$$\dot{\mathbf{u}}_{int}(t) = \mathbf{N}\dot{\mathbf{u}}_e(t) \tag{15}$$

and

$$\ddot{\mathbf{u}}_{int}(t) = \mathbf{N}\ddot{\mathbf{u}}_e(t). \tag{16}$$

Inserting these expressions in Eq. (12), gives

$$\begin{aligned}\int_{\Omega_e} \mathbf{L}_V\left(\mathbf{N}\mathbf{W}_e\right) \cdot \mathbf{D}\mathbf{L}_V\left(\mathbf{N}\mathbf{u}_e(t) + \beta\mathbf{N}\dot{\mathbf{u}}_e(t)\right)\, d\Omega_e + \int_{\Omega_e} \mathbf{N}\mathbf{W}_e \cdot \rho\mathbf{N}\ddot{\mathbf{u}}_e(t)\, d\Omega_e \\ + \int_{\Omega_e} \mathbf{N}\mathbf{W}_e \cdot \alpha\rho\mathbf{N}\dot{\mathbf{u}}_e(t)\, d\Omega_e = \int_{\Omega_e} \mathbf{N}\mathbf{W}_e \cdot \mathbf{b}(t)\, d\Omega_e + \int_{\Gamma_e} \mathbf{N}\mathbf{W}_e \cdot \mathbf{t_c}\, d\Gamma_e.\end{aligned} \tag{17}$$

where Ω_e and Γ_e are, respectively, the volume and boundary of element e. Taking advantage of the fact that Voigt notation is used, it is possible to write $\mathbf{w} \cdot \mathbf{u}_{int}$ as $\mathbf{w}^T \cdot \mathbf{u}_{int}$. Eq. (17) can be rewritten as

$$\begin{aligned}\mathbf{W}_e^T \int_{\Omega_e} \mathbf{L}_V\mathbf{N}^T\mathbf{D}\mathbf{L}_V\mathbf{N}\mathbf{u}_e(t)\, d\Omega_e + \mathbf{W}_e^T \int_{\Omega_e} \mathbf{L}_V\mathbf{N}^T\mathbf{D}\mathbf{L}_V\beta\mathbf{N}\dot{\mathbf{u}}_e(t)\, d\Omega_e \\ +\mathbf{W}_e^T \int_{\Omega_e} \mathbf{N}^T\rho\mathbf{N}\ddot{\mathbf{u}}_e(t)\, d\Omega_e + \mathbf{W}_e^T \int_{\Omega_e} \mathbf{N}^T\alpha\rho\mathbf{N}\dot{\mathbf{u}}_e(t)\, d\Omega_e = \\ \mathbf{W}_e^T \int_{\Omega_e} \mathbf{N}^T\mathbf{b}(t)\, d\Omega_e + \mathbf{W}_e^T \int_{\Gamma_e} \mathbf{N}^T\mathbf{t_c}\, d\Gamma_e,\end{aligned} \tag{18}$$

or in its compact form

$$\mathbf{W}_e^T\mathbf{M}_e\ddot{\mathbf{u}}_e(t) + \mathbf{W}_e^T\mathbf{C}_e\dot{\mathbf{u}}_e(t) + \mathbf{W}_e^T\mathbf{K}_e\mathbf{u}_e(t) = \mathbf{W}_e^T\mathbf{f}_e(t), \tag{19}$$

where $\mathbf{M}_e$, $\mathbf{K}_e$ and $\mathbf{C}_e$ are, respectively, the mass, stiffness and damping matrices of the element and $\mathbf{f}_e(t)$ is the force vector. Each of these local matrices and vector are defined as

$$\mathbf{M}_e = \int_{\Omega_e} \mathbf{N}^T\rho\mathbf{N}\, d\Omega_e, \tag{20}$$

$$\mathbf{K}_e = \int_{\Omega_e} \mathbf{L}_V\mathbf{N}^T\mathbf{D}\mathbf{L}_V\mathbf{N}\, d\Omega_e, \tag{21}$$

$$\mathbf{C}_e = \alpha\mathbf{M}_e + \beta\mathbf{K}_e \tag{22}$$

and

$$\mathbf{f}_e(t) = \int_{\Gamma_e} \mathbf{N}^T\mathbf{t_c}\, d\Gamma_e + \int_{\Omega_e} \mathbf{N}^T\mathbf{b}(t)\, d\Omega_e. \tag{23}$$

From Eq. (18), which is written for a single element e, it is possible to define a global equation, that models the entire domain Ω. To this goal, an operator $\mathbf{H}_e$ can be defined to map the local element vectors into global domain vectors. As an example, local displacements $\mathbf{u}_e(t)$ are mapped to the domain global displacements vector $\mathbf{u}(t)$, such as

$$\mathbf{u}_e(t) = \mathbf{H}_e\mathbf{u}(t). \tag{24}$$

Thus, applying the operator in Eq. (19) and making the summation, results in

$$\begin{aligned}\sum_{e=1}^{ne} (\mathbf{H}_e\mathbf{W})^T \mathbf{M}_e\mathbf{H}_e\ddot{\mathbf{u}}(t) + (\mathbf{H}_e\mathbf{W})^T \mathbf{C}_e\mathbf{H}_e\dot{\mathbf{u}}(t) + (\mathbf{H}_e\mathbf{W})^T \mathbf{K}_e\mathbf{H}_e\mathbf{u}(t) = \\ \sum_{e=1}^{ne} (\mathbf{H}_e\mathbf{W})^T \mathbf{f}_e(t),\end{aligned} \tag{25}$$

where ne is the number of elements in the domain.

Simplifying the notation, Eq. (25) can be rewritten as

$$\mathbf{W}^T\mathbf{M}\ddot{\mathbf{u}}(t) + \mathbf{W}^T\mathbf{C}\dot{\mathbf{u}}(t) + \mathbf{W}^T\mathbf{K}\mathbf{u}(t) = \mathbf{W}^T\mathbf{f}(t), \tag{26}$$

with the global mass, damping and stiffness matrices, respectively

$$\mathbf{M} = \sum_{e=1}^{ne} \mathbf{H}_e^T\mathbf{M}_e\mathbf{H}_e, \tag{27}$$

$$\mathbf{C} = \sum_{e=1}^{ne} \mathbf{H}_e^T\mathbf{C}_e\mathbf{H}_e \tag{28}$$

and

$$\mathbf{K} = \sum_{e=1}^{ne} \mathbf{H}_e^T\mathbf{K}_e\mathbf{H}_e. \tag{29}$$

Additionally, the global force vector is defined as

$$\mathbf{f}(t) = \sum_{e=1}^{ne} \mathbf{H}_e^T\mathbf{f}_e(t). \tag{30}$$

Since $\mathbf{W}^T$ exists in all terms of Eq. (26), it can be further simplified to the linear system

$$\mathbf{M}\ddot{\mathbf{u}}(t) + \mathbf{C}\dot{\mathbf{u}}(t) + \mathbf{K}\mathbf{u}(t) = \mathbf{f}(t). \tag{31}$$

2.2.1 Finite Element Definition

Incompatible elements are chosen for the domain discretization because of improved accuracy, specially for modeling bending of slim reinforcements, which avoids the necessity of using higher order elements and the consequent higher computational cost (BATHE, 2014).

A four-node quadrilateral isoparametric element, defined by Chandrupatla et al. (2002), is herein used considering 2 complementary nodes from where the additional displacements $\boldsymbol{\alpha}$, size 4×1, are computed (BATHE, 2014). Thus, instead of 8 DOFs as

Figure 1 – Finite Element

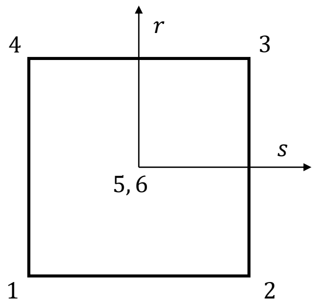

Source: Author production.

the regular element, the incompatible element has 12 DOFs. The additional information derived from the 2 additional nodes is used to improve the displacements computed by the regular 4 nodes, giving to the element higher capability of providing a more accurate description of the material behavior under loading.

The element is depicted in Fig. 1 and its interpolation functions are defined as

$$N_i = \frac{1}{4}(1 \pm r)(1 \pm s) \qquad i = 1..4, \tag{32}$$

$$N_5 = 1 - r^2 \tag{33}$$

and

$$N_6 = 1 - s^2. \tag{34}$$

From the classic definition of the local stiffness matrix,

$$\mathbf{K}_e = \int_{\Omega_e} \mathbf{B}^T \mathbf{E}_e \mathbf{B} d\Omega, \tag{35}$$

where $\mathbf{E}_e$ is the elasticity tensor, Ω_e is the element domain and $\mathbf{B}$ is the strain-displacement matrix, defined as

$$\mathbf{B} = \begin{bmatrix} \mathbf{B}_d & \mathbf{B}_\alpha \end{bmatrix}, \tag{36}$$

with

$$\mathbf{B}_d = \begin{bmatrix} \mathbf{B}_e^1 & \mathbf{B}_e^2 & \mathbf{B}_e^3 & \mathbf{B}_e^4 \end{bmatrix}. \tag{37}$$

which refers to the 4 standard nodes and

$$\mathbf{B}_\alpha = \begin{bmatrix} \mathbf{B}_e^5 & \mathbf{B}_e^6 \end{bmatrix} \tag{38}$$

that refers to the 2 additional nodes. Thus, the expanded local stiffness matrix $\mathbf{K}_{exp}^0$, size 12×12, is defined as

$$\mathbf{K}_{exp}^0 = \begin{bmatrix} \mathbf{K}_{dd_{(8\times8)}} & \mathbf{K}_{d\alpha_{(8\times4)}} \\ \mathbf{K}_{\alpha d_{(4\times8)}} & \mathbf{K}_{\alpha\alpha_{(4\times4)}} \end{bmatrix}, \tag{39}$$

where $\mathbf{K}_{dd}$ refers to the regular 4 nodes, $\mathbf{K}_{d\alpha} = \mathbf{K}_{\alpha d}^T$ and $\mathbf{K}_{\alpha\alpha}$ is related to the additional nodes.

Considering that there is no loading associated to the additional nodes, the equilibrium problem can be written as

$$\begin{bmatrix} \mathbf{K}_{dd_{(8\times8)}} & \mathbf{K}_{d\alpha_{(8\times4)}} \\ \mathbf{K}_{\alpha d_{(4\times8)}} & \mathbf{K}_{\alpha\alpha_{(4\times4)}} \end{bmatrix} \begin{pmatrix} \mathbf{q} \\ \boldsymbol{\alpha} \end{pmatrix} = \begin{pmatrix} \mathbf{f} \\ \mathbf{0} \end{pmatrix}, \tag{40}$$

from which one can define

$$\mathbf{K}_{\alpha d}\mathbf{q} + \mathbf{K}_{\alpha\alpha}\boldsymbol{\alpha} = \mathbf{0}. \tag{41}$$

Solving for $\boldsymbol{\alpha}$ leads to

$$\boldsymbol{\alpha} = -\mathbf{K}_{\alpha\alpha}^{-1}\mathbf{K}_{\alpha d}\mathbf{q}. \tag{42}$$

Thus, finalizing the Static Condensation process by inserting Eq. (42) in Eq. (40), the condensed local stiffness matrix, size 8×8, can be obtained as

$$\mathbf{K}^0 = \left[\mathbf{K}_{\alpha\alpha} - \mathbf{K}_{d\alpha}\mathbf{K}_{\alpha\alpha}^{-1}\mathbf{K}_{\alpha d}\right], \tag{43}$$

which considers information from the incompatible modes and is used to build the global stiffness matrix of the structure.

2.3 HARMONIC PROBLEM DEFINITION

The discrete form of the equilibrium equation for an n Degrees of Freedom (DOFs) linear elastic problem is described by Eq. (31). Thus, consider a structure with linear response with respect to an excitation loading. When it is harmonic,

$$\mathbf{f}(t) = \mathbf{F}e^{i\omega t}, \tag{44}$$

with amplitude $\mathbf{F}$ and angular frequency ω, the permanent response has the same frequency as the excitation and is given by

$$\mathbf{u}(t) = \mathbf{U}e^{i\omega t}, \tag{45}$$

where $\mathbf{U}$ is the complex vector of displacement amplitudes.

Equations (44) and (45), together with the velocity $\dot{\mathbf{u}}(t) = i\omega\mathbf{U}e^{i\omega t}$ and the acceleration $\ddot{\mathbf{u}}(t) = -\omega^2\mathbf{U}e^{i\omega t}$, can be then inserted in Eq. (31) resulting in

$$\left(-\omega^2\mathbf{M} + i\omega\mathbf{C} + \mathbf{K}\right)\mathbf{U}e^{i\omega t} = \mathbf{F}e^{i\omega t}. \tag{46}$$

From Eq. (46), with further simplification, it is possible to notice the linear system

$$\mathbf{K_D}\mathbf{U} = \mathbf{F}, \tag{47}$$

where $\mathbf{K_D}$ is the dynamic stiffness matrix

$$\mathbf{K_D} = -\omega^2\mathbf{M} + i\omega\mathbf{C} + \mathbf{K}, \tag{48}$$

which has a non-linear dependency on the excitation frequency ω. Thus, small perturbations on ω can lead to large changes in the dynamic response $\mathbf{U}$, impacting the effectiveness of any design obtained for a specific excitation frequency value. This is the main motivation of this work: the design of structures less sensitive to variation with respect to ω.

Additional harmonic loads $\mathbf{F}$ with different phases could be considered, however, in this work a system with a single harmonic load is evaluated for simplicity.

3 GENERAL OPTIMIZATION

Optimization is a set of methods that objectives finding the extreme value of a function evaluated in a given domain while complying with one or more constraints. In the following subsections, the generals of optimization and optimality criteria are described followed by a discussion about the optimization method used in this work.

3.1 OPTIMIZATION PROBLEM DEFINITION AND OPTIMALITY CRITERIA

The format of a general optimization problem is defined by Jasbir S Arora (2007) as

$$\begin{aligned} \underset{\boldsymbol{x}}{\text{minimize}} \quad & f(\boldsymbol{x}) \\ \text{subject to} \quad & h_k(\boldsymbol{x}) = 0 \quad k = 1..N_h, \\ & g_j(\boldsymbol{x}) \leq 0 \quad j = 1..N_g, \\ & \boldsymbol{x}_l \leq \boldsymbol{x} \leq \boldsymbol{x}_u. \end{aligned} \tag{49}$$

where $f(\boldsymbol{x})$ is the objective function, dependent of the design variables $\boldsymbol{x}$, and subjected to N_h equality constraints and N_g inequality constraints. Also, $\boldsymbol{x}_l$ and $\boldsymbol{x}_u$ are, respectively, the vectors with the lower and upper bounds of the design variables.

From the general optimization problem, it is possible to write the equivalent Lagrangian function, according to Jasbir S Arora (2007), as

$$\mathcal{L}(\boldsymbol{x}, \boldsymbol{\lambda}_L, \boldsymbol{\mu}) = f(\boldsymbol{x}) + \sum_{k=1}^{N_h} \lambda_{Lj} h_k(\boldsymbol{x}) + \sum_{j=1}^{N_g} \mu_j g_j(\boldsymbol{x}), \tag{50}$$

where $\boldsymbol{\lambda}_L$ is the vector of Lagrange multipliers related to each equality constraint and $\boldsymbol{\mu}$ is the vector with the Kuhn-Tucker multipliers related to each inequality constraint.

Such problem can be considered solved when a stationary point is found, in which the Karush-Kuhn-Tucker (KKT) conditions are satisfied. Thus, making the assumption that $f(\boldsymbol{x})$, $h_k(\boldsymbol{x})$ and $g_j(\boldsymbol{x})$ are twice differentiable at the local optimum point $\boldsymbol{x}^*$, the KKT conditions are satisfied when the following conditions are achieved:

- Stationarity: derivative of the Lagrangian function equals to zero

$$\frac{df(\boldsymbol{x}^*)}{dx_m} + \sum_{k=1}^{N_h} \lambda_{Lj}^* \frac{dh_k(\boldsymbol{x}^*)}{dx_m} + \sum_{j=1}^{N_g} \mu_j^* \frac{dg_j(\boldsymbol{x}^*)}{dx_m} = 0 \tag{51}$$

- Primal feasibility: Constraints satisfied

$$h_k(\boldsymbol{x}^*) = 0, \ \forall \ k; \tag{52}$$

$$g_j(\boldsymbol{x}^*) \leq 0, \ \forall \ j; \tag{53}$$

- Dual feasibility: Multipliers greater than or equal to zero

$$\mu_j^* \geq 0, \ \forall \ j; \tag{54}$$

- Complementary Slackness: product of the Lagrange multipliers and the inequality constraints is zero

$$\mu_j^* g_j(\boldsymbol{x}^*) = 0,\ \forall\ j; \tag{55}$$

- Regular Point: The gradients of the active constraints are linearly independent.

The design point $\boldsymbol{x}^*$ is a local optimum if all these conditions are satisfied.

3.2 SOLUTION STRATEGY

According to Jasbir Singh Arora (2004), an optimization process consists in iteratively update the design variables until the local minima is identified, such that

$$\boldsymbol{x}^{k+1} = \boldsymbol{x}^k + \alpha^k \boldsymbol{d}^k \tag{56}$$

where $\alpha^k > 0$ is the step in the optimization search direction $\boldsymbol{d}^k$.

Also, Jasbir Singh Arora (2004) defines that, to be accepted as the next optimal point, it must satisfy the condition

$$f(\boldsymbol{x}^{k+1}) = f(\boldsymbol{x}^k + \alpha^k \boldsymbol{d}^k) < f(\boldsymbol{x}^k), \tag{57}$$

which can be written as a linear expansion via Taylor's series, such that

$$f(\boldsymbol{x}^k) + \nabla f(\boldsymbol{x}^k) \cdot \alpha^k \boldsymbol{d}^k < f(\boldsymbol{x}^k). \tag{58}$$

Thus, it is possible to use the sensitivity analysis of the objective function to define the search direction $\boldsymbol{d}^k$. The most obvious choice for it is named as Steepest Descent, defined as

$$\boldsymbol{d}^k = -\nabla f(\boldsymbol{x}^k). \tag{59}$$

The computation of the next optimal point as per Eq. 56 depends also on the solution of α^k. For unconstrained problems, it can be simply defined as $\alpha^k = argmin\left(f(\boldsymbol{x}^k + \alpha^k \boldsymbol{d}^k)\right)$, however, since in this work side constraints are considered, the following considerations shall be made:

- The step size shall not cause violation of any side constraint;
- In case a design variable is already at one of the limit boundaries and the gradient imposes that the variable violates the side constraint, the gradient at this position must be blocked.

In this work, the optimization step α^k is determined using the Armijo's Backtracking technique (ARMIJO, 1966), such that

$$f(\tilde{\boldsymbol{x}}^{k+1}) \approx f(\boldsymbol{x}^k) + \nabla f(\boldsymbol{x}^k) \cdot |\Delta \boldsymbol{x}^k|_S = f(\boldsymbol{x}^k) + \nabla f(\boldsymbol{x}^k) \cdot |\alpha^k \boldsymbol{d}^k|_S, \tag{60}$$

where the operator $|\cdot|_S$ is responsible for blocking variables at their side constraints. The optimization step α^k is accepted when

$$f(\boldsymbol{x}^k + |\alpha^k \boldsymbol{d}^k|_S) \leq f(\boldsymbol{x}^k) + c\nabla f(\boldsymbol{x}^k) \cdot |\alpha^k \boldsymbol{d}^k|_S, \tag{61}$$

with $c \in [0, 1]$. In case the condition is not satisfied, the step is reduced by $\alpha^{k+1} = \tau\alpha^k$, where $\tau \in [0, 1]$, until the condition is achieved.

3.3 AUGMENTED LAGRANGIAN METHOD

The Augmented Lagrangian (AL) method is chosen to be used in this work, such that a constrained optimization problem, as the one defined in Eq. (49), can be rewritten as a sequence of unconstrained optimization problems by the addition of all constraints into the Lagrangian function by the use of Lagrangian multipliers and penalization factors.

For further clarification, consider the optimization problem given by Eq. (49), but with only inequality constraints and considering the constraint limit value $\bar{g}_j$

$$\begin{aligned} \underset{\boldsymbol{x}}{\text{minimize}} \quad & f(\boldsymbol{x}) \\ \text{subject to} \quad & g_j(\boldsymbol{x}) \leq \bar{g}_j \;\; j = 1..N_g, \\ & \boldsymbol{x}_l \leq \boldsymbol{x} \leq \boldsymbol{x}_u. \end{aligned} \tag{62}$$

The referred optimization problem can be rewritten as

$$\mathcal{L}(\boldsymbol{x}, \boldsymbol{\mu}, \boldsymbol{r}) = f(\boldsymbol{x}) + \frac{1}{2} \sum_{j=1}^{Ng} r_j \left\langle \frac{\mu_j}{r_j} + g_j(\boldsymbol{x}) - \bar{g}_j \right\rangle^2, \tag{63}$$

which is one of the Augmented Lagrangian forms discussed in the literature (BIRGIN; MARTÍNEZ, 2014). In the equation, r_j is a penalization factor related to the j-th constraint and $\langle a \rangle = \max(a, 0)$.

According to Birgin and Martínez (2014), the AL problem is preferably solved by the use of an inner and an outer loop. In the inner loop, the problem is solved with both the Lagrange multipliers and the penalization factors kept constant up to the moment in which the optimum is found. Once it happens, both the penalty factor and the Lagrange multipliers are updated in an outer loop such that the inner loop can be reinitialized. This process happens multiple times up to the moment in which the optimum is finally found.

Following Birgin and Martínez (2014), the multipliers update is done according to

$$\mu_j^{(q+1)} = \left\langle \mu_j^q + r^{(q)} \left(g_j(\boldsymbol{x}) - \bar{g} \right) \right\rangle, \tag{64}$$

where q is the number of the current outer iteration. Furthermore, also according to Birgin and Martínez (2014), the update of the penalization factors is dependent on the computation of

$$V^q = max \left(g_j(\boldsymbol{x}), -\frac{\mu_j}{r_j} \right), \tag{65}$$

such that the update is done when $V^q > V^{q-1}$, as per

$$r_j^{(q+1)} = \kappa r_j^{(q)}, \quad \kappa > 1, \tag{66}$$

where κ is a constant larger than unity. It is important to notice that κ and $r_j^{(0)}$ are generally not defined by a fixed rule and depend on the type of problem and constraints. Thus, experiments are required for each problem to choose these parameters.

After testing, the method proposed by Birgin and Martínez (2014) for calculation of $r_j^{(0)}$ presented good results and was incorporated to this work. Per the referred method,

$$r_j^{(0)} = 2 \frac{f(\boldsymbol{x})}{\sum_{j=1}^{Ng} \langle g_j(\boldsymbol{x}) \rangle^2}. \tag{67}$$

One note to be taken is that in the AL first external loop, all Lagrange multipliers are set to zero, leading to a pure penalization optimization process. The update only happens when starting the second loop.

For the AL problem solution, a gradient-based approach is used. Thus, the derivative of the AL equation is demanded,

$$\frac{d\mathcal{L}(\boldsymbol{x},\boldsymbol{\mu},\boldsymbol{r})}{dx_m} = \frac{df(\boldsymbol{x})}{dx_m} + \sum_{j=1}^{Ng} r_j \left\langle \frac{\mu_j}{r_j} + g_j(\boldsymbol{x}) - \bar{g}_j \right\rangle \frac{dg_j(\boldsymbol{x})}{dx_m}. \tag{68}$$

With this derivative, an optimization strategy such as the one described in Section 3.2 can be used to find the best optimization path in each iteration of the inner loops.

The process is ideally stopped when all KKT conditions are met, which is not always possible since a numerical problem is solved. For this work, the first order conditions are verified for confirming if the optimum point candidate can be confirmed to be stationary, such that

$$\left\| \frac{df(\boldsymbol{x}^*)}{dx_m} + \sum_{j=1}^{N_g} \mu_j^* \frac{dg_j(\boldsymbol{x}^*)}{dx_m} \right\| \leq \varepsilon_{AL}. \tag{69}$$

In case the derivative of the AL function is smaller or equal to ε_{AL}, with $\varepsilon_{AL} > 0$, the point is stationary. Such condition is defined as sufficient to confirm optimality to the goals of this work.

4 TOPOLOGY OPTIMIZATION FOR HARMONIC PROBLEMS

Topology optimization is a form of structural optimization that consists in determining the optimal material distribution within a predetermined fixed domain subjected to natural and essential boundary conditions (BENDSØE; KIKUCHI, 1988).

Following Sections contain definitions about key factors in the topology optimization subjected to harmonic loads, such as material definition, length scale filtering and projection and, finally, the damping modeling. Also, the deterministic formulation is presented and discussed.

4.1 MATERIAL PARAMETRIZATION

Since the problem herein solved is dependent on material stiffness and mass characteristics, these two distinct material parametrizations need to be defined. Regarding the stiffness modeling, the SIMP (Solid Isotropic Material with Penalization) parametrization, described by Bendsøe and Sigmund (1999), is used, such that the effective constitutive tensor at the finite element e, $\mathbf{D}_e$, is given by

$$\mathbf{D}_e = \rho_e^p \mathbf{D}^0, \tag{70}$$

where $\mathbf{D}^0$ is the constitutive tensor of the base material, ρ_e is the relative density at element e and p is a positive exponent. Thus, as the relative density ρ_e is constant in each finite element, its stiffness matrix can be written as

$$\mathbf{K}_e(\rho_e) = (\rho_l + (1 - \rho_l)\,\rho_e^p)\,\mathbf{K}_e^0, \tag{71}$$

where $\mathbf{K}_e^0$ is the stiffness matrix of the base material, ρ_l a lower bound used to prevent singularities in the finite element model. The global stiffness matrix is then

$$\mathbf{K}(\boldsymbol{\rho}) = \sum_{e=1}^{ne} \mathbf{H_e}^T \mathbf{K_e}(\boldsymbol{\rho}) \mathbf{H_e}, \tag{72}$$

where ne is the number of elements, $\boldsymbol{\rho}$ is the vector containing all the relative densities, $\mathbf{H_e}$ is a localization matrix and $\mathbf{K_e}$ is the local stiffness of element e.

Regarding the mass parametrization, using a SIMP-like strategy does not produce satisfactory results, as discussed by Pedersen (2000) and Dmitri Tcherniak (2002). The problem is that, if $p > 1$ and ρ_e gets close to zero, the mass-stiffness ratio tends to infinity, leading to unrealistic dynamic responses in void regions.

Based on these previous works, Niels Olhoff and Jianbin Du (2008) proposed a modification in the mass parametrization targeting a relaxed mass-stiffness ratio and a smooth transition for the mass derivative at a given threshold point. The original stiffness parametrization is kept the same while splitting the mass modeling at $\rho_e = \bar{\rho}$, as suggested by Pedersen (2000). The proposed model, based on the work of Niels Olhoff and Jianbin Du (2008), is

$$\mathbf{M}_e(\rho_e) = \begin{cases} (\rho_l + (1 - \rho_l)\,\rho_e)\,\mathbf{M}_e^0, & \text{if } \bar{\rho} < \rho_e \leq 1.0 \\ (\rho_l + (C_1 \rho_e^6 + C_2 \rho_e^7))\,\mathbf{M}_e^0, & \text{if } \rho_e \leq \bar{\rho}, \end{cases} \tag{73}$$

where $\mathbf{M}_e^0$ is the mass matrix of the base material and the constants C_1 and C_2 are given by

$$C_1 = -\frac{6\rho_l - 6}{\bar{\rho}^5} \tag{74}$$

and

$$C_2 = \frac{5\rho_l - 5}{\bar{\rho}^6}, \tag{75}$$

with $\bar{\rho} = 0.1$ (PEDERSEN, 2000). This is the mass parametrization used in this work.

4.2 FILTERING AND PROJECTION

The traditional linear spatial filter, defined in Sigmund (2007), is used to impose a minimum length scale and eliminate checkerboard patterns. Also, the Heaviside projection, studied in Wang, Lazarov, and Sigmund (2011), is used to ensure crispy black and white designs. Thus, the real set of design variables used is given by $\boldsymbol{x} \in \mathbb{R}^{ne}$, which is filtered by the linear spatial filter

$$\tilde{\rho}_e = \frac{\sum_{i\in\vartheta_e} w_{ei} x_i}{\sum_{i\in\vartheta_e} w_{ei}}. \tag{76}$$

where ϑ_e is the set of neighbors of element e within a given radius R. Also, the weights w_{ei} are defined as

$$w_{ei} = \max\left(0, R - \|\mathbf{c}_i - \mathbf{c}_e\|\right), \tag{77}$$

where the centroidal coordinates of elements e and i are given by $\mathbf{c}_e$ and $\mathbf{c}_i$. Intermediate variables $\tilde{\boldsymbol{\rho}}$ are then transformed by a Heaviside-like nonlinear operator

$$\rho_e = \frac{\tanh\left(\beta_H \eta_H\right) + \tanh\left(\beta_H\left(\tilde{\rho}_e - \eta_H\right)\right)}{\tanh\left(\beta_H \eta_H\right) + \tanh\left(\beta_H\left(1 - \eta_H\right)\right)}, \tag{78}$$

where η_H is a threshold value (0.5 in this manuscript) (WANG; LAZAROV; SIGMUND, 2011). For this work, the parameter β_H is subjected to a continuation strategy, as described in Section 8.

Even though the mathematical design variables are given by $\boldsymbol{x}$, all equations are presented as a function of $\boldsymbol{\rho}$, given the fact that sensitivities and equilibrium equations are solved with respect to the relative densities. The only modification is the need to apply a correction to the sensitivities before solving the optimization problem (SIGMUND, 2007; WANG; LAZAROV; SIGMUND, 2011). Thus, the sensitivity of a generic function $f(\boldsymbol{\rho})$ with respect to x_m is evaluated as

$$\frac{df(\boldsymbol{\rho})}{dx_m} = \frac{\partial f(\boldsymbol{\rho})}{\partial \rho_i}\frac{\partial \rho_i}{\partial \tilde{\rho}_j}\frac{d\tilde{\rho}_j}{dx_m}, \tag{79}$$

with implicit sum along indexes i and j.

4.3 DAMPING MODELING

The well-known Rayleigh damping model is written as a linear combination of the global mass and stiffness matrices, in the form $\mathbf{C} = \alpha\mathbf{M} + \beta\mathbf{K}$. Generally, fixed values for the constants α and β are defined to match a given dynamic behavior in a specific problem. However, when it comes to topology optimization this is not possible since both the mass and stiffness matrices are in constant modification along the solution process, making both α and β a function of the current design.

For the definition of α and β during a topology optimization process, the work of Montero, Silva, and Cardoso (2020) proposes a generalization of the original strategy developed by Silva, Neves, and Lenzi (2020). It consists in a structural damping method ($\alpha = 0$) that ensures a reasonable structural damping behavior while always leading to a sub-critical damped system. Thus, the strategy proposed by Montero, Silva, and Cardoso (2020) is defined as

$$\mathbf{C} = \frac{2\zeta}{\omega}\mathbf{K}. \tag{80}$$

This method has the convenience of allowing the damping coefficient configuration with the physical parameter ζ, as defined by Montero, Silva, and Cardoso (2020), which is particularly useful in case damping continuations are adopted for the optimization process, as is the case of this work.

Specially in the initial iterations of the optimization process, the dynamic behavior of the structure is not yet defined and there might be events in which two different resonant modes swap positions, as described in the work of Montero, Silva, and Cardoso (2020). This event creates numerical instabilities due to the ill-conditioning of the dynamic stiffness matrix $\mathbf{K_D}$, specially if the structure is slightly damped. To overcome this issue, a continuation strategy is used in this work, starting the optimization process with a relatively high value for ζ and continuously decreasing it up to the specified value for the problem.

The problem is solved with N_{LA} external loops of the AL method, as described by the flowchart depicted in Fig. 4. For each AL iteration q in the interval defined by $1 \leq q \leq N_\zeta$, a continuation approach of damping coefficient ζ is performed. The effective ζ^q at iteration q is given by

$$\zeta^q = max\left(\zeta_{target}, \frac{q-1}{N_\zeta - 1}\left(\zeta_{target} - \zeta_{ini}\right) + \zeta_{ini}\right), \tag{81}$$

where ζ_{ini} is the initial (large) value for ζ and ζ_{target} is the desired value for ζ.

For this work, the optimization starts with initial damping parameter $\zeta_{ini} = 0.3$, (30%), and the target value is $\zeta_{target} = 0.05$, (5%). The number of continuation steps N_ζ is defined for each design case in the results section.

4.4 SENSITIVITY ANALYSIS OF HARMONIC PROBLEMS

The solution of an optimization problem involving harmonic displacements computations demand the evaluation of the sensitivity of the structure with respect to the design variables. Such methodology was originally proposed by Tortorelli and Micharelis (1994) and Jensen and Pedersen (2005).

The process starts with the adjoint problem definition,

$$\begin{aligned}\Phi(\boldsymbol{\rho}, \mathbf{U}_D(\boldsymbol{\rho}), \mathbf{U}_D^*(\boldsymbol{\rho})) = \Phi(\boldsymbol{\rho}) &+ \frac{1}{2}\boldsymbol{\lambda}_1^T\left(\mathbf{K}_D(\boldsymbol{\rho})\mathbf{U}_D(\boldsymbol{\rho}) - \mathbf{F}_0(\boldsymbol{\rho})\right) \\ &+ \frac{1}{2}\boldsymbol{\lambda}_2^T\left(\mathbf{K}_D^*(\boldsymbol{\rho})\mathbf{U}_D^*(\boldsymbol{\rho}) - \mathbf{F}_0^*(\boldsymbol{\rho})\right).\end{aligned} \tag{82}$$

In the equation, Φ is the dynamic function and $\boldsymbol{\lambda}_1$ and $\boldsymbol{\lambda}_2$ are the adjoint vectors that multiply either the conjugate and non-conjugate dynamic equilibrium equations, being the conjugate terms represented by the "*" sign.

After developing the equations and executing a series of mathematical maneuvers, as detailed in the work of Montero, Silva, and Cardoso (2020), the resulting expression can be defined as

$$\frac{d\Phi}{d\rho_m} = \frac{\partial\Phi}{\partial\rho_m} - Re\left(\boldsymbol{\lambda}^T \frac{d\mathbf{F}_0}{d\rho_m}\right) + Re\left(\boldsymbol{\lambda}^T \frac{d\mathbf{K}_D}{d\rho_m}\mathbf{U}\right), \tag{83}$$

where $\boldsymbol{\lambda}$ is the resulting adjoint term, resultant from a simplification applied to $\boldsymbol{\lambda}_1$ and $\boldsymbol{\lambda}_2$.

As can be seen, to solve the derivative, it is necessary to calculate the expression $\partial\Phi/\partial\rho_m$. Also, it is required to solve the adjoint problem, defined by

$$\mathbf{K}_D\boldsymbol{\lambda} = \left(i\frac{\partial\Phi}{\partial\mathbf{U}_I}^T - \frac{\partial\Phi}{\partial\mathbf{U}_R}^T\right). \tag{84}$$

4.5 DETERMINISTIC APPROACH FOR DYNAMIC DISPLACEMENTS OPTIMIZATION

The work of Montero, Silva, and Cardoso (2020) proposes a formulation for either minimizing or maximizing dynamic responses, based on a linear combination of the density-weighted norm N_{mwdB} and the well-known static compliance $\Upsilon_S = \mathbf{F}^T\mathbf{U}_S$. The proposed optimization problem can be defined as

$$\begin{aligned}
\underset{\boldsymbol{\rho}}{\text{minimize}} \quad & \gamma_1 \frac{N_{mwdB}(\boldsymbol{\rho},\omega)}{N^0_{mwdB}} + \gamma_2 \frac{\Upsilon_S(\boldsymbol{\rho})}{\Upsilon^0_S} \\
\text{subject to} \quad & \mathbf{K}_D(\boldsymbol{\rho},\omega)\,\mathbf{U}(\boldsymbol{\rho},\omega) = \mathbf{F}, \\
& \mathbf{K}(\boldsymbol{\rho})\,\mathbf{U}_S(\boldsymbol{\rho}) = \mathbf{F}, \\
& V(\boldsymbol{\rho}) = \sum_{e=1}^{ne} \rho_e V^0_e \leq \bar{V}, \\
& \boldsymbol{\rho}_l \leq \boldsymbol{\rho} \leq \boldsymbol{\rho}_u,
\end{aligned} \tag{85}$$

where N_{mwdB} and Υ_S are weighted by the constants γ_1 and γ_2, such that $|\gamma_1| + \gamma_2 = 1$. Constant γ_1 is defined as $0 < \gamma_1 \leq 1$ when non-resonant structures are targeted and as $0 > \gamma_1 \geq -1$ otherwise.

Both functions are scaled by their initial values N^0_{mwdB} and Υ^0_S, so that their order of magnitude is similar and dimensionless. Also, $V(\rho)$ is the volume and $\bar{V}$ is its limit value. Additionally, the equilibrium equations $\mathbf{K}_D\mathbf{U} = \mathbf{F}$ and $\mathbf{K}\mathbf{U}_S = \mathbf{F}$ are automatically satisfied during the optimization, since the objective function demands the solution of both equations (the static equilibrium equation is needed to compute Υ_S and the dynamic equilibrium equation is needed to compute N_{mwdB}).

According to Montero, Silva, and Cardoso (2020), the density-weighted norm has great capacity of localizing resonances even for high damping coefficients and the measure is also insensitive to antiresonances, avoiding related premature convergence issues (SILVA; NEVES; LENZI, 2019). Finally, it is able to disregard void regions in the computation of dynamic displacements, eliminating disturbance of the optimization process by eventual high displacements of meaningless modes located at the almost zero-stiffness areas of the domain.

The density-weighted norm is defined as

$$N_{mw}(\mathbf{U}(\omega)) = \left(\sum_{j \in S} \left(u_j^* a_j u_j \right)^{\frac{m}{2}} \right)^{\frac{1}{m}}, \tag{86}$$

where ω is the target angular frequency, u_j is the $j - th$ component of $\mathbf{U}$ and u_j^* is its complex-conjugate counterpart. In this work the set S is comprised of all degrees of freedom of the finite element mesh. The exponent m is always even and aids in the identification of the resonances. The authors recommend that the value of m is carefully chosen to not make it unnecessarily high, which would impose increased non-linear behavior and eventual accuracy problems (MONTERO; SILVA; CARDOSO, 2020).

The term a_j is the responsible for weighting each DOF j by the relative density of the neighbor elements and is written as

$$a_j = \left(\sum_{v_j \in S_j} \rho_{v_j}^{w} \right)^{\frac{1}{w}}, \tag{87}$$

where v_j is the set of elements containing the DOF j and w is a positive exponent.

According to Montero, Silva, and Cardoso (2020), the logarithmic form is preferred, specially for higher excitation frequencies, in which the associated displacements and derivatives are very small. Thus, Eq. (86) is rewritten as

$$N_{mwdB} = c_0 + 10 \log_{10}(N_{mw}), \tag{88}$$

where the factor c_0 is chosen to make the function positive for values of N_{mw} larger than $1 \times 10^{-c_0/10}$. As proposed by Montero, Silva, and Cardoso (2020), a value of 100 is used in this work, such that the function is positive for N_{mw} larger than 1×10^{-10}.

As discussed in the work of Montero, Silva, and Cardoso (2020), this formulation leads to well defined topologies, with extreme dynamic response. However, as any deterministic optimization approach, the process leads to solutions that are really optimized only at the target frequency, not ensuring a smooth, well-behaved dynamic response at neighbor frequencies, as intended in the present work. Thus, a modified formulation is proposed, aiming the design of structures with robust dynamic behavior.

4.5.1 Sensitivity Analysis of the Density-Weighted Norm

The derivative of Eq. (86) with respect to the design variables $\boldsymbol{\rho}$ is detailed in the work of Montero, Silva, and Cardoso (2020), however is integrally presented herein for clarity. The derivative is given as

$$\frac{dN_{mw}}{d\rho_m} = \frac{\tilde{a}}{2} \sum_j \tilde{b}_j \frac{d}{d\rho_m} \left(u_j^* a_j u_j \right), \tag{89}$$

with

$$\tilde{a} = \left(\sum_j \left(u_j^* a_j u_j \right)^{\frac{m}{2}} \right)^{\frac{1}{m} - 1} \tag{90}$$

and

$$b_j = \left(u_j^* a_j u_j\right)^{\frac{m}{2}-1}. \tag{91}$$

Also, u_j is defined as

$$u_j = \mathbf{L_j}^T \mathbf{U} \tag{92}$$

and u_j^* is written as

$$u_j^* = \mathbf{L_j}^T \mathbf{U}^* \tag{93}$$

where $\mathbf{L_j}$ is a localization vector. This leads to

$$\frac{dN_{mw}}{d\rho_m} = \frac{\tilde{a}}{2} \sum_j b_j \left(u_j a_j \mathbf{L}_j^T \frac{d\mathbf{U}^*}{d\rho_m} + u_j^* \frac{da_j}{d\rho_m} u_j + u_j^* a_j \mathbf{L}_j^T \frac{d\mathbf{U}}{d\rho_m} \right), \tag{94}$$

and splitting the complex displacement vector into its real and imaginary components, it gives that

$$\begin{aligned} \frac{dN_{mw}}{d\rho_m} &= \frac{\tilde{a}}{2} \sum_j b_j \left[\left(u_{jR} + i u_{jI}\right) a_j \mathbf{L}_j^T \left(\frac{d\mathbf{U}_R}{d\rho_m} - i \frac{d\mathbf{U}_I}{d\rho_m} \right) \right. \\ &\left. + \left(u_{jR}^2 + u_{jI}^2\right) \frac{da_j}{d\rho_m} + \left(u_{jR} - i u_{jI}\right) a_j \mathbf{L}_j^T \left(\frac{d\mathbf{U}_R}{d\rho_m} + i \frac{d\mathbf{U}_I}{d\rho_m} \right) \right]. \end{aligned} \tag{95}$$

Deriving Eq. (87), results in

$$\frac{da_j}{d\rho_m} = \frac{1}{w} \left(\sum_{v_j} \rho_{v_j}^w \right)^{\frac{1}{w}-1} w \sum_{v_j} \left(\rho_{v_j}^{w-1} \frac{d\rho_{v_j}}{d\rho_m} \right) \tag{96}$$

where v_j is defined as a list of first order elements that are neighbors of the degree-of-freedom j.

Further exploring Eq. (96), it can be simplified as

$$\frac{da_j}{d\rho_m} = A_j \sum_{v_j} \left(\rho_{v_j}^{w-1} \delta_{vm} \right), \tag{97}$$

where

$$A_j = \left(\sum_{v_j} \rho_{v_j}^w \right)^{\frac{1}{w}-1} \tag{98}$$

and

$$\delta_{vm} = \begin{cases} 1, & \text{if } v = m, \\ 0, & \text{if } v \neq m. \end{cases} \tag{99}$$

Inserting Eq. (97) in Eq. (95) and with further simplification

$$
\begin{aligned}
\frac{dN_{mw}}{d\rho_m} = \tilde{a} \sum_j b_j \Bigg[& u_{jR} a_j \mathbf{L}_j^T \frac{d\mathbf{U}_R}{d\rho_m} + u_{jI} a_j \mathbf{L}_j^T \frac{d\mathbf{U}_I}{d\rho_m} \\
& + \frac{1}{2} \left({u_j}_R^2 + {u_j}_I^2 \right) A_j \sum_{v_j} \left(\rho_{v_j}^{w-1} \delta_{vm} \right) \Bigg] .
\end{aligned}
\tag{100}
$$

It is possible now to split the terms as required by the sensitivity analysis for general dynamic problems, given by Eq. (84), as

$$
\frac{\partial N_{mw}}{\partial \mathbf{U}_R} = \tilde{a} \sum_j b_j u_{jR} a_j \mathbf{L}_j^T ,
\tag{101}
$$

and

$$
\frac{\partial N_{mw}}{\partial \mathbf{U}_I} = \tilde{a} \sum_j b_j u_{jI} a_j \mathbf{L}_j^T .
\tag{102}
$$

Thus, the adjoint problem can be written as

$$
\mathbf{K}_D \boldsymbol{\lambda}_N = \left(i \frac{\partial N_{mw}}{\partial \mathbf{U}_I} - \frac{\partial N_{mw}}{\partial \mathbf{U}_R} \right)^T .
\tag{103}
$$

Substituting Eq. (100) into (103) and reorganizing terms,

$$
\mathbf{K}_D \boldsymbol{\lambda}_N = -\tilde{a} \sum_j b_j {u_j}^* a_j \mathbf{L}_j .
\tag{104}
$$

The remaining term is directly added to the derivative, resulting in

$$
\begin{aligned}
\frac{dN_{mw}}{d\rho_m} = & \frac{\tilde{a}}{2} \sum_j b_j \left({u_j}_R^2 + {u_j}_I^2 \right) A_j \sum_{v_j} \left(\rho_{v_j}^{w-1} \delta_{vm} \right) \\
& + Re \left(\boldsymbol{\lambda_N}^T \frac{d\mathbf{K_D}}{d\rho_m} \mathbf{U} \right) - Re \left(\boldsymbol{\lambda_N}^T \frac{d\mathbf{F_0}}{d\rho_m} \right) .
\end{aligned}
\tag{105}
$$

Adapting the resultant equation to the logarithmic scale, Eq. (105) is redefined as

$$
\frac{dN_{mwdB}}{d\rho_m} = 10 \frac{1}{ln(10) N_{mw}} \frac{dN_{mw}}{d\rho_m} .
\tag{106}
$$

5 UNCERTAINTY

Many real-life systems present behavior variation patterns. The spreading rate of a biological disease, the monetary exchange rate fluctuations over a semester, or loadings due to the wind or by earthquakes are examples of external events with uncertain behavior (VANMARCKE, 2010).

Thus, depending on the variations that a physical system is subjected to, a deterministic calculation approach might be insufficient to ensure an accurate representation of the application (SUDRET; DER KIUREGHIAN, 2000). Uncertain parameters can be classified in two distinct groups: aleatoric and epistemic (HORA, 1996). Aleatoric uncertainties are caused by the randomness of a certain event with inherent variability, such as a coin flipping exercise. Epistemic (or systematic) uncertainties are related to the lack of knowledge of a certain event, but with further information or improved modeling, could be mitigated. In other words, aleatoric uncertainties cannot be reduced while epistemic uncertainties can (SHAKER; HÜLLERMEIER, 2020).

There are two main ways of dealing with uncertainties in a given problem: the probabilistic and the non-probabilistic methods. This work considers the probabilistic approach, where the uncertainties are added to the problem as random variables (AGARWAL, 2004). The concepts related to random variables will be further explored in the next subsections of this Chapter.

Since the non-probabilistic method is not covered by this work, the interested reader can refer to the work of Agarwal (2004) for further information.

For engineering applications where uncertain input parameters are adopted, the understanding of their influence on the system response is mandatory for correct interpretation of the results. To this goal, consider a mechanical system $M_s : x_p \rightarrow y_p$ subjected to the uncertain input parameters contained in the random variable X_p. The system response $\mathbf{Y}_p$ is

$$\mathbf{Y}_p = M_s \left(X_p \right), \tag{107}$$

where $\mathbf{Y}_p$ contains the response for each uncertain input contained in X_p.

The understanding of the probabilistic content of the response vector $\mathbf{Y}_p$ is the main goal of the solution methods of probabilistic problems (SUDRET, 2007). According to Sudret (2007), an option for the computation of such response is the application of probabilistic methods of uncertainty propagation, that can generally be divided in three subgroups: complete characterization, response variability and reliability (LOPEZ; BECK, 2013).

Methods related to complete characterization allow for the definition of the probability density such that a very complete understanding of the input data is provided (LOPEZ; BECK, 2013). Katzgraber (2009) defines that a well-known method of complete characterization is the Monte Carlo Simulation (MCS), which is considered a baseline for verification of any other method. The system response characterization is often done by these methods via evaluation of the expected value and a deviation measure, such as the standard deviation, of the function response. These concepts will be explored in Section 5.1.

According to Lopez and Beck (2013), methods that evaluate the response variability have the main goal of determining measures like the expected value and standard deviation of the system response under uncertain input parameters. One can refer to the perturbation method as an example related to this approach (SILVA; CARDOSO, 2016).

Response reliability based methods evaluate measures associated to failure, that could be used as a design constraint, for instance. Examples of reliability based methods are the FORM (First Order Reliability Method) and SORM (Second Order Reliability Method) (DITLEVSEN; MADSEN, 1996).

Following items in this Section define basic fundamentals related to uncertainties, such as the definition of random variable. Also, the related concepts of expected value, variance and standard deviation will be explored. Finally, an overview on the Normal distribution probability function is provided.

5.1 RANDOM VARIABLE

Consider the probability space $(\Omega_p, \mathfrak{F}, P)$, where Ω_p is a sample space that collects all possible events, $\mathfrak{F}$ is a subset of possible events contained in Ω_p, and P is a general probability distribution function that describes how often an event might occur. Consider also $(\Omega'_p, \mathfrak{F}')$ as a subspace of the complete probability space. Then, for every mapping $X : \Omega_p \to \Omega'_p$, a real number $X(\omega_p)$ is associated, called a realization of X, with $\omega_p \in \Omega_p$. So, according to Bauer and Burckel (2011), the mapping function X is called a random variable.

In simpler terms, a random variable is a function that maps, for any event in a partition of the sample space Ω_p, an unique real number, such that $X : \Omega_p \to \mathbb{R}$.

Bauer and Burckel (2011) state that the event $\{X \in \mathfrak{F}\}$ is configured when "X lies in $\mathfrak{F}$" and $P\{X \in \mathfrak{F}\}$ is the probability of such. Thus, to each mapping event, a positive real number $P\{X \in \mathfrak{F}\} \geq 0$ exists, which represents its probability of occurrence. Additionally, listing all possible realizations $X(\omega_p)$ with its associated probability gives the probability distribution of X, defined as P_X.

Moreover, associated to a probability distribution P_X, there is a cumulative distribution $F_X(x)$, defined as

$$F_X(x) = P_X(X \leq x) = P_X(\omega_p \in \Omega_p : X(\omega_p) \leq x), \tag{108}$$

for all $x \in \mathbb{R}$. A random variable X is defined as continuous when a non-negative function $f_X(x)$ exists, such that

$$F_X(x) = \int_{-\infty}^{x} f_X(x)dx, \tag{109}$$

for all $x \in \mathbb{R}$, where $f_X(x)$ is the probability density function of the random variable X. Considering $F_X(x)$ as differentiable, then the probability density function associated to a random variable X can be defined as

$$f_X(x) = \frac{dF_X(x)}{dx}, \tag{110}$$

when

- $f_X(x) \geq 0$,
- For the interval $[x_1, x_2]$, where $x_1, x_2 \in \Omega_p$,

  $$P_X = P(X \in [x_1, x_2]) = \int_{x_1}^{x_2} f_X(x)dx, \tag{111}$$

  such that the probability of a random variable $X \in [x_1, x_2]$ is defined by the integral of its probability density function evaluated in the referred interval.

- Probability of a random variable $X \in [-\infty, +\infty]$ is defined as

$$P_X = P(X \in [-\infty, +\infty]) = \int_{-\infty}^{+\infty} f_X(x)dx = 1 \tag{112}$$

The probability $P\{X \in \mathfrak{F}\}$ can be computed by the distribution P_X and one does not need to explicitly know the eventually complicated probability space $(\Omega_p, \mathfrak{F}, P)$ for such (BAUER; BURCKEL, 2011). Also, Bauer and Burckel (2011) define that several "probability-theoretic concepts" can be derived from their distributions.

One of such concepts is the expected value of a random variable X, $E[X]$. Thus, considering that the random variable $X \in (\Omega_p, \mathfrak{F}, P)$, the expected value of a random variable is defined by Bauer and Burckel (2011) as

$$E[X] := \int X dP_X. \tag{113}$$

One important property of the expected value is that

$$E[|X|] < +\infty, \tag{114}$$

which is equivalent to the integrability of the random variable X (BAUER; BURCKEL, 2011). The expected value can also be written considering the deterministic function of a random variable $\Phi(X)$, as

$$E[\Phi(X)] = \int_{-\infty}^{+\infty} \Phi(x) f_X(x)dx. \tag{115}$$

A general case of Eq. (115) is to consider $\Phi(X) = X^k$, with $k \geq 0$. If $k = 0$, then $E[X^0] = E[1] = 1$, which is the total probability of $X \in \Omega$. When $k > 0$, the k-th moment of $E[.]$ is defined, such that

$$m_k = E[X^k] = \int_{-\infty}^{+\infty} x^k f_X(x)dx, \tag{116}$$

where the expected value itself is the first moment of a random variable.

Another way of expressing the moments of X is to consider $E\left[(X - E[X])^k\right]$, defined as the central moment of X,

$$\bar{m}_k = E\left[(X - E[X])^k\right] = \int_{-\infty}^{+\infty} (x - E[X])^k f_X(x)dx. \tag{117}$$

The central moment, considering $k = 0$, leads to $E\left[(X - E[X])^0\right] = E[1] = 1$. Also, the first central moment, defined for $k = 1$, is $E\left[(X - E[X])^1\right] = E[X] - E[X] = 0$.

According to Bauer and Burckel (2011), the second central moment, $\bar{m}_2$, is of great importance and is called variance, represented by

$$Var[X] = E\left[(X - E[X])^2\right] = \int_{-\infty}^{+\infty} (x - E[X])^2 f_X(x)dx. \tag{118}$$

Another important definition, as defined by Bauer and Burckel (2011), is related to the standard deviation of X, defined as

$$Std[X] = \sqrt{Var[X]}. \tag{119}$$

Thus, the expected value is defined as measure of average whereas the variance and standard deviation define how scattered the random variables are around the average.

5.2 NORMAL PROBABILITY DENSITY FUNCTIONS

Normal probability density functions are often used in the uncertainty modeling in engineering problems, as is the case of this work. Thus, its main characteristics and properties are presented in this topic.

The Normal distribution function is a continuous differentiable function, with $X \in \mathbb{R}$, defined as

$$f_X(x) = \frac{1}{Std[X]\sqrt{2\pi}} \exp^{-\frac{1}{2}\left(\frac{x-E[X]}{Std[X]}\right)^2}. \tag{120}$$

One can verify that the distribution is totally defined by the expected value $E[X]$ and standard deviation $Std[X]$. Figure 2 depicts the regular shape of a Normal distribution, where the percentage values represent the quantity of the samples of X contained in each interval, defined as a function of $E[X]$ and $Std[X]$.

Figure 2 – Normal distribution

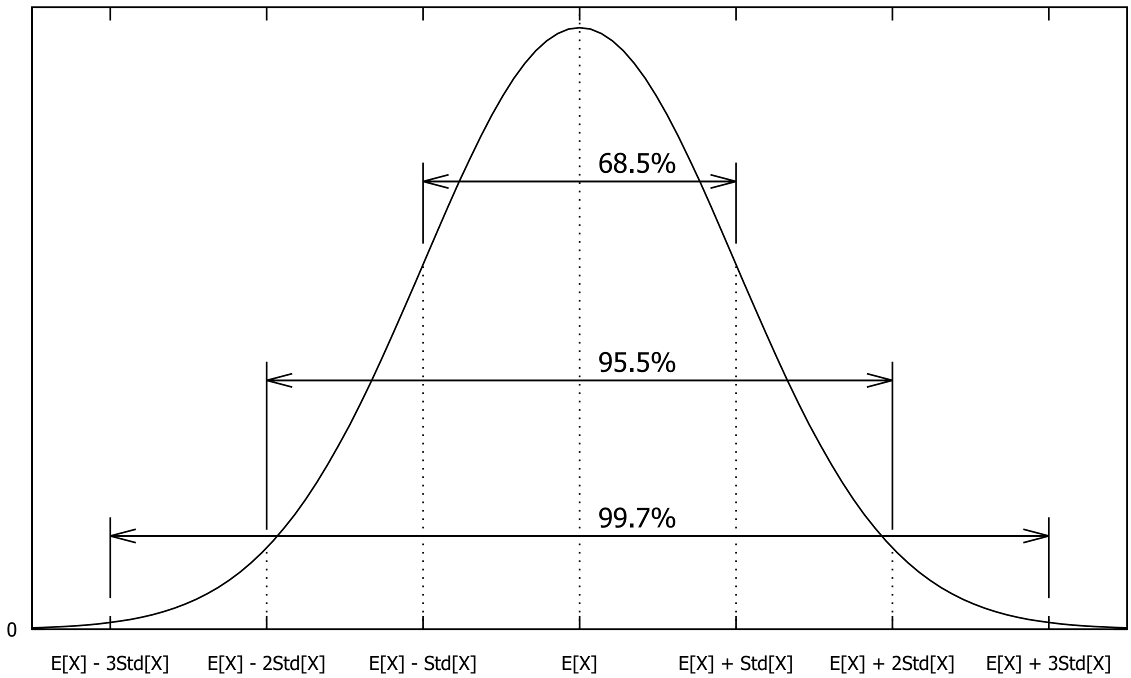

Source: Author production.

A regular Normal distribution, as the one shown in Fig. 2, can be defined as $X \sim \mathcal{N}\left(E[X], Std[X]\right)$.

The definition of a Normal distribution vector is given as

$$f_X(X) = \frac{1}{\sqrt{(2\pi)^N det\left(|\mathbf{S}|\right)}} \exp^{-\frac{1}{2}(x-E[X])^T\mathbf{S}^{-1}(x-E[X])}, \tag{121}$$

which depends on the expected value $E[X]$ and on the covariance matrix $\mathbf{S}$, defined as

$$\mathbf{S} = E\left[\left(X - E\left[X\right]\right)\left(X - E\left[X\right]\right)^T\right]. \tag{122}$$

It is important to highlight that variations of the regular Normal distribution are also common in engineering applications. One of such variations is the truncation of the distribution, such that instead of being defined in the interval $[-\infty, +\infty]$, it is defined according to a lower limit a and an upper limit b, such that the new interval is $[a, b]$. In this case, the distribution is defined as $X \sim \mathcal{N}\left(a, b, E[X], Std[X]\right)$.

A truncated Normal distribution is used in this work, as discussed in Section 8.

6 PROBABILISTIC ROBUST OPTIMIZATION

Components designed by considering the deterministic approach normally have high sensitivity to variations in input parameters such that uncertainties on material properties and in loading can highly affect the part's reliability in operation. Thus, a robust approach targets a solution for the optimization problem with reduced sensitivity, or improved robustness, with respect to changes in one or more input parameters (CARDOSO; SILVA; BECK, 2019; SILVA; CARDOSO, 2016; DA SILVA; BECK; CARDOSO, 2018).

In general, a robust optimization problem considers the minimization of the linear combination of the expected value $E[.]$ and the standard deviation $Std[.]$ of a function (response) with respect to a given (and uncertain) input data (CARDOSO; SILVA; BECK, 2019). The optimization problem can be defined as

$$\begin{aligned}
\underset{\boldsymbol{\rho}}{\text{minimize}} \quad & \Phi[\boldsymbol{\rho}, \mathbf{r}] = \psi E[f(\boldsymbol{\rho}, \mathbf{r})] + \varphi Std[f(\boldsymbol{\rho}, \mathbf{r})] \\
\text{subject to} \quad & g_j(\boldsymbol{\rho}) \leq \bar{g}_j \;\; j = 1..N_g, \\
& \boldsymbol{\rho}_l \leq \boldsymbol{\rho} \leq \boldsymbol{\rho}_u,
\end{aligned} \tag{123}$$

where $\mathbf{r} \in \mathbb{R}$ is a vector with the realizations of a given random variable X, $f(\boldsymbol{\rho}, \mathbf{r})$ is a generic function dependent on $\boldsymbol{\rho}$ and $\mathbf{r}$, constants ψ and φ are weighting factors for the expected value $E[.]$ and the standard deviation $Std[.]$, respectively. Thus, a large φ increases the importance of $Std[.]$ in the objective function, theoretically leading to a more robust solution.

There are several different approaches to compute $E[.]$ and $Std[.]$ and some of these methods are further described as follows:

- MCS method: According to Katzgraber (2009), Monte Carlo methods can be defined as a class of techniques for randomly sampling an N-dimensional space to estimate a probability distribution. Furthermore, the method is particularly useful for high-dimensional distributions given the fact that it can accurately capture their characteristics, being the challenge to correctly choose the random samples to minimize both the numerical effort and the inherent approximation errors (KATZGRABER, 2009). Problems aimed by the Monte Carlo method, as described by MacKay (1998), are to generate samples from a given distribution and to estimate expectations of functions under this distribution.

- Perturbation Method: consists in applying a small perturbation value on the chosen random variables and evaluating the expected value $E[.]$ and covariance $Cov[.]$, which has a direct relation with $Std[.]$, of the problem response. Considering, as an example, a classic elastic structural problem where the understanding of the impacts in the static displacements is desired, each term of the governing equation $\mathbf{KU} = \mathbf{F}$ can be written as second-order Taylor expansions around the mean value. Using such information from the Taylor expansions, one can compute $E[.]$ and $Cov[.]$ as defined in the work of Silva and Cardoso (2016). The caveat of this method is the limitation in the uncertainty level that can be considered (SILVA; CARDOSO, 2016).

- Unknown-but-bounded: allows for the design of components considering uncertain parameters with a defined variation interval, but not knowing how the probability distribution is. Using such information, the method is developed considering the solution of a double-loop problem. An inner loop is responsible for determining the worst case scenario and an outer loop is used to optimize the structure for the design case defined in the first loop. According to Zhang, Kang, and Zhang (2016), the double-loop problems solutions are generally time consuming and derivative of the outer loop tends to be relatively complex since there in no implicit dependency. Also according to Zhang, Kang, and Zhang (2016), many researchers studied possibilities of solving the problem with a single-loop problem, but, to date, the double-loop problem solution is still the more reasonable choice.

- Collocation Method: can be defined as a MCS method modified with the goal of increasing computational efficiency and is feasible, in comparison to the MCS method, up to a threshold of 50 random variables (LAZAROV, Boyan S; SCHEVENELS; SIGMUND, 2012). The method targets the calculation of $E[.]$ and $Std[.]$ by computing the deterministic problem at certain "collocation" points, which reduces the quantity of overall computation effort. The main challenge is to specify the collocation points such that the balance between computational cost and approximation accuracy is reached.

The MCS method is the baseline for accuracy verification of other methods and can be used regardless of the probability distribution of the input data. Therefore, the MCS method is used in this work, although the proposed optimization problem can also be used with any other method.

The expected value $E[.]$ can be written as the mean value of the evaluations of the function f with respect to the design variables $\boldsymbol{\rho}$ and realizations of the random variable, given in $\mathbf{r}$,

$$E[f(\boldsymbol{\rho},\mathbf{r})] = \frac{1}{N}\sum_{i=1}^{N} f(\boldsymbol{\rho}, r_i), \tag{124}$$

and Standard deviation of f, $Std[f(\boldsymbol{\rho},\mathbf{r})]$, can be evaluated in parallel with the expected value as

$$Std[f(\boldsymbol{\rho},\mathbf{r})] = \sqrt{\frac{1}{N-1}\left(\sum_{i=1}^{N}(f(\boldsymbol{\rho}, r_i)-\delta)^2 - \frac{(\sum_{i=1}^{N} f(\boldsymbol{\rho}, r_i)-\delta))^2}{N}\right)}. \tag{125}$$

where $\delta = f(\boldsymbol{\rho}, E[\mathbf{r}])$ is an offset used to address numerical cancellation errors (CARDOSO; SILVA; BECK, 2019).

Generally, a large number of samples is needed to be taken from the distribution to increase the accuracy of the method. Inevitably, the evaluation of very similar samples happens many times along the process, creating results that could be interpreted as "repetitions" or clusters of previously computed results.

To overcome this undesired behavior, the general robust problem formulation defined in Cardoso, Silva, and Beck (2019) is modified in this work. Such modification is a particular variation of the Stratified Sampling method, described by Shields et al. (2015), and consists in discretizing, in N_{bins} parts, the histogram generated by a highly populated realizations vector, with N events, following the distribution of interest. For each bin, the number of events, N_{e_i}, and the simple average of the samples $\bar{r}_i$ are computed, as depicted in Fig. 3.

As an outcome, both the expected value and the standard deviation of f are evaluated using the average of the samples in each interval and the associated number of

Figure 3 – Stratified sampling.

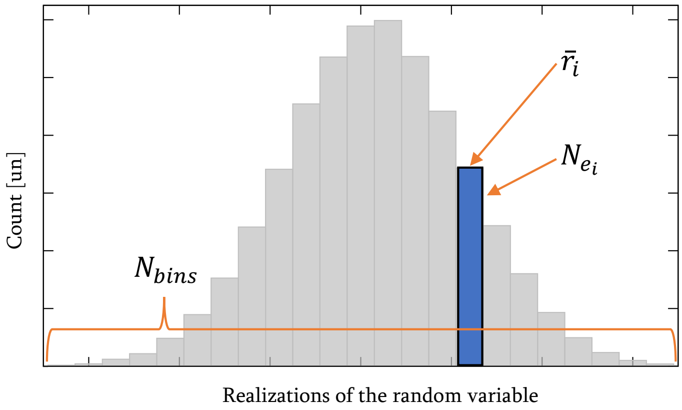

Source: Author production.

samples. Thus, the expected value $E[.]$ is redefined as

$$E[f(\boldsymbol{\rho}, \mathbf{r})] = \frac{1}{N} \sum_{i=1}^{N_{bins}} f(\boldsymbol{\rho}, \bar{r}_i) N_{e_i}, \tag{126}$$

where $f(\boldsymbol{\rho}, \bar{r}_i)$ is evaluated considering the design variables $\boldsymbol{\rho}$ and the average value of the samples of $\mathbf{r}$ inside bin i.

Standard deviation of f, $Std[f(\boldsymbol{\rho}, \mathbf{r})]$, is also redefined accordingly, such that

$$Std[f(\boldsymbol{\rho}, \mathbf{r})] = \sqrt{\frac{1}{N-1} \left(\sum_{i=1}^{N_{bins}} \left(f(\boldsymbol{\rho}, \bar{r}_i) - \delta\right)^2 N_{e_i} - \frac{\left[\sum_{i=1}^{N_{bins}} \left(f(\boldsymbol{\rho}, \bar{r}_i) - \delta\right) N_{e_i}\right]^2}{N} \right)}. \tag{127}$$

The presented formulation allows data sourcing from a highly populated vector of realizations of the random variable while ensuring relatively low computational cost, since it is proportional to the choice of the parameter N_{bins} and not to the number of realizations N, considering $N \gg N_{bins}$. Additionally, it is important to mention that this approach does not account for any refinement of the number of bins based on some error measure of the outcomes of the MCS. Thus, numerical experiments are needed to choose N_{bins} in advance for a particular problem.

Equations (126) and (127) are evaluated using parallel processing in the computer implementation used in this work. This is a straightforward task due to the embarrassingly parallel nature of the Monte Carlo Method and also by the capabilities provided by a modern programming language like Julia, where a loop can be easily spawned to multiple processes (BEZANSON et al., 2017).

6.1 SENSITIVITY ANALYSIS OF A PROBABILISTIC ROBUST PROBLEM

The sensitivity of function Φ defined in Eq. (123) w.r.t. a design variable ρ_m is

$$\frac{d\Phi(\boldsymbol{\rho}, \mathbf{r})}{d\rho_m} = \psi \frac{dE[f(\boldsymbol{\rho}, \mathbf{r})]}{d\rho_m} + \varphi \frac{dStd[f(\boldsymbol{\rho}, \mathbf{r})]}{d\rho_m}. \tag{128}$$

Dealing with the two parts at the right side of equation separately, one has

$$\frac{dE[f(\boldsymbol{\rho},\mathbf{r})]}{d\rho_m}=\frac{1}{N}\sum_{i=1}^{N}\frac{df(\boldsymbol{\rho},r_i)}{d\rho_m}. \tag{129}$$

Continuing with the second part of the equation (128), it is given that

$$\frac{dStd[f(\boldsymbol{\rho},\mathbf{r})]}{d\rho_m}=\frac{d}{d\rho_m}\Big[\frac{1}{N-1}\Big(\sum_{i=1}^{N}(f(\boldsymbol{\rho},r_i)-\delta)^2-\frac{(\sum_{i=1}^{N}f(\boldsymbol{\rho},r_i)-\delta))^2}{N}\Big)\Big]^{\frac{1}{2}}. \tag{130}$$

Further developing the derivative, results in

$$\begin{aligned}\frac{dStd[f(\boldsymbol{\rho},\mathbf{r})]}{d\rho_m}&=\frac{1}{2}\Big[\Big(\sum_{i=1}^{N}(f(\boldsymbol{\rho},r_i)-\delta)^2-\frac{(\sum_{i=1}^{N}f(\boldsymbol{\rho},r_i)-\delta))^2}{N}\Big)\Big]^{-\frac{1}{2}}\\ \frac{1}{N-1}&\left[\sum_{i=1}^{N}2(f(\boldsymbol{\rho},r_i)-\delta)\frac{df(\boldsymbol{\rho},r_i)}{d\rho_m}-\frac{\sum_{i=1}^{N}2(f(\boldsymbol{\rho},r_i)-\delta)\sum_{i=1}^{N}\frac{df(\boldsymbol{\rho},r_i)}{d\rho_m}}{N}\right].\end{aligned} \tag{131}$$

Simplifying the notation and reorganizing terms, the final derivative for $Std[f(\boldsymbol{\rho},\mathbf{r})]$ is defined as

$$\begin{aligned}\frac{dStd[f(\boldsymbol{\rho},\mathbf{r})]}{d\rho_m}=\frac{1}{2}\frac{1}{Std[f(\boldsymbol{\rho},\mathbf{r})]}\frac{1}{N-1}&\left[\sum_{i=1}^{N}2(f(\boldsymbol{\rho},r_i)-\delta)\frac{df(\boldsymbol{\rho},r_i)}{d\rho_m}\right.\\ &\left.-\frac{\sum_{i=1}^{N}2(f(\boldsymbol{\rho},r_i)-\delta)\sum_{i=1}^{N}\frac{df(\boldsymbol{\rho},r_i)}{d\rho_m}}{N}\right].\end{aligned} \tag{132}$$

Analogously, the sensitivity for the modified robust problem formulation, defined in Eqs. (126) and (127), is given as

$$\frac{dE[f(\boldsymbol{\rho},\mathbf{r})]}{d\rho_m}=\frac{1}{N}\sum_{i=1}^{N_{bins}}\frac{df(\boldsymbol{\rho},\overline{r_i})}{d\rho_m}N_{e_i} \tag{133}$$

and

$$\begin{aligned}\frac{dStd[f(\boldsymbol{\rho},\mathbf{r})]}{d\rho_m}=\frac{1}{2}\frac{1}{Std[f(\boldsymbol{\rho},\mathbf{r})]}\frac{1}{N-1}&\left[\sum_{i=1}^{N_{bins}}2(f(\boldsymbol{\rho},\bar{r}_i)-\delta)N_{e_i}\frac{df(\boldsymbol{\rho},\bar{r}_i)}{d\rho_m}\right.\\ &\left.-\frac{\sum_{i=1}^{N_{bins}}2(f(\boldsymbol{\rho},\bar{r}_i)-\delta)N_{e_i}\sum_{i=1}^{N_{bins}}\frac{df(\boldsymbol{\rho},\bar{r}_i)}{d\rho_m}N_{e_i}}{N}\right].\end{aligned} \tag{134}$$

Thus, for each sample $\bar{r}_i$, it is necessary to evaluate the sensitivity $\frac{df(\boldsymbol{\rho},\bar{r}_i)}{d\rho_m}$. Equations (133) and (134) are evaluated using parallel processing in the computer implementation used in this work, since the computation of sensitivities for each $\bar{r}_i$ can be carried out independently.

7 PROPOSED FORMULATION

The proposed formulation aims the design of continuum structures with optimized dynamic response and improved behavior robustness with respect to uncertainties in the excitation frequency ω, considering volume constraint.

By optimized dynamic displacements with improved robustness, the author means resonant and non-resonant structures with minimized variation in the dynamic response around a given target frequency. Thus, in case of non-resonant structures are targeted, the dynamic displacements shall be relatively small (without the presence of high-energy resonances close to the target frequency) and consistently similar around the target frequency. When resonant structures are targeted, the objective is to create designs with high dynamic displacements and also with low variation in the dynamic response around a target excitation frequency.

The objective function is defined as a linear combination of two terms: the robust design formulation presented in Section 6 and the static compliance. The problem is defined as

$$\begin{aligned} \underset{\boldsymbol{\rho}}{\text{minimize}} \quad & \Phi(\boldsymbol{\rho},\boldsymbol{\omega}) = R(\boldsymbol{\rho},\boldsymbol{\omega}) + \gamma_2 \frac{\Upsilon_S(\boldsymbol{\rho})}{\Upsilon_S^0} \\ \text{subject to} \quad & \mathbf{K}_D(\boldsymbol{\rho},\boldsymbol{\omega})\,\mathbf{U}(\boldsymbol{\rho},\boldsymbol{\omega}) = \mathbf{F}, \\ & \mathbf{K}(\boldsymbol{\rho})\,\mathbf{U}_S(\boldsymbol{\rho}) = \mathbf{F}, \\ & V(\boldsymbol{\rho}) = \sum_{e=1}^{ne} \rho_e V_e^0 \leq \bar{V}, \\ & \boldsymbol{\rho}_l \leq \boldsymbol{\rho} \leq \boldsymbol{\rho}_u, \end{aligned} \tag{135}$$

with

$$R(\boldsymbol{\rho},\boldsymbol{\omega}) = \frac{\gamma_1 E[N_{mwdB}(\boldsymbol{\rho},\boldsymbol{\omega})] + |\gamma_1| \varphi Std[N_{mwdB}(\boldsymbol{\rho},\boldsymbol{\omega})]}{E[N_{mwdB}(\boldsymbol{\rho},\boldsymbol{\omega})]^0 + \varphi Std[N_{mwdB}(\boldsymbol{\rho},\boldsymbol{\omega})]^0}, \tag{136}$$

where $E[N_{mwdB}(\boldsymbol{\rho},\boldsymbol{\omega})]$ and $Std[N_{mwdB}(\boldsymbol{\rho},\boldsymbol{\omega})]$ are the expected value and standard deviation of the density-weighted norm N_{mwdB} as a function of the vector of design variables $\boldsymbol{\rho}$. The vector $\boldsymbol{\omega}$ contains N realizations of the random variable $X(\omega)$, which is the excitation frequency, such that each ω contained in $\boldsymbol{\omega}$ is used in the MCS process. The weighting factor φ is used to set the relative importance of the expected value and the standard deviation (ψ from Eq. (123) is assumed as 1.0).

Weight constants γ_1 and γ_2 are defined in the same way as presented in Section 4.5. The caveat is that γ_1 multiplies both the expected value and the standard deviation in Eq. (136) however, its module is adopted together with $Std[.]$ to ensure that the standard deviation is always minimized independently of the signal of γ_1.

Both equilibrium equations are identically satisfied during the finite element computations, such that the only functional constraint is the (deterministic) volume $V(\boldsymbol{\rho}) = \sum \rho_e V_e^0 \leq \bar{V}$.

Optimization problem defined in Eq. (135) can be solved by using many traditional methods, like the Method of Moving Asymptotes (SVANBERG, 1987), for example. However, the Augmented Lagrangian (AL) method, presented in Section 3.3, is used in this work. Thus, the constrained optimization problem defined in Eq. (135) is rewritten as a sequence of unconstrained optimization problems as

$$\begin{aligned} \underset{\boldsymbol{\rho}}{\text{minimize}} \quad & \mathcal{L}^q(\boldsymbol{\rho}, \boldsymbol{\mu}^q, r_p^q, \boldsymbol{\omega}) = \Phi(\boldsymbol{\rho}, \boldsymbol{\omega}) + \frac{{r_p}^q}{2} \left\langle \frac{\mu_1^q}{{r_p}^q} + \frac{V(\boldsymbol{\rho})}{\bar{V}} - 1 \right\rangle^2 \\ \text{subject to} \quad & \boldsymbol{\rho}_l \leq \boldsymbol{\rho} \leq \boldsymbol{\rho}_u, \end{aligned} \tag{137}$$

where q is the AL iteration, μ_1^q is the Lagrange multiplier associated to the volume constraint, ${r_p}^q$ is a penalty factor and $\langle a \rangle = \max(a, 0)$. The same procedure used in Montero, Silva, and Cardoso (2020) is used here, with the only difference being the robust part of the objective function $\Phi(\boldsymbol{\rho}, \boldsymbol{\omega})$.

The sensitivity of $\mathcal{L}^q$ with respect to a design variable ρ_m is

$$\frac{d\mathcal{L}^q(\boldsymbol{\rho}, \boldsymbol{\mu}^q, r_p^q, \boldsymbol{\omega})}{d\rho_m} = \frac{d\Phi(\boldsymbol{\rho}, \boldsymbol{\omega})}{d\rho_m} + {r_p}^q \left\langle \frac{\mu_1^q}{{r_p}^q} + \frac{V(\boldsymbol{\rho})}{\bar{V}} - 1 \right\rangle \frac{1}{\bar{V}} \frac{dV(\boldsymbol{\rho})}{d\rho_m}, \tag{138}$$

where

$$\frac{d\Phi(\boldsymbol{\rho}, \boldsymbol{\omega})}{d\rho_m} = T \left(\gamma_1 \frac{dE[N_{mwdB}(\boldsymbol{\rho}, \boldsymbol{\omega})]}{d\rho_m} + |\gamma_1| \varphi \frac{dStd[N_{mwdB}(\boldsymbol{\rho}, \boldsymbol{\omega})]}{d\rho_m} \right) + \frac{\gamma_2}{\Upsilon_S^0} \frac{d\Upsilon_S(\boldsymbol{\rho})}{d\rho_m} \tag{139}$$

and

$$T = \frac{1}{E[N_{mwdB}(\boldsymbol{\rho}, \boldsymbol{\omega})]^0 + \varphi Std[N_{mwdB}(\boldsymbol{\rho}, \boldsymbol{\omega})]^0}. \tag{140}$$

Derivatives $\frac{dE[N_{mwdB}(\boldsymbol{\rho}, \boldsymbol{\omega})]}{d\rho_m}$ and $\frac{dStd[N_{mwdB}(\boldsymbol{\rho}, \boldsymbol{\omega})]}{d\rho_m}$ are evaluated using Eqs. (133) and (134) and the derivative of $N_{m\omega dB}$ with respect to ρ_m is presented in Section 4.5.1. The Central Finite Difference method was used for validating the computational implementation of the derivative, considering different perturbation levels for numerical convergence assurance.

Regarding the solution procedure, the realizations of the excitation frequency are generated in the very beginning of the process and the exact same realizations are considered in all the iterations. This strategy is commonly referred in the literature as the Common Random Numbers method. Figure 4 shows the flowchart of the optimization procedure using the Augmented Lagrangian approach.

Figure 4 – Optimization algorithm flowchart.

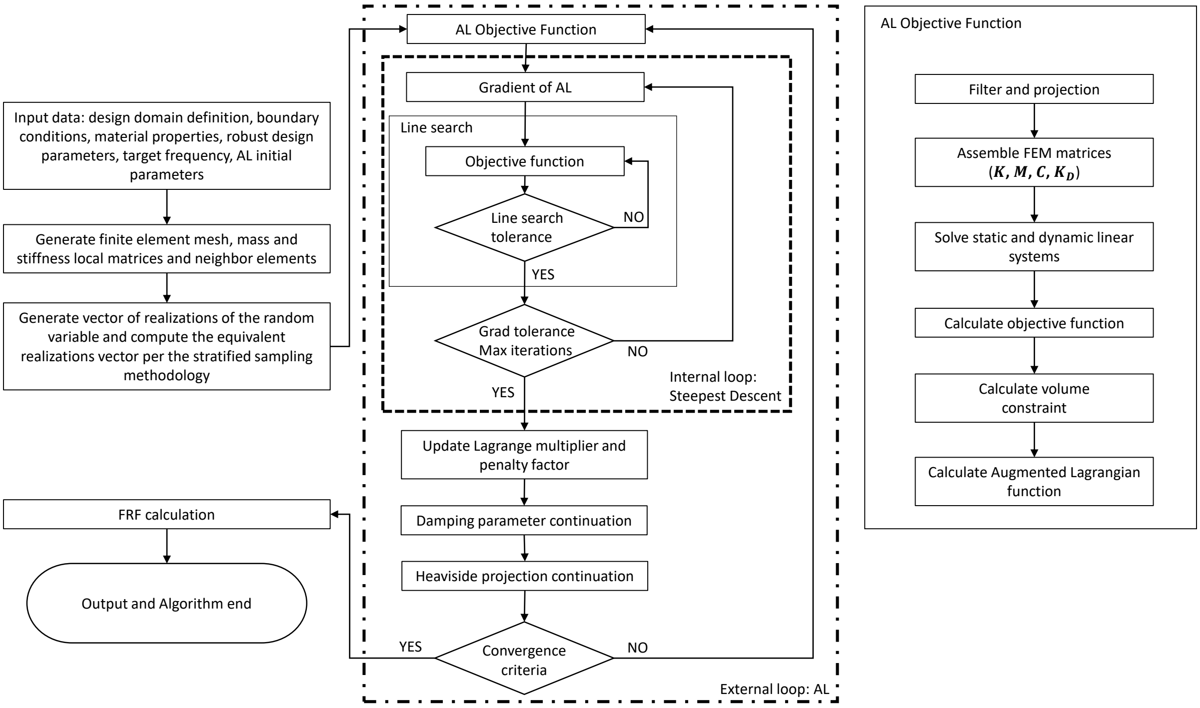

Source: Author production.

8 RESULTS

This section presents the outcomes from the various cases in which the proposed formulation has been tested. Results for non-resonant and resonant structures are demonstrated in Sections 8.2 and 8.3, respectively.

Four-node incompatible bilinear isoparametric elements are used in the finite element discretization to better represent bending behavior, specially in slender reinforcements (PIAN; WU, 2005), which is discussed in details in Section 2.2.1. The linear spatial filter and the Heaviside projection are used to ensure minimum length scale, avoid mesh dependency, checkerboard patterns and to obtain crispy black and white topologies (SIGMUND, 2007; WANG; LAZAROV; SIGMUND, 2011). Additionally, damping modeling and the related continuation strategy are described in Section 4.3.

Regarding the robust problem modeling, the use of the MCS method makes it possible to consider different distributions for ω. Nonetheless, a truncated normal distribution is used in this work. The truncation is justified by the fact that a normal distribution can, theoretically, result in negative realizations or even unrealistic high frequencies. These two scenarios would have no physical meaning for the context of this work since: 1) the frequency is a positive measure, and 2) an unrealistic high frequency would be too far from the frequency of interest.

The truncation is defined as an interval $\pm\Delta\omega$ around the mean $\bar{\omega}$, such that at least 99.7% of the realizations of the non-truncated distribution with the same mean and standard deviations is represented by the truncated distribution. Thus, the frequency ω is modeled as

$$\omega \sim \mathcal{N}\left(\omega_l, \omega_u, \bar{\omega}, \eta\right), \tag{141}$$

where ω_l and ω_u are the lower and upper bounds of ω, $\bar{\omega}$ is the mean value and η the standard deviation. The limits are defined as

$$\omega_{u,l} = \bar{\omega} \pm \frac{\Delta\omega}{2\pi}, \tag{142}$$

where $\bar{\omega}$, η and $\Delta\omega$ are defined for each one of the cases studied in this section.

Reference vector $\boldsymbol{\omega}_{\bar{\omega},\eta}$ is obtained with $N = 1 \times 10^6$ realizations of Eq. (141) for each combination of $\bar{\omega}$, η and $\Delta\omega$ studied in this section. This vector is used as input to the pre-processing discussed in Section 6, used in the optimization procedure. The number of bins used in the pre-processing was found after a careful evaluation of the errors for the expected value, standard deviation and the Inf norm of gradient for the worst case (larger η and small φ), i.e., with large output standard deviation of $N_{m\omega dB}$. Table 1 shows the relative differences obtained when using a regular MCS with low number of realizations and for the modified approach, for different values of N_{bins}. The reference is the regular MCS with $N = 1 \times 10^6$ realizations. Based on these results, $N_{bins} = 30$ is used to perform all the optimizations in this section.

8.1 DESIGN MODELS

Two different design models were evaluated in this work with the objective to check the formulation behavior under different conditions. Thus, in Sections 8.1.1 and 8.1.2, they are defined and their main characteristics are described.

Table 1 – Relative differences for expected value, standard deviation and Inf norm of sensitivities with respect to the reference MCS with 1×10^6 realizations.

Case	E	Std	Gradient
Regular MCS, $N = 250$	0,001%	0,278%	0,347%
Modified MCS, $N_{bins} = 5$	0,000%	4,358%	0,051%
Modified MCS, $N_{bins} = 10$	0,000%	1,159%	0,013%
Modified MCS, $N_{bins} = 30$	0,000%	0,130%	0,002%
Modified MCS, $N_{bins} = 50$	0,000%	0,046%	0,001%
Modified MCS, $N_{bins} = 75$	0,000%	0,046%	0,001%
Modified MCS, $N_{bins} = 100$	0,000%	0,000%	0,000%
Modified MCS, $N_{bins} = 150$	0,000%	0,000%	0,000%
Modified MCS, $N_{bins} = 250$	0,000%	0,000%	0,000%

Source: Author production.

8.1.1 Cantilever beam with central loading

The first test case is related to structures with symmetry in geometry, load and boundary conditions, as shown in Fig. 5. The load is homogeneously applied along edge c and the relative densities of all elements on this region are kept constant and equal to 1.0 during the optimization.

Figure 5 – Definition of Problem 1.

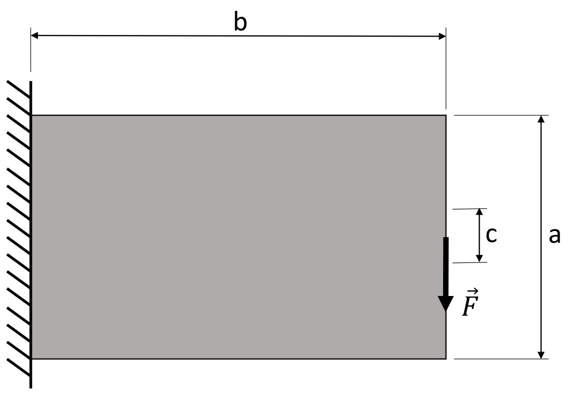

Source: Author production.

Relevant data used in this test case are presented in Tab. 2.

Also, following the work of (MONTERO; SILVA; CARDOSO, 2020), mean frequencies of $\bar{\omega} = 365$, $\bar{\omega} = 700$, $\bar{\omega} = 1135$ and $\bar{\omega} = 1440$ Hz are studied in the next subsections.

8.1.2 Cantilever beam with bottom loading

A second test case is used to assess if the proposed formulation can increase robustness without exploring the symmetry of the geometry, loading and boundary conditions. Thus, the load application point is changed to an asymmetric location, as shown in Fig. 6 and the height of the domain is slightly increased to change the initial

Table 2 – Problem data - Test case 1.

Data	Value	Unit
Height a	0.5	$[m]$
Length b	1.0	$[m]$
Edge length c	0.1	$[m]$
Thickness	1.0	$[m]$
Young Modulus	210	$[GPa]$
Poisson	0.3	$[-]$
Mass density	7860	$[kg/m^3]$
Harmonic Load	10000	$[N]$

Source: Author production.

frequency response. The load is again applied along edge c and the relative densities of all elements on this region are also kept constant and equal to 1.0 during the optimization.

Figure 6 – Definition of Problem 2

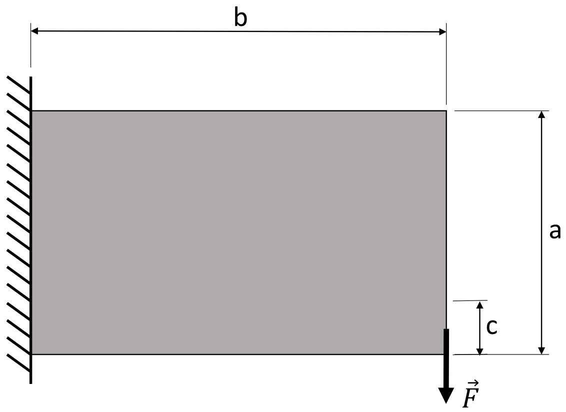

Source: Author production.

Relevant data for this test case are presented in Tab. 3.

Table 3 – Problem data - Test case 2.

Data	Value	Unit
Height a	0.625	$[m]$
Length b	1.0	$[m]$
Edge length c	0.1	$[m]$
Thickness	1.0	$[m]$
Young Modulus	210	$[GPa]$
Poisson	0.3	$[-]$
Mass density	7860	$[kg/m^3]$
Harmonic Load	10000	$[N]$

Source: Author production.

To define the target frequencies for this case, the dynamic response of the structure is evaluated using the dynamic compliance, such that resonances and antiresonances can be identified. The design domain is configured with $\bar{V} = 100\%$ and the resultant frequency response is shown in Fig. 7.

Figure 7 – Frequency response of the Problem 2.

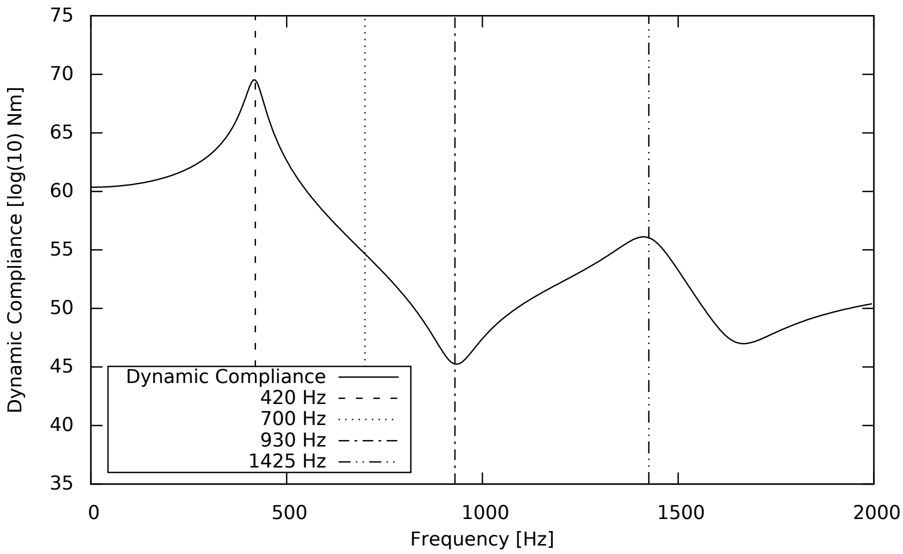

Source: Author production.

Based on the frequency response, the target frequencies $\bar{\omega}$ are the first resonance (420 Hz), an intermediate frequency between the first resonance and one antiresonance (700 Hz), an antiresonance (930 Hz) and the second resonance (1425 Hz). It is important to highlight that the selected frequencies are the closest multipliers of 5 Hz of the actual resonances and antiresonances.

8.2 DYNAMIC RESPONSE MINIMIZATION

Two distinct design situations, demonstrated in Sections 8.2.1 and 8.2.3, are investigated with the objective of evaluating the proposed formulation.

For all cases, the parameters γ_1 and $\bar{V}$ from Eq. (137) are defined as 0.99 and $0.5|\Omega|$, respectively, where $|\Omega|$ is the volume of the design domain. Also, the same initial design point is used in all optimizations, which is selected to violate the volume constraint in 10%, such that the penalty parameter r_p, from Eq. (137), can be automatically computed with Eq. 67. Thus, results presented as "Before Optimization" in this section are obtained with an homogeneous material distribution given by $\rho_i = 0.5 * 1.1$, $\forall i$, that is, considering the starting point.

Finally, exponents from the density-weighted norm, presented in Eqs. 86 and 87, are defined as $m = 2.0$ and $w = 2.0$ (MONTERO; SILVA; CARDOSO, 2020). It is worth stressing that the smaller is the γ_2, the smaller is the contribution from the static compliance. Thus, as $\gamma_2 = |\gamma_1| - 1 = 0.01$, the results obtained in this work are mainly influenced by the dynamic norm, as desired.

The problem is solved with $N_{AL} = 15$ external loops where the first $N_\zeta = 10$ iterations are used to effectively solve the problem and to apply the continuation procedure for ζ, Eq. (81). The last 5 AL iterations are used to reduce the occurrence of intermediate

Figure 8 – Topologies obtained with the deterministic approach, Eq. (85), for the test case depicted in Fig. 5.

365.0 Hz	700.0 Hz	1135.0 Hz	1440.0 Hz

Source: Author production.

relative density values, so that the initial value of the Heaviside projection parameter $\beta_H = 1.5$ is updated along the optimization process as

$$\beta_H^{k+1} = \begin{cases} 1.5, & \text{if } 1 \leq k \leq N_\zeta \\ \beta_H^k + 7.5, & \text{if } N_\zeta < k \leq N_{AL}. \end{cases} \tag{143}$$

Three basic parameters are used to assess the formulation. The first one is φ, defined in Eq. (136), responsible for weighting the importance of the standard deviation in the objective function. The second parameter is the expected value of the excitation frequency, $\bar{\omega}$, and the third one is its standard deviation η and the associated $\Delta\omega$. Optimized topologies, evaluation of robustness [1], analysis of the frequency response and an investigation about the mechanisms used by the optimizer to impose the robustness are discussed in all examples.

8.2.1 Cantilever beam with central loading

The first test case is related to structures with symmetry in geometry, load and boundary conditions, as defined in Section 8.2.1, considering a mesh of 72×36, giving a total of 2592 elements, and spatial filter radius $R = 0.031$ m. In such configuration, vibration modes presenting low contribution to the global response can be weakly activated due to possible asymmetries in the design or due to a load vector $\mathbf{F}$ quasi-orthogonal to $\mathbf{U}$. Consequently, low-energy resonances can appear close to the frequency of interest and this mechanism can be used to increase the robustness of the design.

For reference and further comparison to the robust designs, the topologies obtained using the deterministic approach for each investigated frequency are shown in Fig. 8.

For each central frequency $\bar{\omega}$ defined in Section 8.1.1, deviations of $\eta = 2.0$, $\eta = 5.0$ and $\eta = 10$ Hz are studied, with corresponding values of $\Delta\omega$ of 20, 20 and 30 Hz, respectively, to account for at least 99.7% of the original frequency (not truncated) content.

8.2.1.1 Results at 365 Hz

The first investigation is performed at the target frequency of 365 Hz, which presents a dynamic behavior with high dependency on the stiffness (OLHOFF, N.; DU, J., 2009). Resulting topologies obtained with different values of η and φ, are depicted in Fig. 9.

[1] The histograms computed for the robustness evaluations and depicted in the following subsections refer to the absolute number of realizations, and not to the relative number of realizations. Same strategy is used in the maximization cases, described in Section 8.3.

Figure 9 – Topologies obtained at 365 Hz, for different values of η and φ.

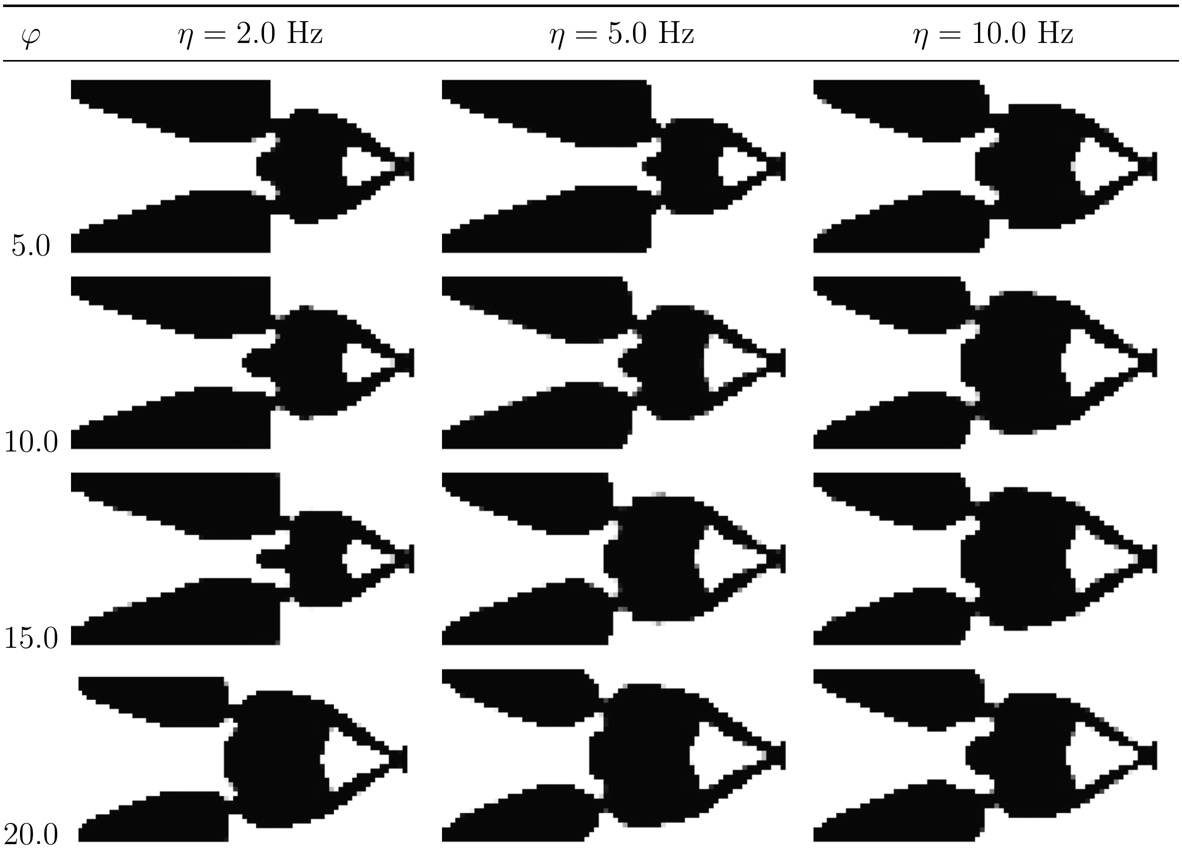

Source: Author production.

Table 4 – Expected values $E[N_{m\omega dB}]$ at 365 Hz, for different values of η and φ.

φ	$\eta = 2.0$ Hz	$\eta = 5.0$ Hz	$\eta = 10.0$ Hz
0.0	67.7007	67.7028	67.7099
5.0	67.5667	67.4196	67.8839
10.0	67.6042	67.8453	68.1752
15.0	67.5534	68.0176	68.2413
20.0	68.0189	68.2350	67.9966

Source: Author production.

Table 5 – Standard deviations $Std[N_{m\omega dB}]$ at 365 Hz, for different values of η and φ.

φ	$\eta = 2.0$ Hz	$\eta = 5.0$ Hz	$\eta = 10.0$ Hz
0.0	0.0303	0.0758	0.1505
5.0	0.0216	0.0258	0.0396
10.0	0.0110	0.0034	0.0123
15.0	0.0051	0.0035	0.0121
20.0	0.0082	0.0034	0.0099

Source: Author production.

The topology is the same for all cases, with good connectivity and with very small presence of intermediate densities. The difference observed in the designs is in the shape and size of the main features. The robustness of the resulting topologies are assessed by evaluating $N_{m\omega dB}\left(\boldsymbol{\rho}^{\star}, \boldsymbol{\omega}_{\bar{\omega},\eta}\right)$, where $\boldsymbol{\rho}^{\star}$ corresponds to the relative densities of each one of the designs shown in Fig. 9 and $\boldsymbol{\omega}_{\bar{\omega},\eta}$ is the reference vector with the realizations of the random variable $X(\omega)$ ($N = 1 \times 10^6$) with the associated η and $\Delta\omega$ values. The resulting histograms are shown in Fig. 10 and the corresponding expected values and standard deviations are shown in Tables 4 and 5. First lines of these two tables, relative to $\varphi = 0.0$, present the expected values and standard deviations of the deterministic design when subjected to $\boldsymbol{\omega}_{\bar{\omega},\eta}$. The same strategy is used for all subsequent test cases and frequencies of interest.

As expected, while designs with low values of φ or η tend to the deterministic dynamic behavior, designs obtained with higher values of these same parameters lead to important improvements in the robustness. Also, the expected value increases while the standard deviation decreases. Increasing parameters η and φ, in general, lead to increased robustness designs.

The design obtained with $\varphi = 15$ and $\eta = 10$ Hz is selected for further evaluation. Its frequency response is presented in the left side of Fig. 11. It can be seen that the optimization process relocated the first two resonances so that the frequency plot of the displacement norm is quasi-flat exactly at the target frequency (b). In relatively low frequencies, the optimization process can lead to an adequate separation between the adjacent resonances, which makes this type of result possible. This is an extremely efficient dynamic solution to the purposes of this work. Frequency plots for both the initial design and deterministic approach are also presented, where it is easy to notice the large difference with respect to the robust solution.

The absolute value $|\mathbf{U}(\omega)|$ of the displacement fields at the first two resonances

Figure 10 – Histograms of $N_{m\omega dB}$ comparing the robust and deterministic designs at 365 Hz, for different values of η and φ. Histograms in green are relative to deterministic designs and the histograms in grey are relative to robust designs.

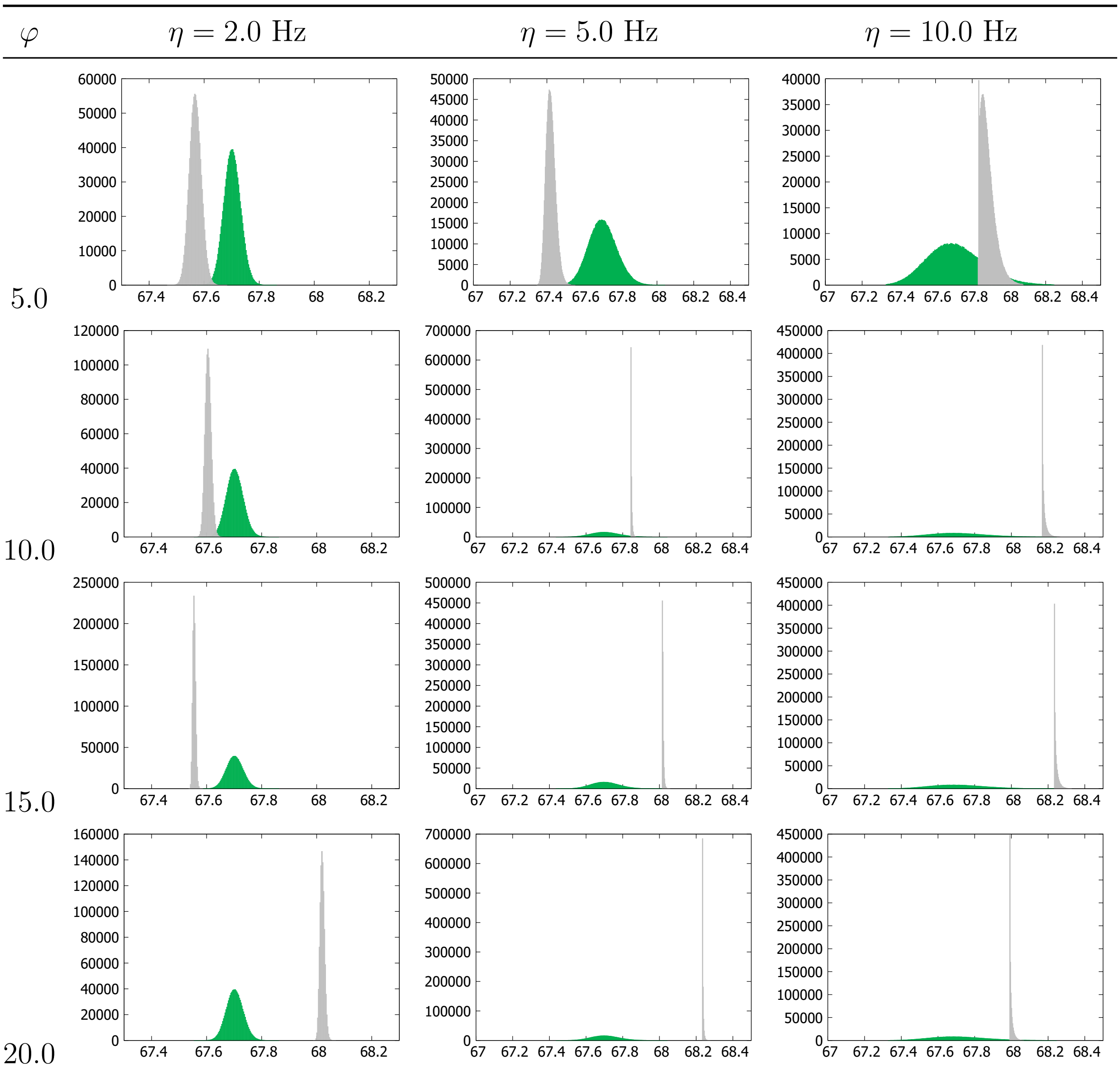

Source: Author production.

Figure 11 – Frequency response for the robust design ($\eta = 10$ Hz and $\varphi = 15.0$) and for the deterministic design (left) and topology with dynamic displacement fields (absolute values) at three different frequencies for the same robust design (right), obtained at 365 Hz.

Frequency Response	Displacement Field

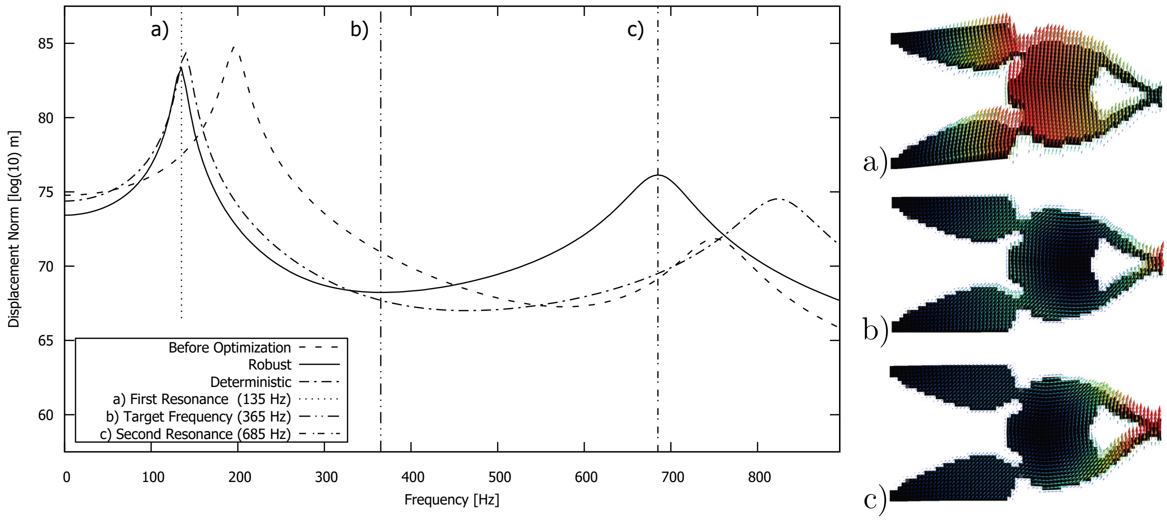

Source: Author production.

Table 6 – Expected values $E[N_{m\omega dB}]$ at 700 Hz, for different values of φ and η.

φ	$\eta = 2.0$ Hz	$\eta = 5.0$ Hz	$\eta = 10.0$ Hz
0.0	63.5415	63.5417	63.5429
5.0	63.5705	63.5160	63.7672
10.0	63.5443	63.7877	63.8879
15.0	63.5432	63.8691	64.0785
20.0	63.7988	63.8671	64.1072

Source: Author production.

and at the excitation frequency are also illustrated in Fig. 11, where it is clear the smaller magnitudes in displacement at 365 Hz when compared to the adjacent resonance frequencies.

8.2.1.2 Results at 700 Hz

Figure 12 shows the topologies obtained for a target frequency of 700 Hz. Resulting topologies show a tendency for mass accumulation close to the loading edge, with slender cross-shaped reinforcements. At some specific cases, the mesh discretization used was insufficient to properly allow for their formation and hinges started to appear. Nonetheless, the dynamic response of the structures around and at the target frequency of 700 Hz does not rely in such hinges and, therefore, the topologies are considered acceptable for the intentions of this work.

Histograms of $N_{m\omega dB}$ for the results are shown in Fig. 13 and the associated expected values and standard deviations are shown in Tables 6 and 7.

An interesting aspect of the resultant topologies is that an abrupt change in the

Figure 12 – Topologies obtained at 700 Hz, for different values of η and φ.

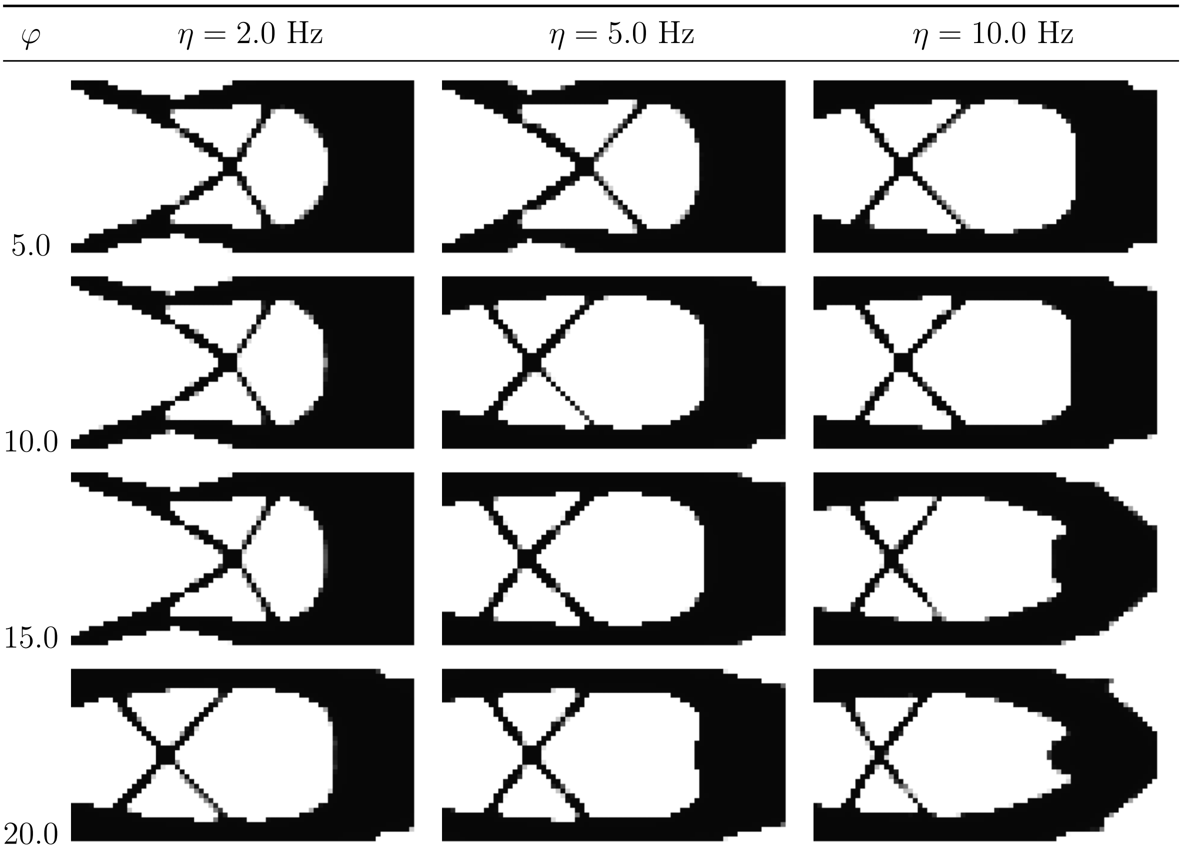

Source: Author production.

Table 7 – Standard deviations $Std[N_{m\omega dB}]$ at 700 Hz, for different values of φ and η.

φ	$\eta = 2.0$ Hz	$\eta = 5.0$ Hz	$\eta = 10.0$ Hz
0.0	0.0260	0.0651	0.1286
5.0	0.0263	0.0613	0.0263
10.0	0.0258	0.0080	0.0116
15.0	0.0256	0.0044	0.0086
20.0	0.0033	0.0057	0.0163

Source: Author production.

Figure 13 – Histograms of $N_{m\omega dB}$ comparing the robust and deterministic designs at 700 Hz, for different values of η and φ. Histograms in green are relative to deterministic designs and the histograms in grey are relative to robust designs.

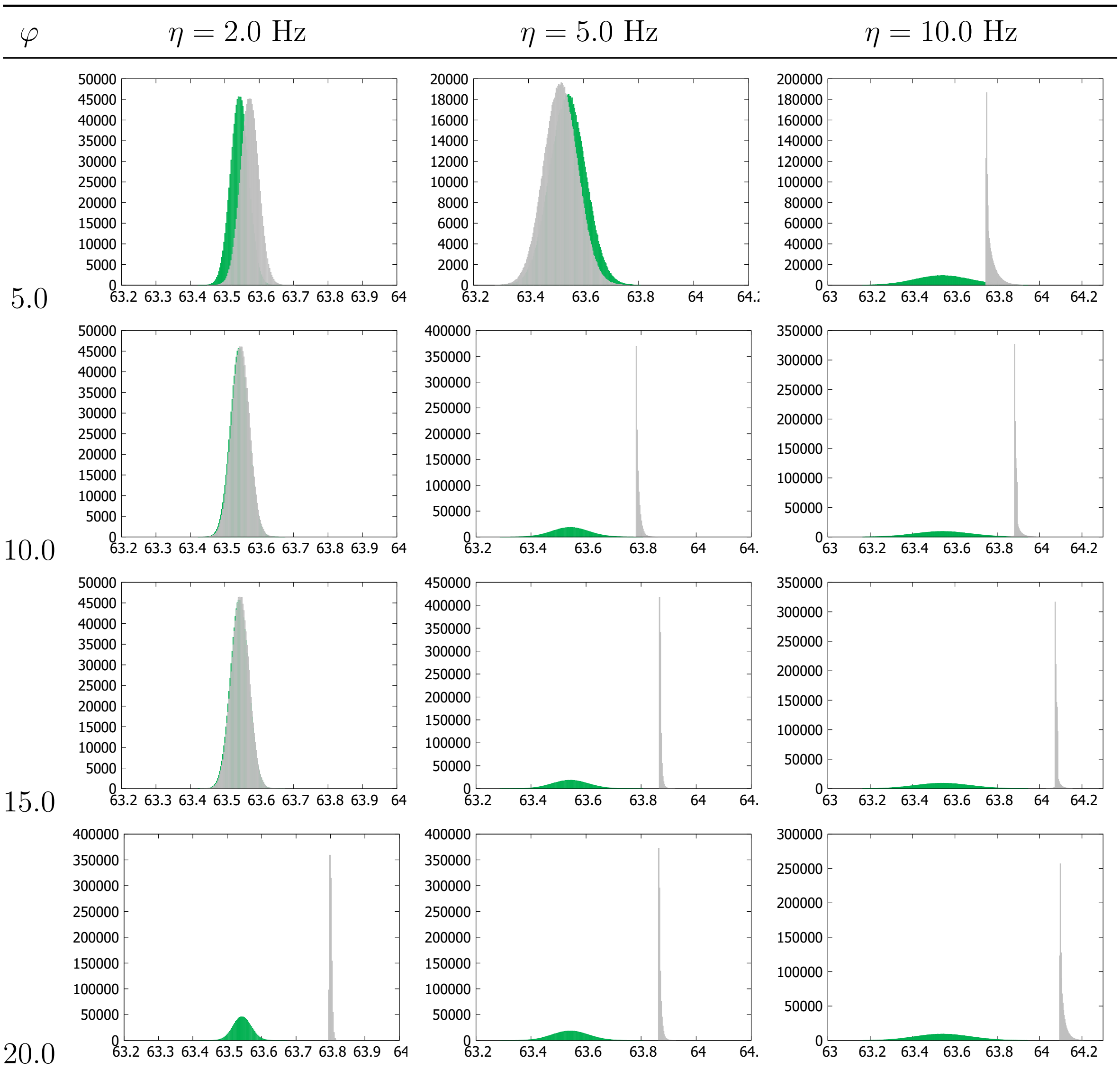

Source: Author production.

Figure 14 – Frequency response for the robust design ($\eta = 10$ Hz and $\varphi = 15.0$) and for the deterministic design (left) and topology with dynamic displacement fields (absolute values) at three different frequencies for the same robust design (right), obtained at 700 Hz.

Frequency Response	Displacement Field

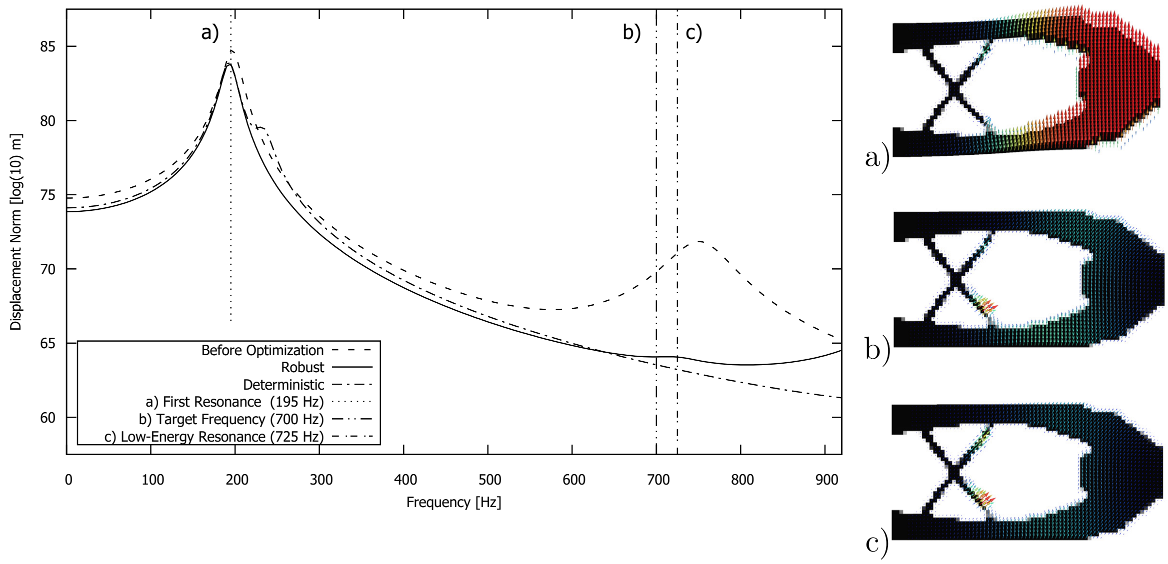

Source: Author production.

design trend can be noticed at combinations of higher values of η and φ. An extremely abrupt change in the structures robustness is also observed at the exact same design points (Fig. 13). This fact confirms the high nonlinearity of the problem with respect to both η and φ. Frequency response of the design obtained with $\varphi = 15.0$ and $\eta = 10.0$ Hz is presented in Fig. 14. It can be seen that a low-energy resonance appears after the target frequency, making the frequency plot of the displacement norm quasi-flat at the region of interest. This is a different mechanism than the one used to increase the robustness at 365 Hz, but also effective in making the dynamic response robust for all samples of the vector with the realizations of $X(\omega)$. The robustness improvement is noticeable when compared to the result obtained with the deterministic approach. Deformed topology and forced displacement fields are also depicted in Fig. 14, where it is observed that the external loads are placed at a "nodal region" of the vibration mode related to that low-energy resonance (Fig. 14, line c), which has great influence on the structure behavior at the excitation frequency (Fig. 14, line b). This "weak" mode, almost orthogonal to the load vector, is not dangerous for amplifying the global vibration and is useful to improve the robustness of the displacement norm around the excitation frequency.

It should be stressed that the damping ratio has a large impact in the shape of all resonances. Thus, different values of ζ can alter the shape of this "weak" mode. Nonetheless, the only matter is to slightly relocate this resonant frequency to cope with this modification.

8.2.1.3 Results at 1135 Hz

Resultant topologies for 1135 Hz are depicted in Fig. 15, where it can be noticed that the results also present mass accumulation close to the loading edge.

Figure 15 – Topologies obtained at 1135 Hz, for different values of η and φ.

φ	$\eta = 2.0$ Hz	$\eta = 5.0$ Hz	$\eta = 10.0$ Hz
5.0			
10.0			
15.0			
20.0			

Source: Author production.

Table 8 – Expected values $E[N_{m\omega dB}]$ at 1135 Hz for different values of η and φ.

φ	$\eta = 2.0$ Hz	$\eta = 5.0$ Hz	$\eta = 10.0$ Hz
0.0	59.4141	59.4142	59.4146
5.0	59.3992	59.3985	59.3877
10.0	59.4031	59.3833	59.7844
15.0	59.3929	59.7755	59.8370
20.0	59.3987	59.7765	59.8449

Source: Author production.

Table 9 – Standard deviations $Std[N_{m\omega dB}]$ at 1135 Hz for different values of η and φ.

φ	$\eta = 2.0$ Hz	$\eta = 5.0$ Hz	$\eta = 10.0$ Hz
0.0	0.0154	0.0384	0.0758
5.0	0.0152	0.0380	0.0737
10.0	0.0153	0.0375	0.0094
15.0	0.0152	0.0036	0.0050
20.0	0.0152	0.0026	0.0038

Source: Author production.

Slight differences can be noticed among the designs obtained with higher values of φ and η. Histograms of the dynamic responses are presented in Fig. 16 and the expected values and standard deviations of each histogram are presented in Tables. 8 and 9.

The cases with higher values of φ and η show an improvement in their robust behavior in comparison to the other evaluated cases, even with the relatively small topology differences observed in Fig. 15. Figure 17 shows the dynamic response for the design obtained with $\eta = 10.0$ Hz and $\varphi = 15.0$.

Again, a low-energy resonance is close to the target frequency, creating a range of frequencies where the displacement norm presents almost no variation. This weakly activated mode is clearly responsible for the improved robustness of the structure. In Fig. 17, the deformed structures and forced displacement fields for three frequencies, including the "weak" neighboring resonance, indicate the referred dynamic behavior, which is also used at 700 Hz.

8.2.1.4 Results at 1440 Hz

Fig. 18 shows the topologies obtained at 1440 Hz for different values of η and φ. The trend of mass accumulation near the loading edge is very clear in the designs and slender beams provide the connection of the mass to the support. Some slight differences are seen in the designs, like the formation of secondary and very slender reinforcements close to the base, connecting the lateral beams to the cross-shape reinforcements.

Histograms of the dynamic responses are shown in Fig. 19. Expected values and standard deviations of the responses of the deterministic ($\varphi = 0.0$) and robust designs are shown in Tables 10 and 11. Also, the same behavior observed at 700 and 1135 Hz is presented in these results. The nonlinearity of the problem with respect to η and φ causes an abrupt transition in the response trend when the setup parameters are large. Fig. 20 shows the frequency response of the design obtained with $\varphi = 15$ and $\eta = 10$ Hz.

Figure 16 – Histograms of $N_{m\omega dB}$ comparing the robust and deterministic designs at 1135 Hz, for different values of φ and η. Histograms in green are relative to deterministic designs and the histograms in grey are relative to robust designs.

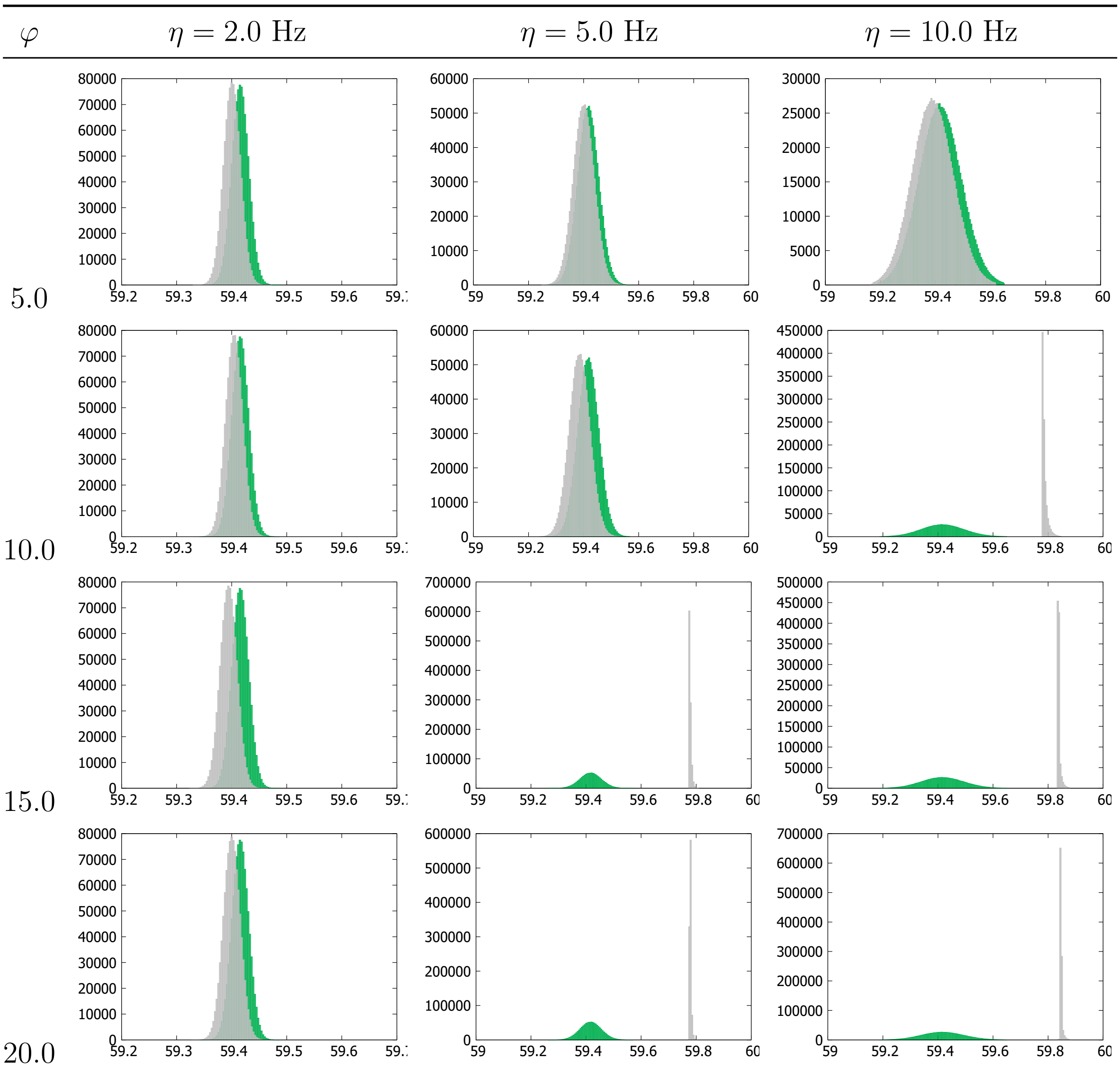

Source: Author production.

Table 10 – Expected values $E[N_{m\omega dB}]$ at 1440 Hz, for different values of φ and η.

φ	$\eta = 2.0$ Hz	$\eta = 5.0$ Hz	$\eta = 10.0$ Hz
0.0	57.4073	57.4073	57.4075
5.0	57.3964	57.3795	57.4057
10.0	57.4025	57.3797	57.8179
15.0	57.3876	57.4867	57.8299
20.0	57.3962	57.8386	57.9132

Source: Author production.

Figure 17 – Frequency response for the robust design ($\eta = 10$ Hz and $\varphi = 15.0$) and for the deterministic design (left) and topology with dynamic displacement fields (absolute values) at three different frequencies for the same robust design (right), obtained at 1135 Hz.

Frequency Response	Displacement Field

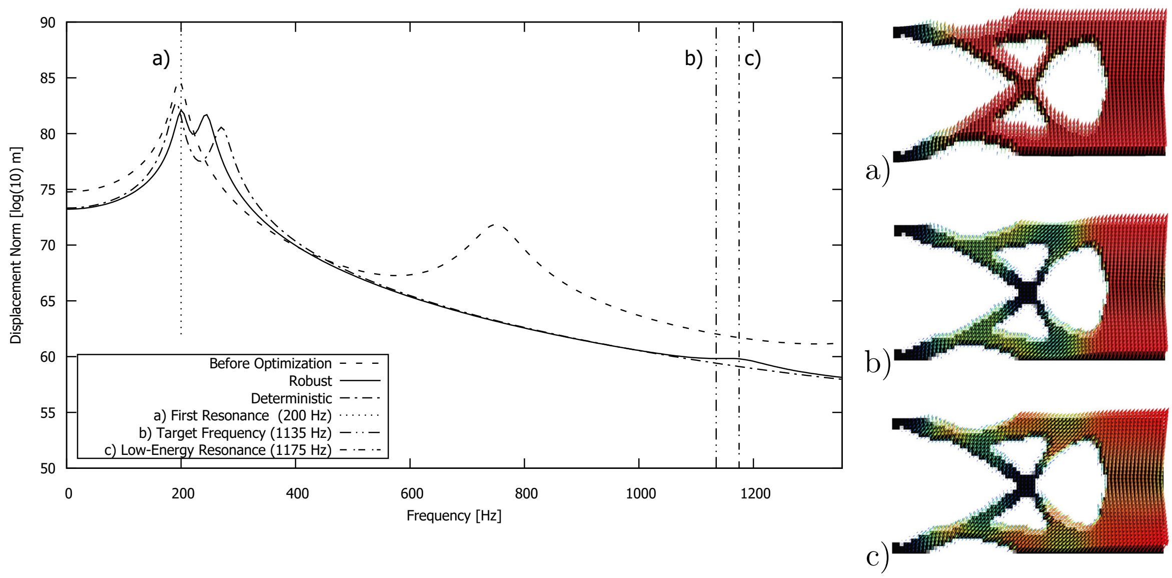

Source: Author production.

Figure 18 – Topologies obtained at 1440 Hz, for different values of φ and η.

φ	$\eta = 2.0$ Hz	$\eta = 5.0$ Hz	$\eta = 10.0$ Hz

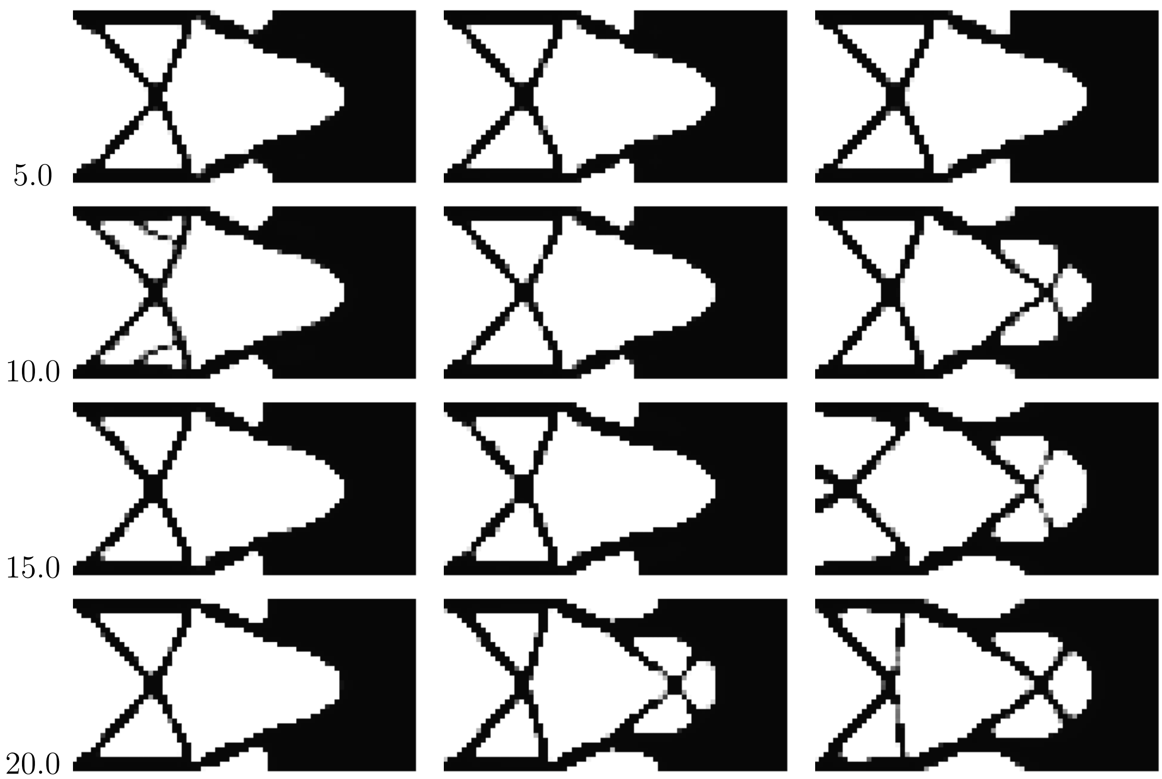

Source: Author production.

Figure 19 – Histograms of $N_{m\omega dB}$, comparing the robust and deterministic designs at 1440 Hz, for different values of φ and η. Histograms in green are relative to deterministic designs and the histograms in grey are relative to robust designs.

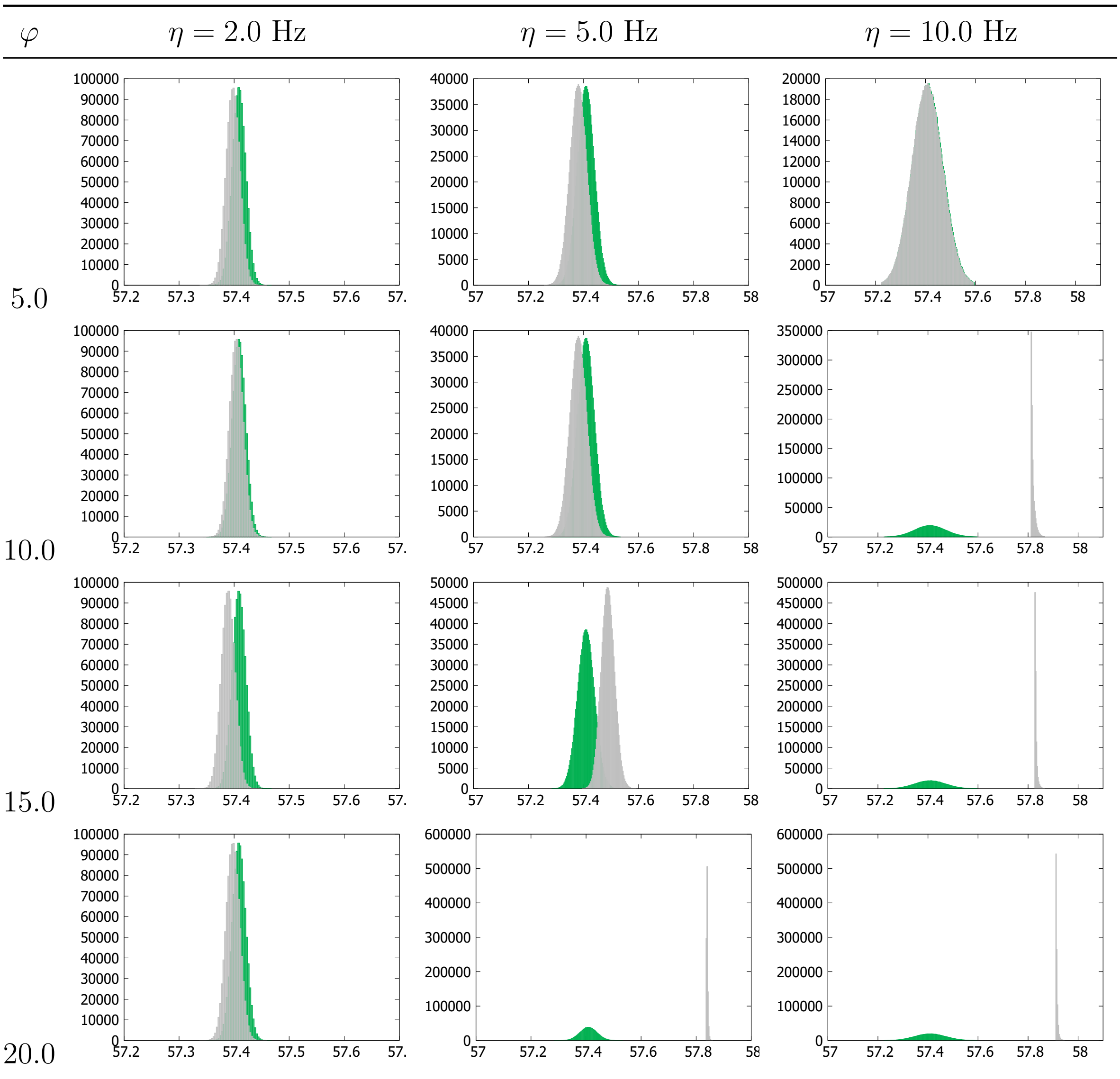

Source: Author production.

Table 11 – Standard deviations $Std[N_{m\omega dB}]$ at 1440 Hz, for different values of φ and η.

φ	$\eta = 2.0$ Hz	$\eta = 5.0$ Hz	$\eta = 10.0$ Hz
0.0	0.0124	0.0310	0.0612
5.0	0.0124	0.0308	0.0611
10.0	0.0124	0.0308	0.0080
15.0	0.0124	0.0245	0.0046
20.0	0.0124	0.0023	0.0038

Source: Author production.

Figure 20 – Frequency response for the robust design ($\eta = 10$ Hz and $\varphi = 15.0$) and for the deterministic design (left) and topology with dynamic displacement fields (absolute values) at three different frequencies for the same robust design (right), obtained at 1440 Hz.

Frequency Response | Displacement Field

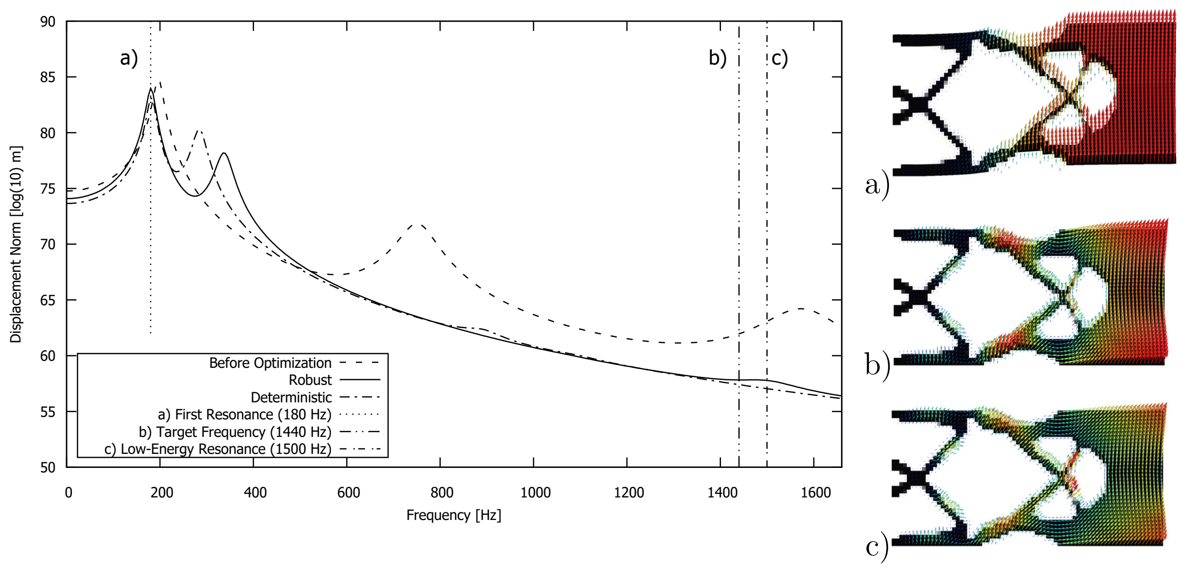

Source: Author production.

Also in this case, a low-energy resonance close to the target frequency ensures the increased robustness of the designs. An interval of frequencies is affected by this new mode and a quasi-flat behavior is noticed at this interval. In Fig. 20, the forced displacement field at frequency "c)", and the deformed topology, demonstrates the "weak" resonance, responsible for the improvement in robustness.

8.2.2 Convergence analysis

Given the highly nonlinear behavior of the objective function and the projection operator, as well as numerical issues associated to resonances, the authors opted to use two continuation strategies. Previous tests performed without the damping continuation, defined in Section 4.3, led to situations where the optimizer cannot relocate the resonances to improve the robustness, as opposed to the results obtained with the continuation procedure for the damping ratio. Additionally, the Heaviside projection continuation, defined in Eqs. (78) and (143), is also recommended since premature large increments on the parameter β_H can lead to drastic modifications in topology, such that it is usually used after the convergence of the original problem.

The convergence of the optimization process for the case with $\bar{\omega} = 1135$ Hz, $\eta = 10$ Hz and $\varphi = 15$ is therefore selected to exemplify the convergence and evolution of the proposed formulation. The result is summarized in Fig. 21, where the solid line shows the normalized value of the Lagrangian Function and the dotted line the volume constraint, for each external iteration. Intermediate topologies and a zoom of the frequency response in the range $[935, 1400]$ Hz are shown for iterations 1, 5, 10, 11 and 13, and the associated values of ζ and β_H are indicated by the tuples (ζ, β_H) over each topology. Iterations 1 to 10 are used to perform the continuation approach for the damping ratio ζ, linearly varying

Figure 21 – Convergence for the Lagrangian Function (solid line), volume constraint (dotted line) and intermediate topologies and frequency responses at some external iterations. Tuples over each topology indicate the pair (ζ, β_H).

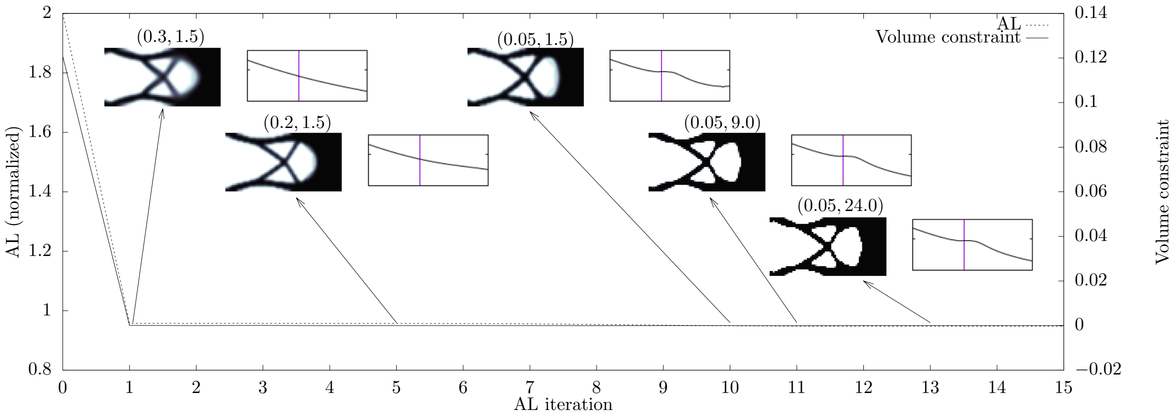

Source: Author production.

from 0.3 to 0.05, but with a fixed β_H equal to 1.5. Iterations 11 to 15 are used to perform the continuation approach of the projection operator, but with a fixed damping ratio $\zeta = 0.05$. From this figure, it is possible to verify that the convergence is very smooth, leading to a feasible solution. Also, it is possible to verify that the continuation for the damping ratio allows for a smooth formation of the "weak" activated modes along the external iterations. Also, it is possible to verify the efficacy of the continuation approach for the projection, as the grey areas are removed along iterations 11 to 15. The final topology and the complete final frequency response for this case are depicted in Fig. 17.

8.2.3 Cantilever beam with bottom loading

Results in the previous sections show that the appearance of weakly activated modes is the basis for increasing robustness at higher frequencies. Therefore, a second test case is used to assess if the proposed formulation can increase robustness with an asymmetric disposition of the loading and boundary conditions, as shown in Fig. 6. A mesh of 72×45 was considered, giving a total of 3420 elements, in combination with the spatial filter radius $R = 0.031$ m.

Based on the results obtained for the symmetric case, only results obtained with $\varphi = 15.0$ and $\eta = 10.0$ Hz are presented. The resulting topologies are shown in Fig. 22.

Design differences between deterministic and robust solutions are noticed for all evaluated cases, specially at lower frequencies, i.e. close to the first resonance frequency of the non-optimized design.

The topology obtained for 420 Hz present the largest difference when comparing the deterministic to the robust formulations. The absence of the dynamic absorber in the robust design is the most notable difference, while a very thin and slender load path connects the loading to the rest of the topology.

At 700 Hz, there is also a relatively large modification, even though the main characteristics of the design presented in the deterministic approach are conserved. One noticeable difference, however, is related to the cross-shaped reinforcement, that appeared in the robust design.

Structural modifications between deterministic and robust designs are less noticeable

Figure 22 – Topologies obtained for the asymmetric loading test case, for different target frequencies and for $\varphi = 15.0$ and $\eta = 10.0$ Hz.

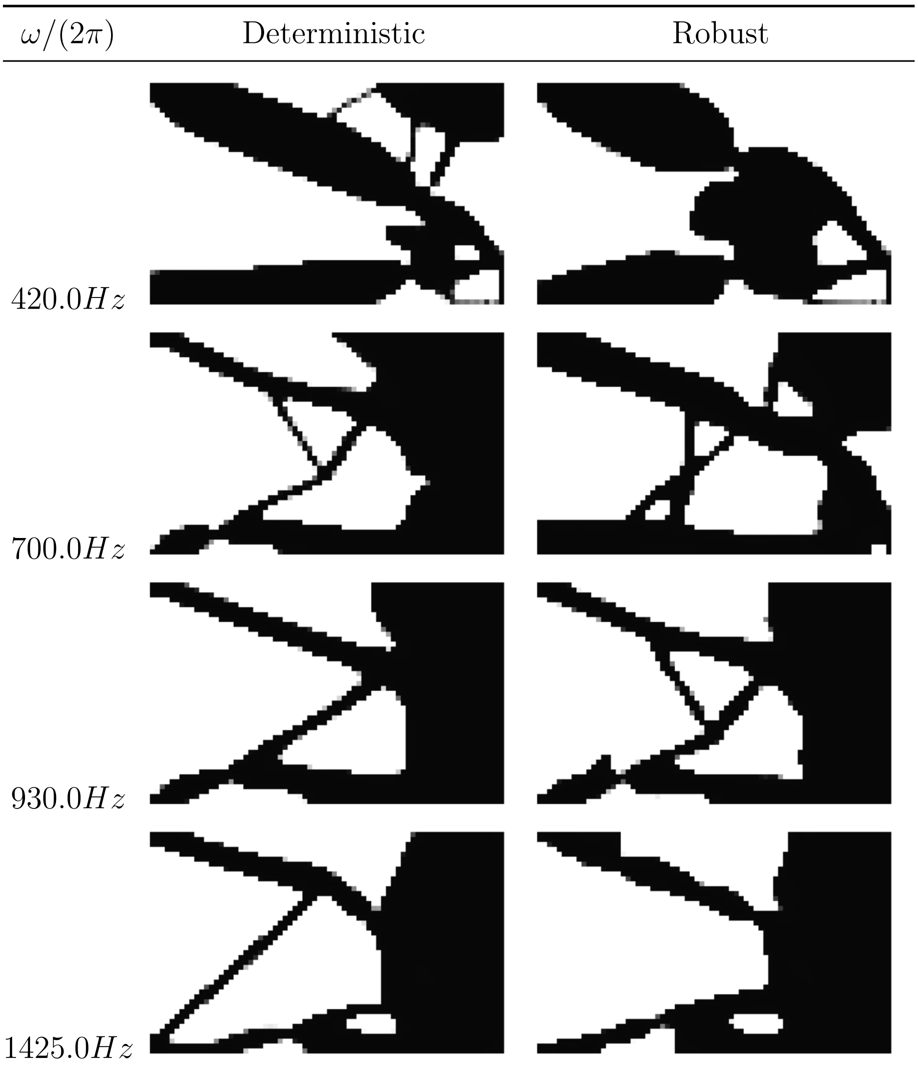

Source: Author production.

Figure 23 – Frequency response for the robust design ($\eta = 10$ Hz and $\varphi = 15.0$) and for the deterministic design (left) and displacement fields (absolute values) at three different frequencies for the same robust design (right), obtained at 420 Hz.

Frequency Response	Displacement Field
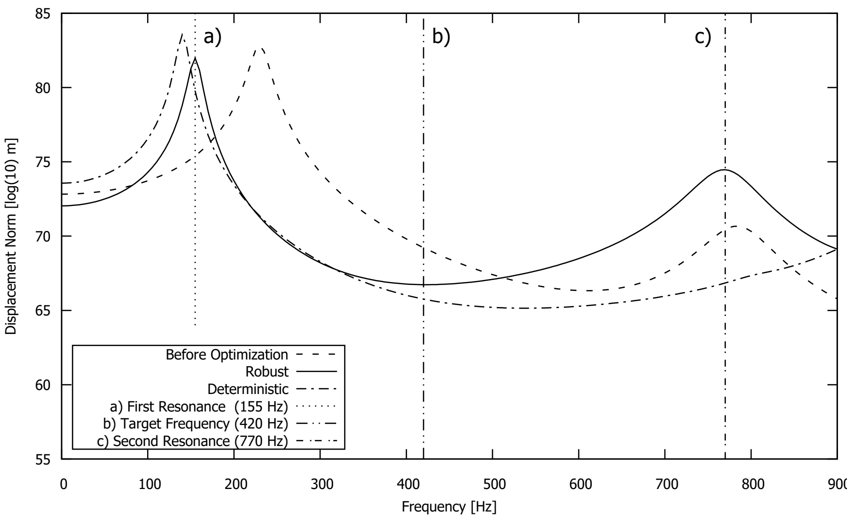	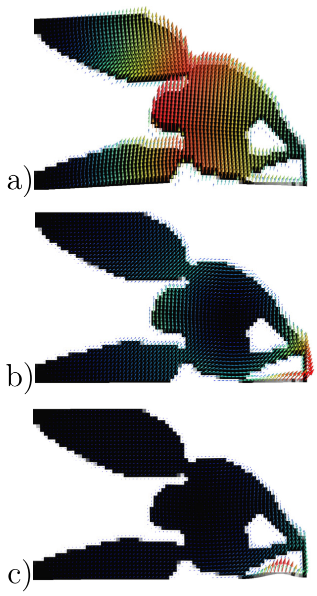

Source: Author production.

at 930 Hz and 1425 Hz, and are basically related to slightly different mass distribution throughout the domain. The common characteristic of mass accumulation at the loaded end is seen in both deterministic and robust designs.

Frequency responses and displacement fields are depicted in Figs. 23, 24, 25 and 26. Additionally, the histograms comparing the robust designs to the deterministic designs outputs are shown in Fig. 27.

The histograms shown in Fig. 27 confirm the efficacy of the proposed formulation for all evaluated cases, since structures designed with the proposed formulation present increased robustness.

Regarding the physical mechanism used for the robustness improvements, by the evaluation of the frequency response charts given in Figs. 23, 24, 25 and 26, it is clear that the trends noticed for the symmetrically loaded cases are also observed herein. For 420 Hz, the mechanism is to relocate the first and second resonances to obtain a quasi-flat dynamic response at the neighborhood of the target frequency. For the other three frequencies, the same mechanism used in the symmetric cases is also observed. Again, a low-energy resonance mode is created close to the target frequency, influencing the surroundings and also making the frequency response quasi-flat in this region. Such strategy is considered very efficient and leads to highly-robust designs with very low design modifications with respect to the deterministic approach.

8.3 DYNAMIC RESPONSE MAXIMIZATION

The problem related to maximization cases is, generally speaking, of higher complexity in comparison to the ones related to minimization since the resultant design will

Figure 24 – Frequency response for the robust design ($\eta = 10$ Hz and $\varphi = 15.0$) and for the deterministic design (left) and displacement fields (absolute values) at three different frequencies for the same robust design (right), obtained at 700 Hz.

Frequency Response	Displacement Field

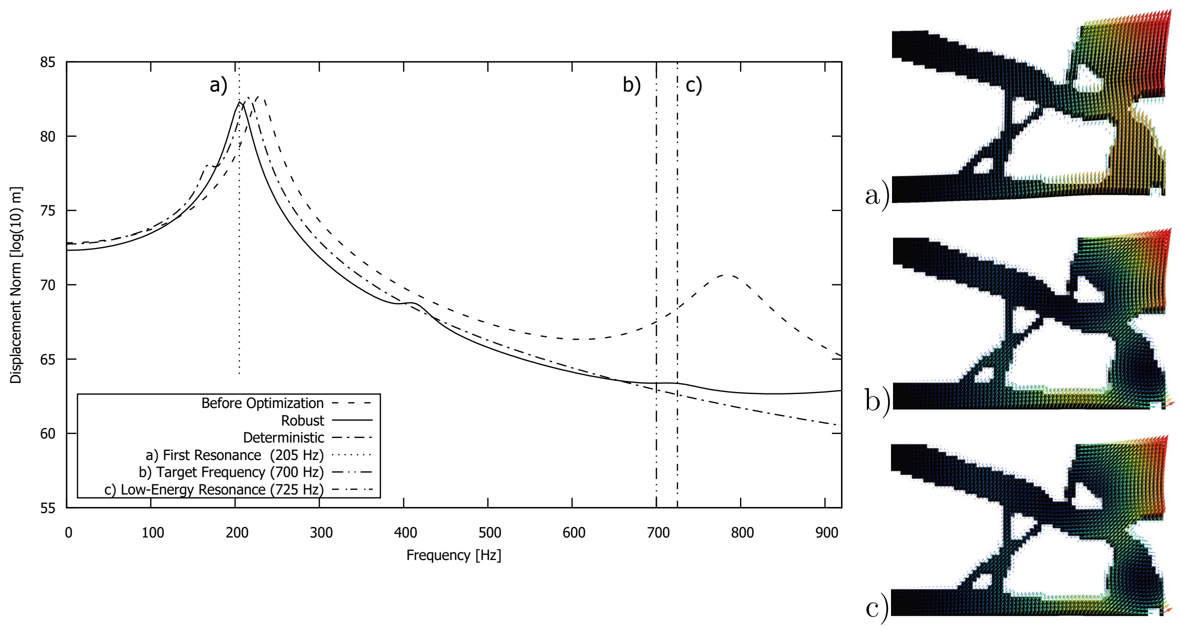

Source: Author production.

Figure 25 – Frequency response for the robust design ($\eta = 10$ Hz and $\varphi = 15.0$) and for the deterministic design (left) and displacement fields (absolute values) at three different frequencies for the same robust design (right), obtained at 930 Hz.

Frequency Response	Displacement Field

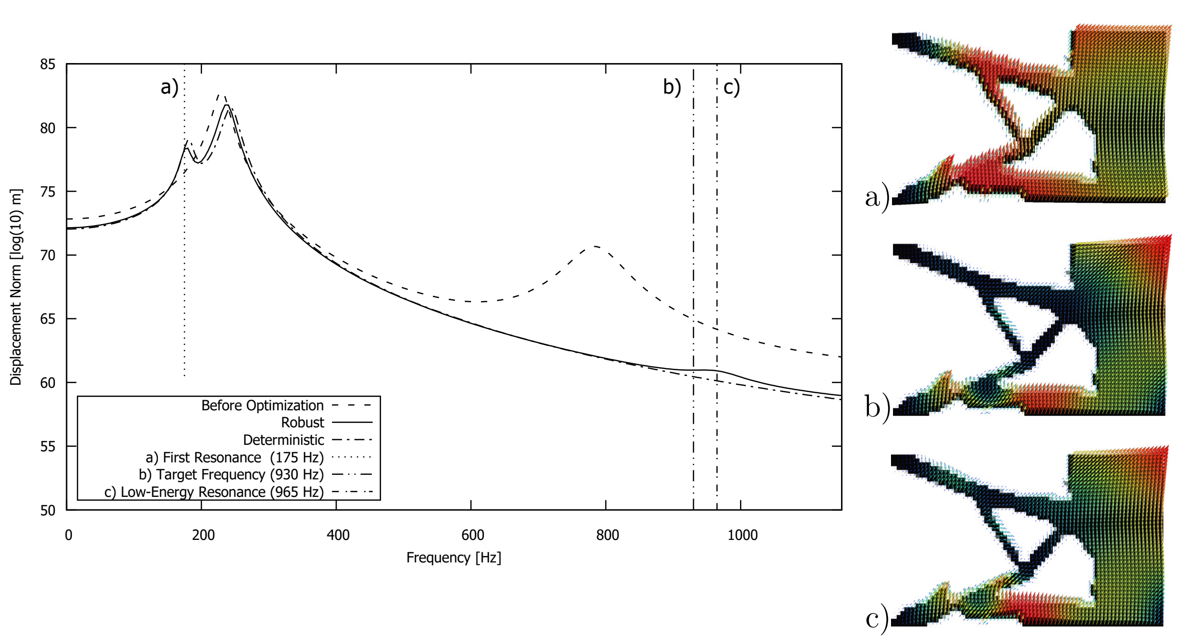

Source: Author production.

Figure 26 – Frequency response for the robust design ($\eta = 10$ Hz and $\varphi = 15.0$) and for the deterministic design (left) and displacement fields at three different frequencies for the same robust design (right), obtained at 1425 Hz.

Frequency Response	Displacement Field
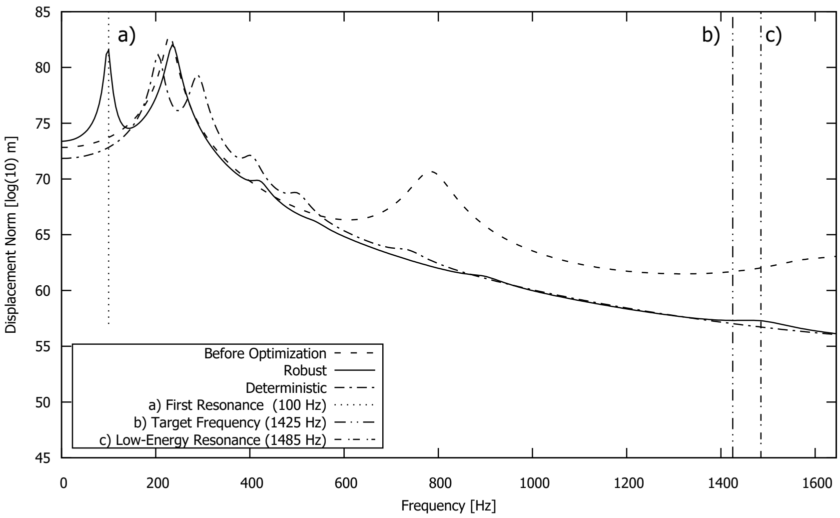	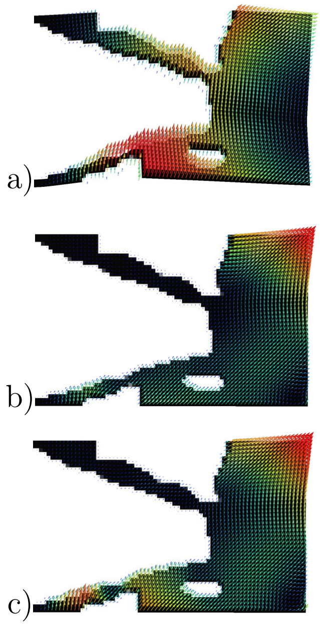

Source: Author production.

Figure 27 – Histograms of $N_{m\omega dB}$ for different frequencies and for $\varphi = 15.0$ and $\eta = 10.0$ Hz. Histograms in green are relative to deterministic designs and histograms in grey are relative to robust designs.

420 Hz	700 Hz	930 Hz	1425 Hz

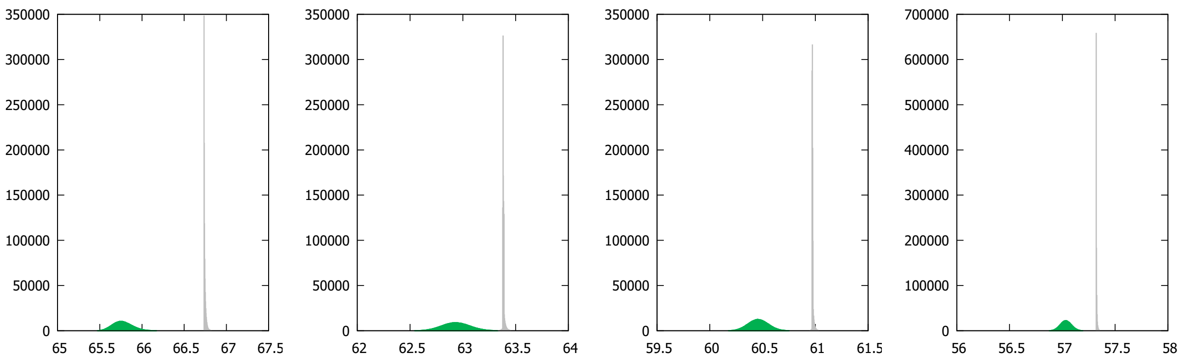

Source: Author production.

likely have a resonance at or close to the target excitation frequency. At this condition, the dynamic stiffness matrix is close to singular and critically ill-conditioned, causing instabilities in the derivatives and consequent difficulties to the optimization process. Moreover, in this work, the design of resonant structures is combined with a probabilistic robust formulation, which presents itself a high nonlinear behavior with respect to the design variables. Therefore, such combination, that targets the design of resonant structures with robust dynamic behavior, increases both the complexity and the nonlinearity of the problem.

The related challenges, however, were addressed after deep investigation of several design cases and fine tuning of the formulation parameters such that, in this Section, the major outcomes are presented and discussed.

The formulation is evaluated by its application on the design of resonant structures at the symmetric case, described in Section 8.1.1, considering for the majority of the cases a mesh of 100×50 elements and spatial filter radius $R = 0.0155$ m. An specific situation at 700 Hz demanded a finer mesh, as described in Section 8.3.2.

Thus, in comparison to minimization results herein presented, all maximization cases demanded a finer mesh and smaller filter radius R since initial formulation testing revealed such necessity for meeting the design goals. As will be seen, the robustness improvements in maximization cases are dependent on slender reinforcements and slight compliant mechanisms, that can only be properly modeled in a well-discretized domain and with an adequate length scale radius R.

For all cases, the parameters γ_1 and $\bar{V}$ from Eq. (137) are defined as 0.75 and $0.5|\Omega|$, respectively. Thus, $\gamma_2 = |\gamma_1| - 1 = 0.25$. The higher value of γ_2 in comparison to the minimization cases increases the importance of the static compliance in the solution, however, the overall picture is still dominated by the dynamic norm, as is desired.

Also, exactly in the same way as done for the minimization cases, the initial design point is selected to violate the volume constraint in 10%, such that the penalty parameter r_p, from Eq. (137), is automatically computed with Eq. 67. Therefore, also in the following cases, results presented as "Before Optimization" are obtained with an homogeneous material distribution given by $\rho_i = 0.5 * 1.1, \forall i$, that is, considering the starting point.

Exponents from the density-weighted norm, presented in Eqs. 86 and 87, are defined as $m = 8.0$ and $w = 2.0$. A higher value of the exponent m helps the dynamic norm to identify the resonances in the structures dynamic responses (MONTERO; SILVA; CARDOSO, 2020).

The problem is solved with $N_{AL} = 15$ external loops where the first $N_\zeta = 10$ iterations are used to effectively solve the problem and to apply the continuation procedure for ζ, Eq. (81). The last 5 AL iterations are used to reduce the occurrence of intermediate relative density values, so that the initial value of the Heaviside projection parameter $\beta_H = 1.5$ is updated along the optimization process as

$$\beta_H^{k+1} = \begin{cases} 1.5, & \text{if } 1 \leq k \leq N_\zeta \\ min\left(\beta_H^k + 10.0, 2.5\beta_H^k\right), & \text{if } N_\zeta < k \leq N_{AL}. \end{cases} \tag{144}$$

The only exception is one single case at 365 Hz, that demanded 10 extra damping continuations, as is discussed and justified in Section 8.3.1. The projection continuation defined for the maximization cases is smoother than the one used in the minimization cases, Eq. 143, due to the higher problem complexity and more sensitive solution stability.

Figure 28 – Topologies obtained with the deterministic approach, Eq. (85), and standard parametrization for the test case depicted in Fig. 5.

365.0 Hz	700.0 Hz	1135.0 Hz	1440.0 Hz

Source: Author production.

Figure 29 – Topologies obtained with the deterministic approach, Eq. (85), and modified parametrization for the test case depicted in Fig. 5.

365.0 Hz, modified	700.0 Hz, modified

Source: Author production.

Again, the parameters φ, $\bar{\omega}$ and η with the associated $\Delta\omega$ are used to study the formulation. Resultant topologies, evaluation of robustness, analysis of the frequency response and an investigation about the mechanisms used by the optimizer to impose the robustness are discussed in all studied examples.

For mean frequencies $\bar{\omega}$ defined in Section 8.1.1, a single deviation of $\eta = 20$ Hz is studied, with corresponding value of $\Delta\omega$ of 60 Hz to account for at least 99.7% of the original frequency (not truncated) content.

As a reference for further comparison with the robust designs to be presented in the next Sections, Figs. 28 and 29 present the deterministic topologies obtained for maximization case with Eq. (85).

Fig. 28 shows the designs computed with the standard parametrization (mesh with 100×50 elements and $N_{AL} = 15$).

As previously mentioned in this Section, it was necessary to use modified parametrization for two specific cases. Thus, Fig. 29 shows the designs obtained with the deterministic approach and modified parametrization, where the case at 365 Hz was calculated with higher number of damping continuations ($N_{\zeta} = 20$ and $N_{AL} = 25$) and the case at 700 Hz was calculated with finer mesh (140×70).

It is important to highlight that the deterministic problem did not demand such modified parameters, but the robust problem did. Therefore, the related advantages will only be noticed in the robust results, as described in Sections 8.3.1 and 8.3.2.

8.3.1 Results at 365 Hz

Fig. 30 depicts the topologies obtained at 365 Hz for different values of φ and with a fixed value of $\eta = 20$ Hz. The case with $\varphi = 50.0$ needed 10 extra AL iterations, such that only for this specific case $N_{\zeta} = 20$ and $N_{AL} = 25$. The reason for the additional

Figure 30 – Topologies obtained for maximization at 365 Hz, for different values of φ and $\eta = 20$ Hz.

$\varphi = 10.0$	$\varphi = 20.0$	$\varphi = 50.0$

Source: Author production.

iterations is related to the topology definition, being the issue solved with a smoother damping continuation.

Deterministic-like topologies were originated by the use of lower values of φ, however, it is clearly seen in the design obtained with $\varphi = 50$ that a different local minima was identified, such that the originated design has a different overall shape, disposition of reinforcements and visible different stiffness in the connection arrangement to the supports.

It is very important to highlight that the design computed with $\varphi = 50$ must be compared with the deterministic case at 365 Hz shown in Fig. 29, while the other two designs must be compared with the topology shown in Fig. 28. Thus, comparisons related to robustness performance are done meeting this premiss.

The first evaluation consists in a frequency response comparison among the deterministic ($N_{AL} = 15$) and the three robust designs, as shown in 31.

Figure 31 – Frequency response of the deterministic design ($N_{AL} = 15$) and robust design cases at 365 Hz, where Robust Design 1, 2 and 3 correspond to $\varphi = 10.0$, 20.0 and 50.0, respectively.

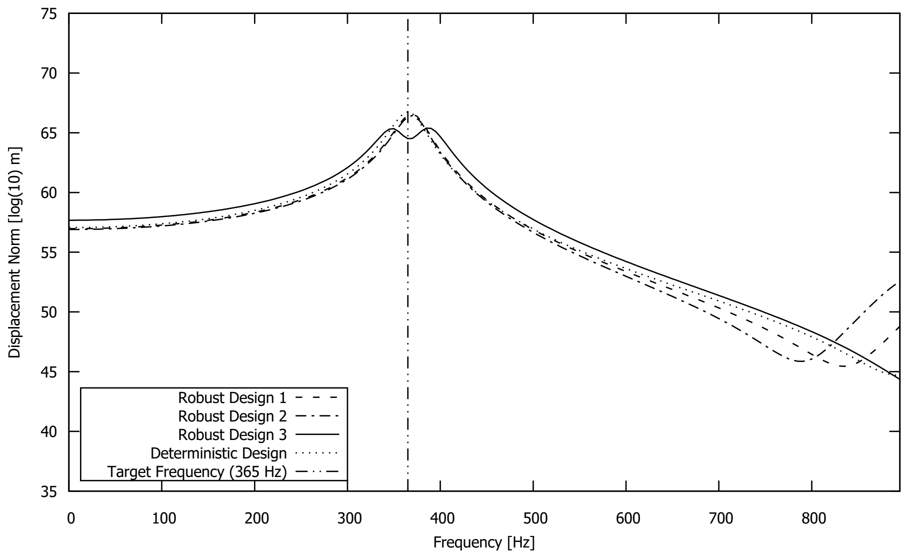

Source: Author production.

The dynamic responses of the designs evaluated with $\varphi = 10.0$ and $\varphi = 20.0$ did not present any important modification with respect to the frequency response of the

Figure 32 – Histograms of $N_{m\omega dB}$, comparing the robust and deterministic designs for maximization at 365 Hz, for different values of φ and $\eta = 20$ Hz. Histograms in green are relative to deterministic designs and the histograms in grey are relative to robust designs.

$\varphi = 10.0$	$\varphi = 20.0$	$\varphi = 50.0$

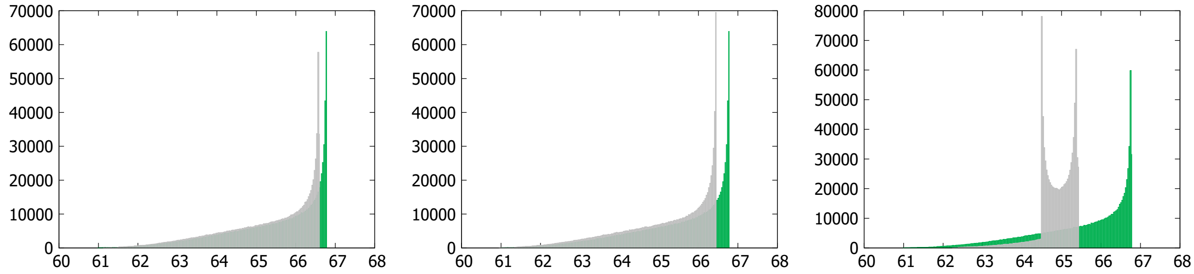

Source: Author production.

Table 12 – Expected values $E[N_{m\omega dB}]$ and standard deviations $Std[N_{m\omega dB}]$ at 365 Hz of the deterministic design ($\varphi = 0.0$) and the robust designs, for different values of φ and $\eta = 20.0$ Hz.

	$\varphi = 0.0$	$\varphi = 10.0$	$\varphi = 20.0$	$\varphi = 50.0$
$E[N_{m\omega dB}]$	65.4653	65.2921	65.1581	64.8539
$Std[N_{m\omega dB}]$	1.2140	1.1888	1.1876	0.4671

Source: Author production.

deterministic design, corroborating with the topology evaluation. However, a relevant difference is noticed in the frequency response of the design computed with $\varphi = 50.0$, where two resonance modes are seen before and after the target frequency.

Such unusual dynamic response seen for the case obtained with $\varphi = 50.0$ explains the difficulties related to its topology definition, since the optimization problem had to deal with two subsequent resonances close to each other together with the typically low dissipation energy existent at lower frequencies (close to the first resonance frequency of the non-optimized design). Since structural damping is considered in this work, the dissipation energy is proportional to the deformation energy. As a consequence, more significant effects appear at higher frequencies, where wave lengths are smaller and, consequently, deformations throughout the structure are higher.

In order to evaluate eventual impacts in the dynamic response robustness related to each frequency response shown in Fig. 31, histograms were calculated according to Section 8 and are depicted in Fig. 32.

Additionally, expected values $E[N_{m\omega dB}]$ and standard deviations $Std[N_{m\omega dB}]$, extracted from the histograms presented in Fig. 32, related to the deterministic design (with $N_{AL} = 25$) and the three robust designs are given in Tab. 12, for further clarity in the results interpretation.

Robustness behaviors of the designs obtained with $\varphi = 10.0$ and $\varphi = 20.0$ had slight improvements in comparison to the deterministic design, as expected after evaluation of the topologies and their frequency responses. Also, slight reduction in $E[N_{m\omega dB}]$ is seen in both cases.

On the other hand, the different local minima obtained with $\varphi = 50.0$ caused an

Figure 33 – Frequency response for the robust design ($\eta = 20$ Hz and $\varphi = 50.0$) and for the deterministic design obtained with $N_{AL} = 25$ (left) and topology with dynamic displacement fields (real values) at three different frequencies for the same robust design (right), obtained for maximization at 365 Hz.

Frequency Response | Displacement Field

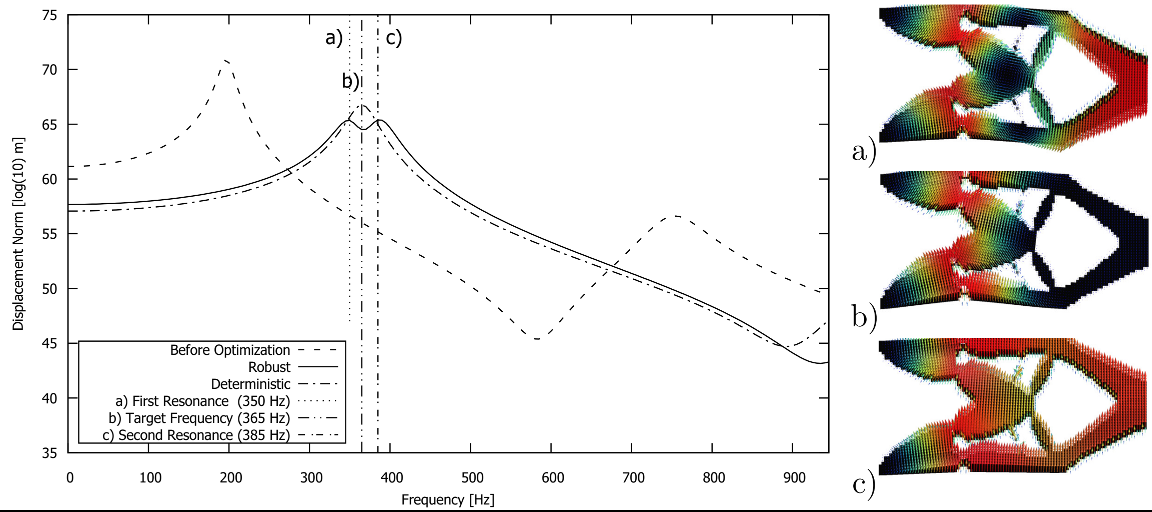

Source: Author production.

abrupt change in the robustness behavior of the dynamic response, leading to a considerably smaller $Std[N_{m\omega dB}]$ with slight reduction in $E[N_{m\omega dB}]$ when compared to the deterministic design. Thus, to further evaluate the physical mechanism that caused such improvement, the frequency response of this design is studied in deeper detail, together with the dynamic displacement fields around the target frequency, as shown in Fig. 33.

Analyzing the frequency response of the robust design, it is possible to notice that the two subsequent high-energy resonances close to the target frequency result in high dynamic displacements within the frequency interval bounded by them. Additionally, a small valley is seen between the referred modes, which is resultant from the characteristic low dissipation energy at lower frequencies, such that a flat region on top of the frequency response could not be created, as will be seen for higher frequencies in the Sections to come.

The dynamic modes seen around the target frequency are global, and rely on the compliant connection originated close to the base, confirming the importance of the drastic change of the design. Additionally, the modes shown in frequencies "a)" and "c)" are asymmetric, meaning that they are different in shape, however, very similar in displacements amplification, which helps to form peaks in the frequency response chart with similar displacement levels.

8.3.2 Results at 700 Hz

The resultant topologies are given in Fig. 34, where the case obtained with $\varphi = 50.0$ demanded a finer mesh discretization. Thus, for this case, the mesh was defined as 140×70, giving a total of 9800 elements. The motivation for the improved mesh is related to the necessity, for this case, of a slender and compliant connection between the loaded edge and the rest of the structure, that needs smaller elements for a proper modeling.

Figure 34 – Topologies obtained for maximization at 700 Hz, for different values of φ and $\eta = 20$ Hz.

$\varphi = 10.0$	$\varphi = 20.0$	$\varphi = 50.0$

Source: Author production.

All three designs presented the basic same overall topology, being the differences related to the stiffness of the reinforcements. It is possible to notice that the design obtained with $\varphi = 50.0$ presents a more compliant connection to the load application point in comparison to the other two designs.

Given the difference in mesh discretization, the design computed with $\varphi = 50$ must be compared with the deterministic case at 700 Hz shown in Fig. 29, and the other two designs shall be compared with the one depicted in Fig. 28. Therefore, subsequent comparisons with respect to robustness performance are done according to this determination.

Frequency responses of the deterministic case shown in Fig. 28 and the three robust designs herein presented are shown in Fig. 35.

Figure 35 – Frequency response of the deterministic design (mesh 100×50 and $N_{AL} = 15$) and robust design cases at 700 Hz, where Robust Design 1, 2 and 3 correspond to $\varphi = 10.0$, 20.0 and 50.0, respectively.

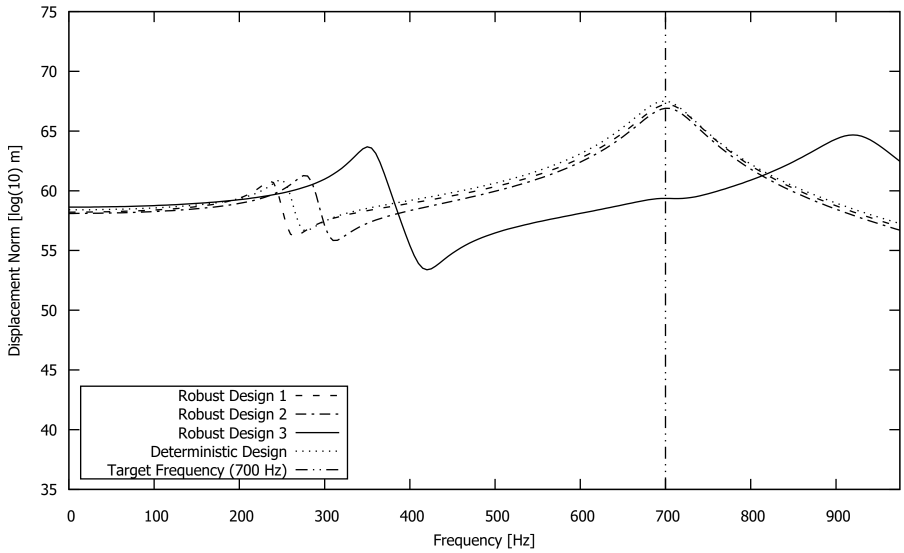

Source: Author production.

The frequency responses of the designs obtained with $\varphi = 10.0$ and $\varphi = 20.0$ presented slightly lower dynamic displacements in comparison to the deterministic design,

Figure 36 – Histograms of $N_{m\omega dB}$, comparing the robust and deterministic designs for maximization at 700 Hz, for different values of φ and $\eta = 20$ Hz. Histograms in green are relative to deterministic designs and the histograms in grey are relative to robust designs.

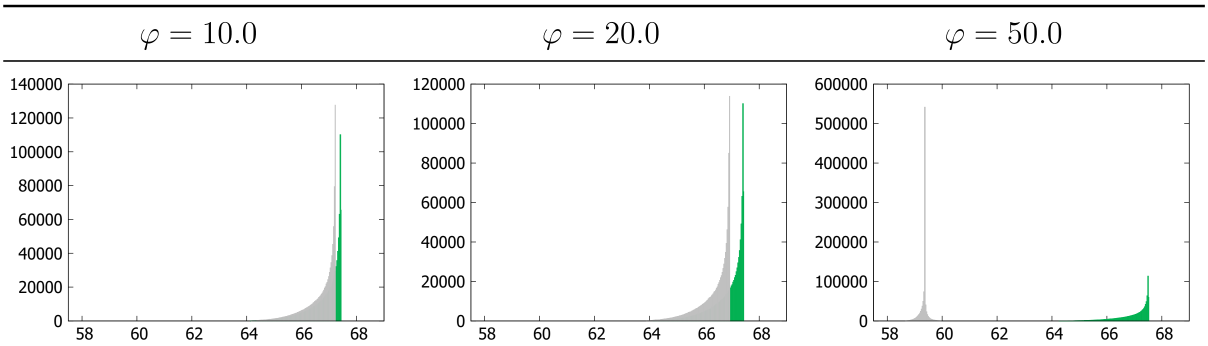

Source: Author production.

Table 13 – Expected values $E[N_{m\omega dB}]$ and standard deviations $Std[N_{m\omega dB}]$ at 700 Hz of the deterministic design ($\varphi = 0.0$) and the robust designs, for different values of φ and $\eta = 20.0$ Hz.

	$\varphi = 0.0$	$\varphi = 10.0$	$\varphi = 20.0$	$\varphi = 50.0$
$E[N_{m\omega dB}]$	66.9829	66.7073	66.4030	59.3238
$Std[N_{m\omega dB}]$	0.5843	0.5689	0.5694	0.1222

Source: Author production.

which is expected since material is being used also in the attempt to improve robustness, and not only in increasing the displacements. A big difference in the dynamic response is clearly identified in the design computed with $\varphi = 50.0$, where a low-energy resonance takes place close to the target excitation frequency and the high-energy mode was relocated at a higher frequency.

In order to understand how each of the dynamic responses translate into behavior robustness, histograms assessment is done for each design, comparing to the equivalent deterministic structure. The histograms are shown in Fig. 36.

Additionally, numeric values of $E[N_{m\omega dB}]$ and $Std[N_{m\omega dB}]$ related to the dynamic responses of the deterministic design, computed with 140×70 elements, and the three robust designs are given in Tab. 13.

As expected, the designs obtained with $\varphi = 10.0$ and $\varphi = 20.0$ demonstrate very small improvements in their dynamic behavior robustness when compared to the deterministic design. However, the design obtained with $\varphi = 50.0$ resulted in an important improvement in the robustness, but with the expense of a reduced level of dynamic displacements in the interval of interest.

Thus, the last case is chosen for a deeper evaluation by the interpretation of the frequency response chart together with the dynamic displacement fields within the domain at certain frequencies of interest, as given in Fig. 37.

Differently from what was identified at 365 Hz, here the mechanism is a low-energy resonance, such as the ones identified in the minimization cases. However, one can clearly see that, when comparing to the dynamic response of the structure prior to the optimization, dynamic displacements have increased considerably and so has the robustness, which

Figure 37 – Frequency response for the robust design ($\eta = 20$ Hz and $\varphi = 50.0$) and for the deterministic design obtained with 140×70 elements (left) and topology with dynamic displacement fields (absolute values) at three different frequencies for the same robust design (right), obtained for maximization at 700 Hz.

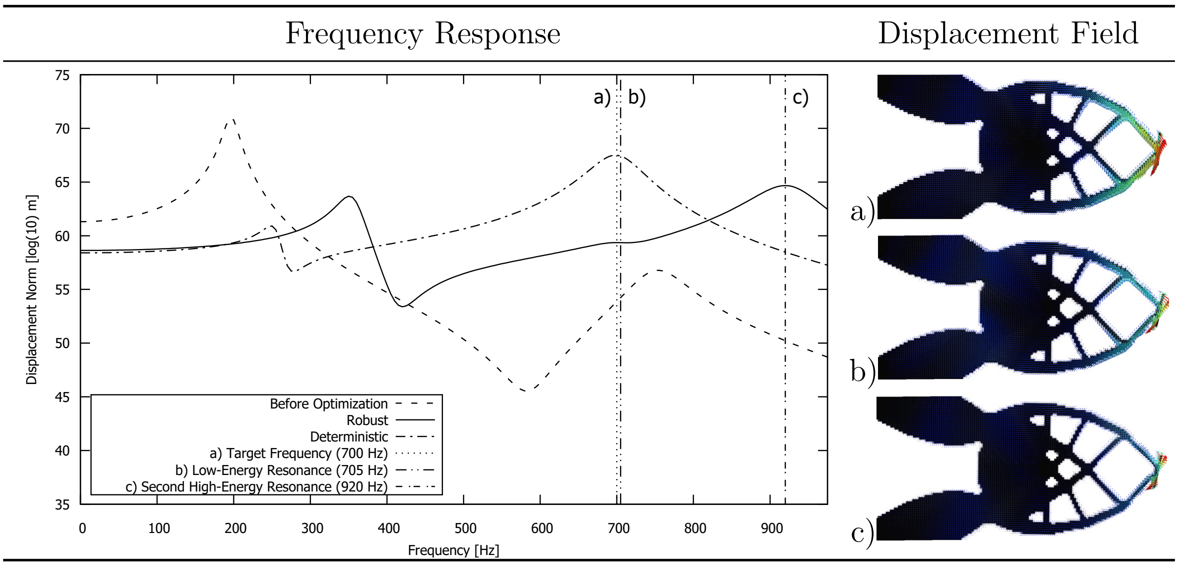

Source: Author production.

classifies the obtained result as valid and successful in meeting the design goals herein proposed. It is important to mention that the higher dissipation energy noticed at this frequency helped in the origination of such quasi-flat pattern in the frequency response.

Thus, the more compliant connection between the structure and the load application edge leads to the low-energy resonance right after the target frequency, creating an almost flat region on the dynamic response chart exactly at 700 Hz, substantially improving the robustness. Analyzing the dynamic displacement fields within the design domain, it is clear that specially the modes seen in frequencies "a)" and "b)" are quite similar and rely on reinforcements at a considerable portion of the right end of the structure, where displacements are seen throughout the domain, but more concentrated at the tip.

The mode seen at frequency "c)", which is a high-energy resonance, is more localized at the right end of the structure and more dependent on the stiffness of the slender beams that connect the loaded edge to the rest of the structure.

8.3.3 Results at 1135 Hz

The results at 1135 Hz reveal topologies very similar to the deterministic design, being the main difference the disposition of reinforcements at the center of the part and also the stiffness of the tip. Figure 38 shows the topologies obtained with different values of φ and a fixed $\eta = 20$ Hz.

Frequency responses of the three robust designs depicted in Fig. 38 are presented together with the response of the deterministic design in Fig. 39.

All frequency responses of robust designs present the same main difference in relation to the response of the deterministic design, which is the presence of a pair of high-energy resonance modes before and after the target frequency. A quasi-flat region is noticed on the frequency response of the three robust cases, with the expense of lower

Figure 38 – Topologies obtained for maximization at 1135 Hz, for different values of φ and $\eta = 20$ Hz.

$\varphi = 10.0$	$\varphi = 20.0$	$\varphi = 50.0$

Source: Author production.

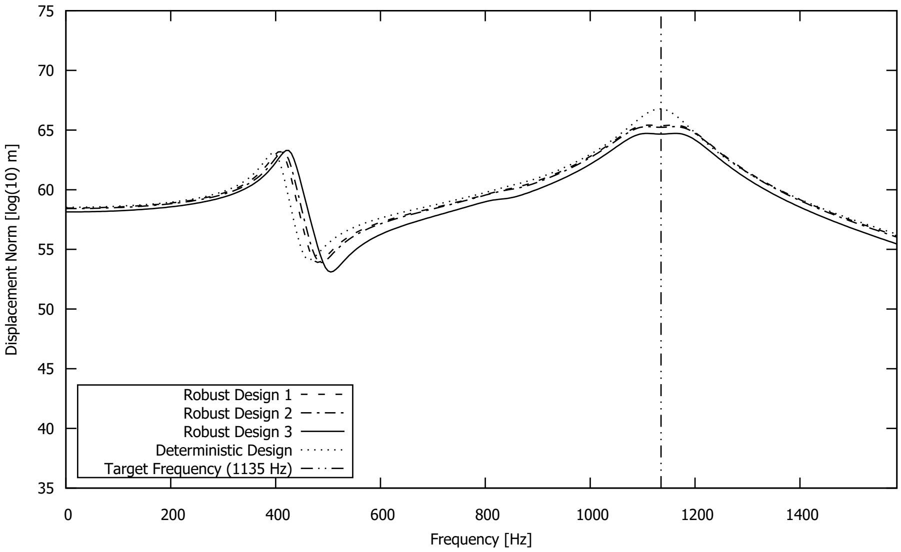

Figure 39 – Frequency response of the deterministic design (mesh 100×50 and $N_{AL} = 15$) and robust design cases at 1135 Hz, where Robust Design 1, 2 and 3 correspond to $\varphi = 10.0$, 20.0 and 50.0, respectively.

dynamic displacements in relation to the deterministic design.

In order to confirm the robustness improvements, histograms with the dynamic responses of each design are presented in Fig. 40. Additionally, the corresponding values of $E[N_{m\omega dB}]$ and $Std[N_{m\omega dB}]$ are presented in Tab. 14.

For all designs, important improvements are observed in their robustness levels when comparing to the deterministic design. Incrementally, the results are more robust as φ increases, however, it is possible to see that a significant drop in $E[N_{m\omega dB}]$ happens when such parameter gains too much importance in the objective function.

Since it represents the most robust result achieved in this case, the design obtained with $\varphi = 50.0$ is chosen for a deeper evaluation so that the physical mechanism can be properly understood. Therefore, the frequency response chart and dynamic displacements fields calculated from the referred design are demonstrated in Fig. 41.

As already mentioned, two high-energy resonances are present in the neighborhood of the target excitation frequency. The first one, defined in the chart as "a)" took place right before 1135 Hz, whereas frequency "c)" appears right after 1135 Hz. Thus, given the high dissipation energy resultant at high frequencies, a quasi-flat region in seen on the

Figure 40 – Histograms of $N_{m\omega dB}$, comparing the robust and deterministic designs for maximization at 1135 Hz, for different values of φ and $\eta = 20$ Hz. Histograms in green are relative to deterministic designs and the histograms in grey are relative to robust designs.

$\varphi = 10.0$	$\varphi = 20.0$	$\varphi = 50.0$

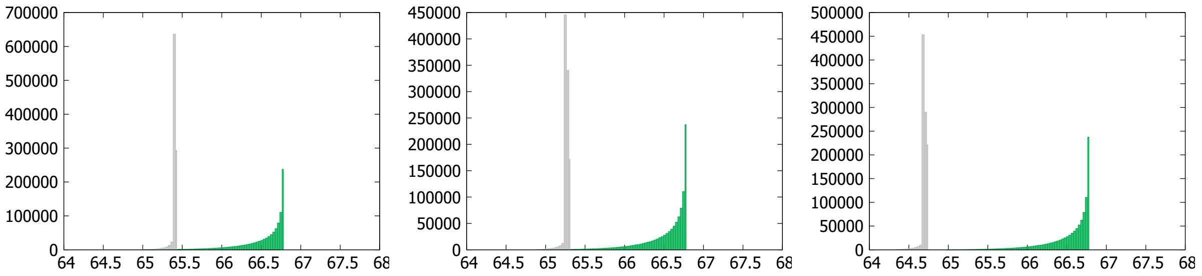

Source: Author production.

Table 14 – Expected values $E[N_{m\omega dB}]$ and standard deviations $Std[N_{m\omega dB}]$ at 1135 Hz of the deterministic design ($\varphi = 0.0$) and the robust designs, for different values of φ and $\eta = 20.0$ Hz.

	$\varphi = 0.0$	$\varphi = 10.0$	$\varphi = 20.0$	$\varphi = 50.0$
$E[N_{m\omega dB}]$	66.5418	65.3816	65.2500	64.6816
$Std[N_{m\omega dB}]$	0.2865	0.0403	0.0368	0.0360

Source: Author production.

Figure 41 – Frequency response for the robust design ($\eta = 20$ Hz and $\varphi = 50.0$) and for the deterministic design (left) and topology with dynamic displacement fields (absolute values) at three different frequencies for the same robust design (right), obtained for maximization at 1135 Hz.

Frequency Response	Displacement Field

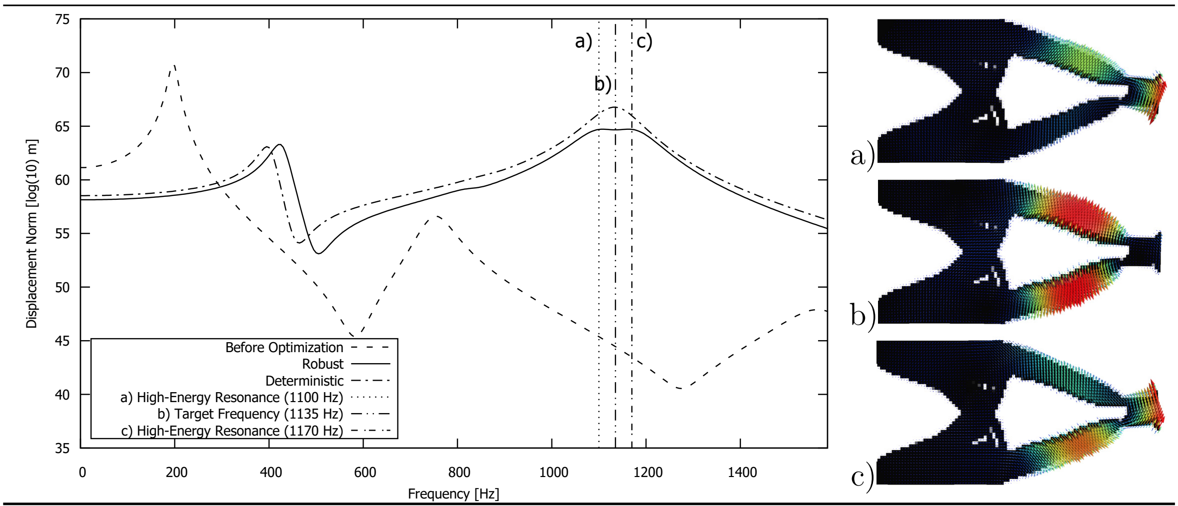

Source: Author production.

Figure 42 – Topologies obtained for maximization at 1440 Hz, for different values of φ and $\eta = 20$ Hz.

$\varphi = 10.0$	$\varphi = 20.0$	$\varphi = 50.0$

Source: Author production.

frequency response chart, connecting the two subsequent modes. Such result is extremely efficient in both improving the robustness and leading to a resonant structure at an interval defined by the mentioned subsequent resonances.

More specifically about the dynamic displacements seen in the two modes, they are symmetric and with approximately the same displacements amplification capacity. Symmetric modes generally appear at the exact same frequency, but can be generated with some offset in case of slight asymmetries in the topology.

The symmetric modes are easily spotted in the dynamic displacement fields shown in Fig. 41. At frequency "a)", it is possible to see that the upper leg is more strongly activated by the mode, and at frequency "c)" the opposite leg is more strongly activated. Therefore, the slight asymmetries existent in the design are actually the artifice that the optimization process used to create the subsequent symmetric modes increasing the dynamic behavior robustness.

8.3.4 Results at 1440 Hz

Figure 42 presents the topologies resultant from the formulation investigation at 1440 Hz, obtained with different values of φ and with a fixed $\eta = 20$ Hz.

Topologies obtained with $\varphi = 10.0$ and $\varphi = 20.0$ are well-defined and are relatively similar to the deterministic design, shown in Fig. 28, being the main difference in the reinforcements arrangement at the center of the part, close to the loaded edge.

Design originated with $\varphi = 50.0$ presented convergence problems, with grey regions in the domain even with the 5 heaviside projection continuations. Thus, for this case in specific, the combination of $\varphi = 50.0$ and $\eta = 20.0$ Hz does not produce satisfactory results. The issue is explained by instabilities in the AL function derivative caused by the high multiplication factor at the parcel related to the $Std[.]$. This result is herein presented as an outcome from the formulation, but cannot be considered a success case.

Frequency responses of the deterministic and the three robust designs are presented in Fig. 43.

All three robust designs present an important difference in the shape of the frequency response close to 1440 Hz, originated by two subsequent high-energy resonance modes, in the same way as in the case at 1135 Hz. It is also easy to see that the higher is the value of φ, the lower are the resonance peaks around the target frequency, since, in theory, more material is being employed in robustness improvements.

Histograms are used to assess the robustness of each design, as shown in Fig. 44,

Figure 43 – Frequency response of the deterministic design (mesh 100×50 and $N_{AL} = 15$) and robust design cases at 1440 Hz, where Robust Design 1, 2 and 3 correspond to $\varphi = 10.0$, 20.0 and 50.0, respectively.

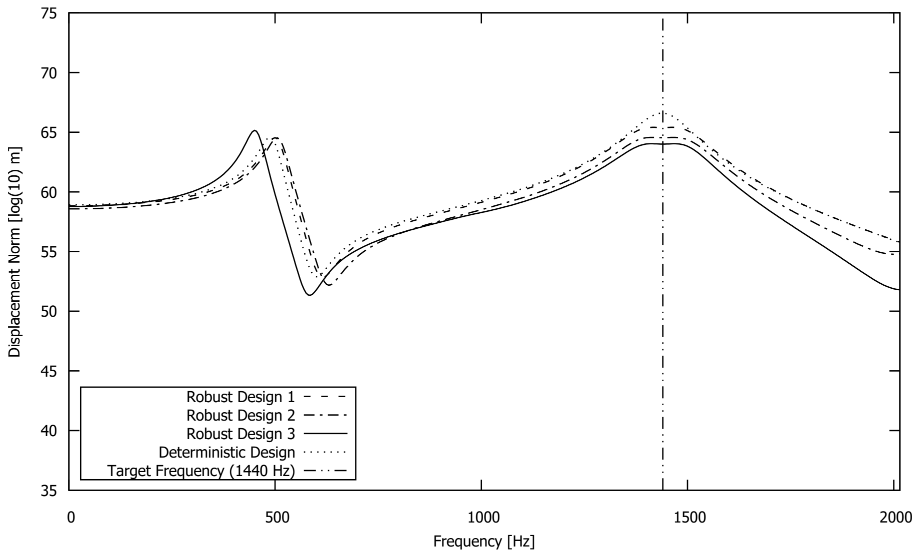

Source: Author production.

Table 15 – Expected values $E[N_{m\omega dB}]$ and standard deviations $Std[N_{m\omega dB}]$ at 1440 Hz of the deterministic design ($\varphi = 0.0$) and the robust designs, for different values of φ and $\eta = 20.0$ Hz.

	$\varphi = 0.0$	$\varphi = 10.0$	$\varphi = 20.0$	$\varphi = 50.0$
$E[N_{m\omega dB}]$	66.4483	65.3945	64.5492	64.0160
$Std[N_{m\omega dB}]$	0.1912	0.0222	0.0160	0.0169

Source: Author production.

and the values of $E[N_{m\omega dB}]$ and $Std[N_{m\omega dB}]$, extracted from the histograms, are presented in Tab. 15.

Noticeable improvements in robustness are seen in all presented designs, while keeping consistently high values of $E[N_{m\omega dB}]$, specially in cases with $\varphi = 10.0$ and $\varphi = 20.0$. For these two cases, incremental reduction in $Std[N_{m\omega dB}]$ is noticed, however, also with incremental reduction in $E[N_{m\omega dB}]$, as an expense. Additionally, slight degradation in robustness is evidenced for the case obtained with $\varphi = 50.0$ together with a more significant drop in $E[N_{m\omega dB}]$, which can be explained by the issues related to the problem convergence.

Thus, for verifying and properly analyzing the reason for the robustness improvements, design obtained with $\varphi = 20.0$ is further investigated, such that its frequency response chart and dynamic displacement fields are given in Fig. 45.

In the same way as seen at 1135 Hz, two subsequent high-energy resonances were created before and after the target excitation frequency. Therefore, also taking advantage of the high dissipation energy present at higher frequencies, an almost flat region is noticed exactly at 1440 Hz, drastically improving the robustness while ensuring high dynamic displacements at the frequency interval bounded by the referred modes.

At higher frequencies, such as 1135 Hz and 1440 Hz, localized modes are more

Figure 44 – Histograms of $N_{m\omega dB}$, comparing the robust and deterministic designs for maximization at 1440 Hz, for different values of φ and $\eta = 20$ Hz. Histograms in green are relative to deterministic designs and the histograms in grey are relative to robust designs.

$\varphi = 10.0$	$\varphi = 20.0$	$\varphi = 50.0$

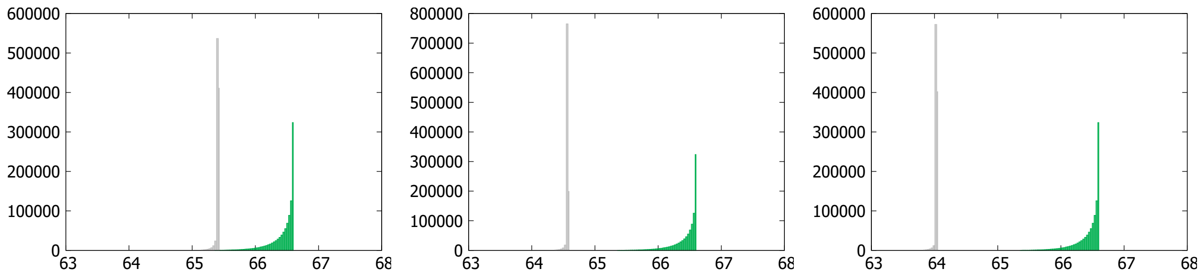

Source: Author production.

Figure 45 – Frequency response for the robust design ($\eta = 20$ Hz and $\varphi = 20.0$) and for the deterministic design (left) and topology with dynamic displacement fields (absolute values) at three different frequencies for the same robust design (right), obtained for maximization at 1440 Hz.

Frequency Response	Displacement Field

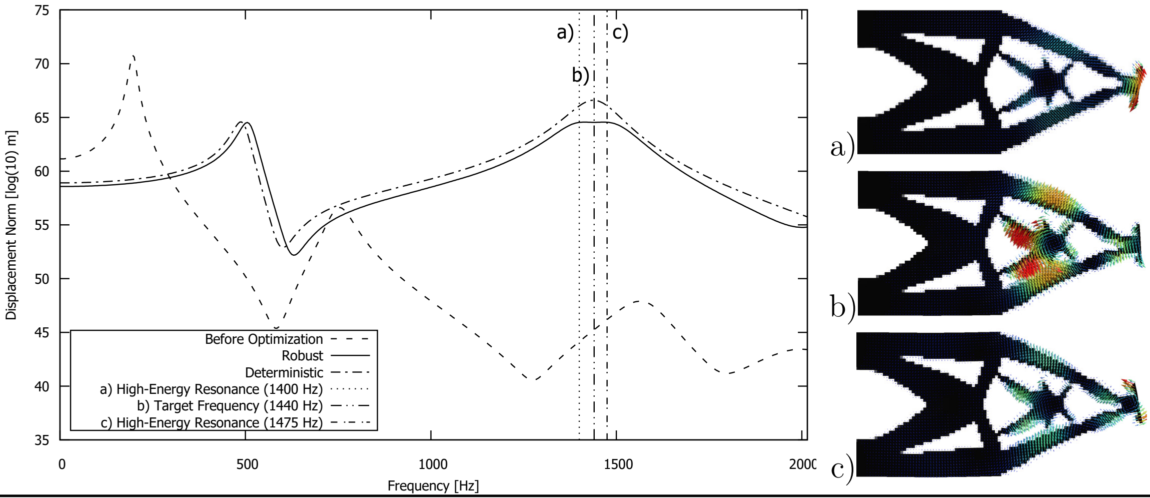

Source: Author production.

easily originated throughout the structures. In this specific case, one can see two different resonance modes, such that at frequency "a)" the mode is described as local bending of the tip and at frequency "c)" the tip is twisting. The dynamic displacements at the target excitation frequency, "b)", are also presented where a local rotation of the center reinforcement is noticed. Thus, the association of these three modes produce the desired effect, significantly increasing the dynamic behavior robustness.

9 CONCLUSIONS

A formulation is proposed for the robust design of structures with optimized dynamic response with respect to uncertainties in the excitation frequency. The objective function is based on the expected value and standard deviation of the density-weighted norm, accompanied by the well-known static compliance to aid in structural connectivity.

The proposed formulation was applied to the design of structures under symmetric and asymmetric loading in relation to the boundary conditions and design domain, considering the variation of the parameters φ and η. Results presented in this work show that the proposed formulation leads to well-defined topologies with robust dynamic behavior.

Results from dynamic displacements minimization show that the physical mechanisms used for the robustness improvements are different and are related to the target frequency. For low frequencies, the mechanism is to relocate the first and second resonances to obtain a quasi-flat dynamic response at the neighborhood of the target frequency. For higher frequencies, a low-energy resonance mode is created close to the target frequency, influencing the surroundings and also making the frequency response quasi-flat in this region. These vibration modes present low contribution to the global response of the structure and are weakly activated in case of eventual asymmetries in the design or due to load vector $\mathbf{F}$ quasi-orthogonal to the displacement vector $\mathbf{U}$. Consequently, low-energy resonances are originated close to the frequency of interest.

For dynamic displacements maximization, the physical artifice employed by the optimization process was also the development of resonances located close to the target frequency, leading to high dynamic displacements together with a robust dynamic behavior. At 365 Hz, the energy dissipation was not high enough for producing a flat region connecting the two subsequent resonant modes. At higher frequencies, such as 1135 and 1440 Hz, the mechanism was essentially the same as the one noticed at 365 Hz, being the main difference the presence of enough energy dissipation in the structure to allow for a quasi-flat region connecting the two high-energy resonances. Particularly at 1135 Hz, symmetric modes were noticed. Results at 700 Hz differ from the others, such that the feasible solution was a low-energy resonance that did improve the behavior robustness and dynamic displacements magnitude, however, not in the same levels compared to the other evaluated frequencies.

Finally, the author highlights that the use of excessively high values for the parameters φ and η may lead to robustness degradation due to the nonlinearity of the problem. Thus, in order to avoid related issues, the definition of the input parameters needs to be done with care and with physical meaning. The convergence issue presented in the maximization of dynamic displacements at 1440 Hz, with $\varphi = 50.0$, is an example of such difficulty.

9.1 FUTURE WORK

The following items were identified as eventual improvement points for future works:

- Further study examples of maximization of dynamic displacements, exploring cases with finer meshes and filter radius, since studied examples show high dependency on such parameters for meeting the design goals;

- Evaluate results with different damping coefficient levels to confirm results feasibility, specially in lower damping scenarios;

- Add local stress constraints to the formulation and reassess all the design cases herein studied;
- Study other methods for computing $E[.]$ and $Std[.]$ with the target of reducing the computational cost, such as the collocation method (LAZAROV, Boyan S; SCHEVENELS; SIGMUND, 2012) or the perturbation method (SILVA; CARDOSO, 2016).

The achievements of the mentioned improvement opportunities would enhance the understanding of the highly nonlinear problem herein solved (deeper evaluation of maximization cases and different damping levels), enhance the formulation capabilities (stress constraints) and improve the solution speed (alternative methods).

REFERENCES

AGARWAL, Harish. **Reliability based design optimization: formulations and methodologies**. [S.l.]: University of Notre Dame, 2004. Cit. on p. 35.

ARMIJO, Larry. Minimization of functions having Lipschitz continuous first partial derivatives. **Pacific Journal of Mathematics**, Mathematical Sciences Publishers, v. 16, n. 1, p. 1–3, Jan. 1966. DOI: 10.2140/pjm.1966.16.1. Available from: <https://doi.org/10.2140/pjm.1966.16.1>. Visited on: 23 July 2019. Cit. on p. 25.

ARORA, Jasbir S. **Optimization of structural and mechanical systems**. [S.l.]: World Scientific, 2007. Cit. on p. 24.

ARORA, Jasbir Singh. **Introduction to optimum design**. 2. ed. San Diego: Elsevier, 2004. p. 728. ISBN 978-0-12-064155-0. DOI: 10.1016/B978-0-12-064155-0.X5000-9. Available from: <https://doi.org/10.1016/B978-0-12-064155-0.X5000-9>. Visited on: 3 June 2019. Cit. on p. 25.

BATHE, Klaus-Jürgen. **Finite element procedures**. 2. ed. Watertown, MA: Prentice Hall, Pearson Education, Inc., 2014. ISBN 978-0-9790049-5-7. Cit. on p. 21.

BAUER, H.; BURCKEL, R.B. **Probability Theory**. [S.l.]: De Gruyter, 2011. (De Gruyter Studies in Mathematics). ISBN 9783110814668. Available from: <https://books.google.com.br/books?id=IxrBdh0ilK8C>. Cit. on pp. 36, 37.

BENDSØE, Martin P; OLHOFF, Niels. A method of design against vibration resonance of beams and shafts. **Optimal Control Applications and Methods**, Wiley Online Library, v. 6, n. 3, p. 191–200, 1985. Cit. on p. 13.

BENDSØE, Martin P; SIGMUND, Ole. Material interpolation schemes in topology optimization. **Archive of applied mechanics**, Springer, v. 69, n. 9-10, p. 635–654, 1999. Cit. on p. 28.

BENDSØE, Martin Philip; KIKUCHI, Noboru. Generating optimal topologies in structural design using a homogenization method. **Computer methods in applied mechanics and engineering**, Elsevier, v. 71, n. 2, p. 197–224, 1988. Cit. on p. 28.

BEZANSON, Jeff et al. Julia: A Fresh Approach to Numerical Computing. **SIAM Review**, v. 59, n. 1, p. 65–98, 2017. DOI: 10.1137/141000671. eprint: https://doi.org/10.1137/141000671. Available from: <https://doi.org/10.1137/141000671>. Cit. on p. 42.

BIRGIN, E.; MARTÍNEZ, J. **Practical Augmented Lagrangian Methods for Constrained Optimization**. Philadelphia, PA: Society for Industrial and Applied Mathematics, 2014. Cit. on p. 26.

CARDOSO, Eduardo Lenz; SILVA, GA da; BECK, André Teófilo. Robust topology optimization of compliant mechanisms with uncertainties in output stiffness. **International Journal for Numerical Methods in Engineering**, Wiley Online Library, v. 119, n. 6, p. 532–547, 2019. Cit. on pp. 15, 16, 40, 41.

CHANDRUPATLA, Tirupathi R et al. **Introduction to finite elements in engineering**. [S.l.]: Prentice Hall Upper Saddle River, NJ, 2002. v. 2. Cit. on p. 21.

CHEN, Shikui; CHEN, Wei; LEE, Sanghoon. Level set based robust shape and topology optimization under random field uncertainties. **Structural and Multidisciplinary Optimization**, Springer, v. 41, n. 4, p. 507–524, 2010. Cit. on p. 15.

DA SILVA, GA; BECK, AT; CARDOSO, EL. Topology optimization of continuum structures with stress constraints and uncertainties in loading. **International Journal for Numerical Methods in Engineering**, Wiley Online Library, v. 113, n. 1, p. 153–178, 2018. Cit. on p. 40.

DENG, Jiadong et al. Topology optimization and fabrication of low frequency vibration energy harvesting microdevices. **Smart Materials and Structures**, v. 24, n. 2, 2015. Cit. on p. 14.

DÍAZ, Alejandro R; KIKUCHI, Noboru. Solutions to shape and topology eigenvalue optimization problems using a homogenization method. **International Journal for Numerical Methods in Engineering**, Wiley Online Library, v. 35, n. 7, p. 1487–1502, 1992. Cit. on p. 14.

DITLEVSEN, Ove; MADSEN, Henrik O. **Structural reliability methods**. [S.l.]: Wiley New York, 1996. v. 178. Cit. on p. 36.

DU, Jianbin; OLHOFF, Niels. Topological design of freely vibrating continuum structures for maximum values of simple and multiple eigenfrequencies and frequency gaps. **Structural and Multidisciplinary Optimization**, Springer Science and Business Media LLC, v. 34, n. 2, p. 91–110, May 2007. DOI: `10.1007/s00158-007-0101-y`. Available from: <`https://doi.org/10.1007/s00158-007-0101-y`>. Visited on: 13 June 2019. Cit. on p. 14.

FOX, RL; KAPOOR, MP. Structural optimization in the dynamics response regime-A computational approach. **AIAA Journal**, v. 8, n. 10, p. 1798–1804, 1970. Cit. on p. 13.

HORA, Stephen C. Aleatory and epistemic uncertainty in probability elicitation with an example from hazardous waste management. **Reliability Engineering & System Safety**, Elsevier, v. 54, n. 2-3, p. 217–223, 1996. Cit. on p. 35.

JENSEN, Jakob S.; PEDERSEN, Niels L. Sensitivity analysis and topology optimization in structural dynamics. **DCAMM Report; Technical University of Denmark**, 2005. Cit. on p. 30.

JOG, Chandrashekhar S. Topology design of structures subjected to periodic loading. **Journal of Sound and Vibration**, Elsevier BV, v. 253, n. 3, p. 687–709, June 2002. DOI: `10.1006/jsvi.2001.4075`. Available from: <`https://doi.org/10.1006/jsvi.2001.4075`>. Visited on: 3 June 2019. Cit. on p. 14.

JUNG, Hyun-Seung; CHO, Seonho. Reliability-based topology optimization of geometrically nonlinear structures with loading and material uncertainties. **Finite elements in analysis and design**, Elsevier, v. 41, n. 3, p. 311–331, 2004. Cit. on p. 15.

KATZGRABER, Helmut G. Introduction to monte carlo methods. **arXiv preprint arXiv:0905.1629**, 2009. Cit. on pp. 35, 40.

KHARMANDA, G; OLHOFF, N. Reliability-based topology optimization as a new strategy to generate different structural topologies. In: 15TH Nordic seminar on computational mechanics. [S.l.: s.n.], 2002. Cit. on p. 15.

KROG, Lars A; OLHOFF, Niels. Optimum topology and reinforcement design of disk and plate structures with multiple stiffness and eigenfrequency objectives. **Computers & Structures**, Elsevier, v. 72, n. 4-5, p. 535–563, 1999. Cit. on p. 14.

LAZAROV, B. S.; SCHEVENELS, M.; SIGMUND, O. Topology optimization with geometric uncertainties by perturbation techniques. **International Journal for Numerical Methods in Engineering**, Wiley, v. 90, n. 11, p. 1321–1336, Apr. 2012. DOI: 10.1002/nme.3361. Available from: <https://doi.org/10.1002/nme.3361>. Cit. on p. 15.

LAZAROV, Boyan S; SCHEVENELS, Mattias; SIGMUND, Ole. Topology optimization considering material and geometric uncertainties using stochastic collocation methods. **Structural and Multidisciplinary optimization**, Springer, v. 46, n. 4, p. 597–612, 2012. Cit. on pp. 15, 41, 85.

LAZAROV, Boyan Stefanov; SCHEVENELS, Mattias; SIGMUND, Ole. Robust design of large-displacement compliant mechanisms. **Mechanical sciences**, Copernicus GmbH, v. 2, n. 2, p. 175–182, 2011. Cit. on p. 15.

LOPEZ, RH; BECK, AT. **Optimization of Structures and Components**. [S.l.]: Springer, New York, 2013. Cit. on p. 35.

MA, Z-D; KIKUCHI, Noboru; HAGIWARA, I. Structural topology and shape optimization for a frequency response problem. **Computational mechanics**, Springer, v. 13, n. 3, p. 157–174, 1993. Cit. on p. 14.

MACKAY, David JC. Introduction to monte carlo methods. In: LEARNING in graphical models. [S.l.]: Springer, 1998. p. 175–204. Cit. on p. 40.

MAUTE, Kurt; FRANGOPOL, Dan M. Reliability-based design of MEMS mechanisms by topology optimization. **Computers & Structures**, Elsevier, v. 81, n. 8-11, p. 813–824, 2003. Cit. on p. 15.

MIN, S et al. Optimal topology design of structures under dynamic loads. **Structural optimization**, Springer, v. 17, n. 2-3, p. 208–218, 1999. Cit. on p. 14.

MONTERO, Diego Schmitt; SILVA, Olavo M.; CARDOSO, Eduardo Lenz. Topology optimization for harmonic vibration problems using a density-weighted norm objective function. **Structural and Multidisciplinary Optimization**, Aug. 2020. ISSN 1615-1488. DOI: 10.1007/s00158-020-02695-0. Available from: <https://doi.org/10.1007/s00158-020-02695-0>. Cit. on pp. 15, 30–32, 45, 48, 50, 70.

NIU, Bin et al. On objective functions of minimizing the vibration response of continuum structures subjected to external harmonic excitation. **Structural and Multidisciplinary Optimization**, Springer, v. 57, n. 6, p. 2291–2307, 2018. Cit. on p. 14.

OLHOFF, N.; DU, J. On topological design optimization of structures against vibration and noise emission. **In: Computational aspects of structural acoustics and vibration (Eds. G. Sandberg and R. Ohayon)**, Springer-Viena, p. 217–276, 2009. DOI: 10.1007/978-3-211-89651{_}5. Cit. on p. 51.

OLHOFF, Niels; DU, Jianbin. On topological design optimization of structures against vibration and noise emission. In: COMPUTATIONAL Aspects of Structural Acoustics and Vibration. [S.l.]: Springer, 2008. p. 217–276. Cit. on pp. 14, 28.

PEDERSEN, Niels Leergaard. Maximization of eigenvalues using topology optimization. **Structural and Multidisciplinary Optimization**, Springer Science and Business Media LLC, v. 20, n. 1, p. 2–11, Aug. 2000. DOI: 10.1007/s001580050130. Available from: <2019-12-05>. Cit. on pp. 14, 28, 29.

PIAN, Theodore HH; WU, Chang-Chun. **Hybrid and incompatible finite element methods**. [S.l.]: Chapman and Hall/CRC, 2005. Cit. on p. 47.

SHAKER, Mohammad Hossein; HÜLLERMEIER, Eyke. Aleatoric and Epistemic Uncertainty with Random Forests. In: BERTHOLD, Michael R.; FEELDERS, Ad; KREMPL, Georg (Eds.). **Advances in Intelligent Data Analysis XVIII**. Cham: Springer International Publishing, 2020. p. 444–456. ISBN 978-3-030-44584-3. Cit. on p. 35.

SHIELDS, Michael D. et al. Refined Stratified Sampling for efficient Monte Carlo based uncertainty quantification. **Reliability Engineering and System Safety**, v. 142, p. 310–325, 2015. ISSN 0951-8320. DOI: https://doi.org/10.1016/j.ress.2015.05.023. Available from: <http://www.sciencedirect.com/science/article/pii/S0951832015001726>. Cit. on p. 41.

SIGMUND, Ole. Morphology-based black and white filters for topology optimization. **Structural and Multidisciplinary Optimization**, Springer Science and Business Media LLC, v. 33, n. 4, p. 401–424, Apr. 2007. ISSN 1615-1488. DOI: 10.1007/s00158-006-0087-x. Available from: <https://doi.org/10.1007/s00158-006-0087-x>. Visited on: 17 Dec. 2019. Cit. on pp. 29, 47.

SILVA, GA da; CARDOSO, EL. Topology optimization of continuum structures subjected to uncertainties in material properties. **International Journal for Numerical Methods in Engineering**, Wiley Online Library, v. 106, n. 3, p. 192–212, 2016. Cit. on pp. 35, 40, 85.

SILVA, Olavo M; NEVES, Miguel M. A strategy based on the strain-to-kinetic energy ratio to ensure stability and convergence in topology optimization of globally resonating one-material structures. **International Journal for Numerical Methods in Engineering**, Wiley Online Library, v. 121, n. 16, p. 3636–3659, 2020. Cit. on p. 15.

SILVA, Olavo M. **Otimização Topológica em Problemas de Vibrações Harmônicas Utilizando Potência de Entrada**. 2017. Doctorate Thesis – Universidade Federal de Santau Catarina. Cit. on p. 14.

SILVA, Olavo M.; NEVES, Miguel M.; LENZI, Arcanjo. A critical analysis of using the dynamic compliance as objective function in topology optimization of one-material structures considering steady-state forced vibration problems. **Journal of Sound and Vibration**, Elsevier BV, v. 444, p. 1–20, Mar. 2019. DOI: `10.1016/j.jsv.2018.12.030`. Available from: <`https://doi.org/10.1016/j.jsv.2018.12.030`>. Visited on: 12 June 2019. Cit. on pp. 14, 31.

SILVA, Olavo M.; NEVES, Miguel M.; LENZI, Arcanjo. On the use of active and reactive input power in topology optimization of one-material structures considering steady-state forced vibration problems. **Journal of Sound and Vibration**, v. 464, p. 114989, 2020. ISSN 0022-460X. DOI: `https://doi.org/10.1016/j.jsv.2019.114989`. Available from: <`http://www.sciencedirect.com/science/article/pii/S0022460X19305516`>. Cit. on pp. 14, 30.

STOCKL, G. Topology optimization of trusses under stochastic uncertainty. **ZEITSCHRIFT FUR ANGEWANDTE MATHEMATIK UND MECHANIK**, v. 81, s697–698, 2001. Cit. on p. 15.

SUDRET, B. Uncertainty propagation and sensitivity analysis in mechanical models. **Contributions to structural reliability and stochastic spectral methods. HDR Qualification Thesis, University Blaise Pascal Clermont**, v. 2, p. 69, 2007. Cit. on p. 35.

SUDRET, Bruno; DER KIUREGHIAN, Armen. **Stochastic finite element methods and reliability: a state-of-the-art report**. [S.l.]: Department of Civil and Environmental Engineering, University of California . . ., 2000. Cit. on p. 35.

SVANBERG, Krister. The method of moving asymptotes—a new method for structural optimization. **International journal for numerical methods in engineering**, Wiley Online Library, v. 24, n. 2, p. 359–373, 1987. Cit. on p. 44.

TCHERNIAK, D. Topology optimization of resonating actuators. **Proceedings of the 12th Nordic**, 1999. Cit. on p. 14.

TCHERNIAK, Dmitri. Topology optimization of resonating structures using SIMP method. **International Journal for Numerical Methods in Engineering**, John Wiley & Sons, v. 54, n. 11, p. 1605–1622, 2002. DOI: `10.1002/nme.484`. Available from: <`https://doi.org/10.1002/nme.484`>. Visited on: 10 June 2019. Cit. on pp. 14, 28.

TORTORELLI, Daniel A.; MICHARELIS, P. Design sensitivity analysis: overview and review. **Inverse problems in engineering**, v. 1, p. 71–105, 1994. Cit. on p. 30.

VALENTINI, Fernando; CARDOSO, Eduardo Lenz; SILVA, Olavo M. Robust topology optimization for harmonic displacement minimization of structures subjected to uncertainty in the excitation frequency. **Computer Methods in Applied Mechanics and Engineering**, 2021. DOI: `https://doi.org/10.1016/j.cma.2021.113767`. Cit. on p. 16.

VANMARCKE, Erik. **Random fields: analysis and synthesis**. [S.l.]: World scientific, 2010. Cit. on p. 35.

WANG, Fengwen; LAZAROV, Boyan Stefanov; SIGMUND, Ole. On projection methods, convergence and robust formulations in topology optimization. **Structural and Multidisciplinary Optimization**, v. 43, n. 6, p. 767–784, June 2011. ISSN 1615-1488. DOI: `10.1007/s00158-010-0602-y`. Available from: <https://doi.org/10.1007/s00158-010-0602-y>. Cit. on pp. 29, 47.

WU, Jinglai et al. Robust topology optimization for structures under interval uncertainty. **Advances in Engineering Software**, Elsevier, v. 99, p. 36–48, 2016. Cit. on p. 15.

ZHANG, Xiaopeng; KANG, Zhan; ZHANG, Wenbo. Robust topology optimization for dynamic compliance minimization under uncertain harmonic excitations with inhomogeneous eigenvalue analysis. **Structural and Multidisciplinary Optimization**, Springer, v. 54, n. 6, p. 1469–1484, 2016. Cit. on pp. 15, 41.